Università degli Studi di Roma Tor Vergata

MACROAREA DI SCIENZE MATEMATICHE, FISICHE E NATURALI
Corso di Laurea Magistrale in Fisica

Tesi di Laurea Magistrale

Neutron imaging for the catalysed hydrogen conversion and storage in metal organic frameworks

Relatori:
Dott. Giovanni Romanelli
Prof. Roberto Senesi

Candidata:
Margherita Simoni
0303242

Anno Accademico 2021–2022

Contents

Introduction

Nowadays, the magnitude of the global energy demand poses several challenges. While climate change is dictating the need for a more clean and renewable energy, the living standards are improving, and the population is expected to grow by two billions in the next two decades, further increasing the energy consumption. Currently, fossil fuels still satisfy about 80% of our energy requirements, but according to the International Energy Agency (IEA), the rate of investments in clean energy has risen up to 12% since 2020. Investing in renewable energy technologies is not only crucial to reach a more sustainable economy, but is also important for relieving pressure on consumers and gaining independence from other countries. According to IEA, in 2021, the European Union was the second clean-energy main investor, after China [1]. A central role in the energy revolution is played by molecular hydrogen (H_2). This molecule is an abundant energy carrier, in fact it has the highest energy per unit of mass of any fuel. It can be used to generate electricity or heat, but also for transportation and utilities applications, as well as commercial use. One of the main challenges we face today is to find high density storage options that are also cheap and safe. Currently, we are storing hydrogen in large volume tanks, at low temperatures (liquid form) or high pressure (gaseous form). But these methods are not particularly indicated for applications in the field of transportation. It is of primary interest to find more efficient ways to store molecular hydrogen: while near-term solutions focus on the advancement of high pressure storage technologies, a possible long term solution is to exploit the physical adsorption of molecular hydrogen in porous materials, such as Metal Organic Frameworks (MOFs). Research in the field of porous materials employed as hydrogen storage solutions is still in its early stages: studies describing the interaction between hydrogen and MOFs are still ongoing and aim to determine the most ideal characteristics and synthesis methods. When modeling the behaviour of molecular hydrogen, it is crucial to take into account that this molecule occurs in two isomeric forms, depending on whether the spins of the two hydrogen atoms

are parallel or antiparallel. These two modifications, that have very different physical properties, undergo a conversion from the ortho-states to para-states at low temperature.

In this thesis I report neutron imaging and neutron transmission measurements on molecular hydrogen adsorbed by a MOF known as HKUST-1. The purpose of this work is to model the ortho-para conversion of adsorbed hydrogen, which we expect to be catalyzed by the adsorbant. Moreover I aim to establish if the bond between the H_2 and the adsorption sites of the MOF hinders the rotation of the hydrogen molecule.

The first chapter of this work presents an introduction on the main properties of molecular hydrogen and most common storage techniques, with a particular focus on metal organic frameworks. Moreover the behaviour of adsorbed hydrogen molecules is described, focusing on the ortho-para conversion, as well as a theoretical model used to describe the hindered rotational states of adsorbed H_2. This model Hamiltonian was introduced by Silvera in 1976 [2]. In this work I implemented the eigenvalues equation using Wolfram Mathematics, in order to reproduce the same results. Eigenvalues of the hindered rotor were then used to construct the ortho- and para- partition functions of the system, which I compared to the free hydrogen partition functions.

In the second chapter I outline the main properties of neutron imaging and neutron transmission techniques, underlining the advantages of using neutrons as probes to investigate matter. Here are also described the two instruments employed in the experimental part of this work, which are located at the ISIS neutron and muon source (UK).

The third chapter focuses on the theoretical description of the neutron scattering cross section. An introduction to neutron differential scattering cross section is provided, before focusing of the specific case of diatomic molecules.

The experimental part of this work is reported in the fourth chapter. The experiments were performed at the IMAT beamline and VESUVIO beamline, located at the ISIS neutron and muon source. I personally contributed to data reduction, analysis and interpretation. In this chapter are described the background noise corrections that were implemented on imaging and transmission data. Moreover, analyzing imaging data I was able to determine a characteristic time for the ortho-para conversion that is significantly lower than that of free hydrogen, therefore demonstrating that the MOF acts as a catalyst for this reaction. I performed the analysis on the imaging data on multiple regions of interests, showing that this technique provides the possibility to explore the spatial distribution of the

sample, which renders it particularly appealing for industrial and engineering applications. Processing transmission data acquired at the VESUVIO beamline, I compared the experimental cross section of adsorbed molecular hydrogen at 30 K, to theoretical simulations. Results indicate that the three dimensional model is not suitable to represent adsorbed hydrogen, suggesting that this system could be better represented by a hindered rotor.

Chapter 1

Hydrogen storage

Molecular hydrogen (H_2) has gained increasing attention in the framework of efficient and green transport technologies. During the last decades a substantial effort has been directed towards the problem of hydrogen storage: to fully exploit this resource we need cheaper and more efficient ways to safely store and transport molecular hydrogen. In this chapter we will briefly discuss the main properties of molecular hydrogen, as well as different storage techniques. We will then focus on one of the possible solutions: Metal Organic Frameworks (MOFs).

1.1 Molecular hydrogen

Molecular hydrogen (H_2) is composed of two hydrogen atoms, each with a half-integer nuclear spin. H_2 molecules can be found in two possible modifications, depending on whether their nuclear spins are parallel or antiparallel. When the spins are parallel the molecule is said to be in the ortho modification. The ortho-hydrogen state has a total nuclear spin S=1, as a consequence the component along the z axis can have one of the three values S_z=-1,0,1. These triplet states are degenerate in absence of a magnetic field, their wave functions are symmetric and can be written in terms of the spin wave functions of the proton 1 and 2 as:

$$|\psi_{S,S_z}\rangle = \alpha(1)\alpha(2)$$
$$|\psi_{S,S_z}\rangle = \alpha(1)\beta(2) + \alpha(2)\beta(1)$$
$$|\psi_{S,S_z}\rangle = \beta(1)\beta(2)$$

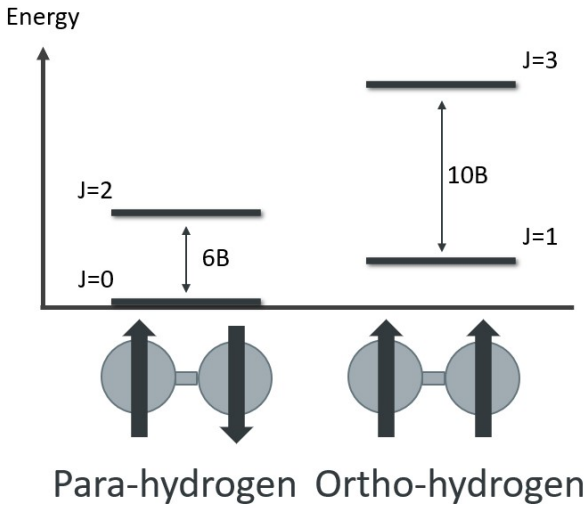

Figure 1.1: Ortho- and para-hydrogen modifications, rotational levels are reported for free hydrogen (3D rotor).

On the other hand, when the spins are antiparallel it is called para-hydrogen, and has a total nuclear spin S=0. This results in the singlet state with anti-symmetric wavefunction:

$$|\psi_{S,S_z}\rangle = \alpha(1)\beta(2) - \alpha(2)\beta(1) \tag{1.1}$$

When the hydrogen molecule is free to move in space, its energy can be stored in multiple degrees of freedom. In fact, free molecular hydrogen can rotate about its centre of mass, vibrate along its axis and move in the space. Moreover we can identify electronic and nuclear motions of the two hydrogen atoms. To study such a complicated system we usually have to perform multiple approximations: as an example, free hydrogen can be considered an ideal gas, neglecting the interactions between molecules, moreover electronic motion can be treated using the Born–Oppenheimer approximation. For the purpose of this work, we are more concerned with molecular motion. Here we can solve the Hamiltonian assuming that the rotational, vibrational and translational motions are independent from each other and from molecular spin.

Since protons have nuclear spin equal to $\frac{1}{2}$, the total wavefunction that describes molecular motion has to be anti-symmetric. While translational, vibrational and electronic motion have no influence on the symmetry of the nuclear wave function, rotations and spin flips can change its parity, therefore, to guarantee that the total

wave function is anti-symmetric, the product of rotational and nuclear spin wave functions has to be anti-symmetric. It is therefore relevant to discuss the rotational states of H_2.

Rotational states of H_2

The theory behind the three dimensional rotor model is here briefly discussed as we are going to adapt it to the two dimensional case. We describe rotational states of a hydrogen molecule neglecting vibrational and translational motion, therefore approximating the molecule as a rigid rotor. In the case of molecular hydrogen, the rigid rotor is composed of two identical atoms of mass m separated by a mean distance a, that rotate as a whole around the centre of mass. The moment of inertia of this system, taken into account that the two atoms have the same mass m and same distance from the centre of mass $\frac{a}{2}$, is:

$$I = \frac{1}{2}ma^2 \tag{1.2}$$

To solve the Schrodinger equation of a rigid rotor we assume the bond length to be constant ($r = a$), which means that the partial derivative with respect to r does not contribute because r does not vary. Writing the Hamiltonian in spherical coordinates we get:

$$-\frac{\hbar^2}{2I}\left[\frac{1}{\sin\theta}\frac{\partial}{\partial\theta}\sin\theta\frac{\partial}{\partial\theta} + \frac{1}{\sin^2\theta}\frac{\partial^2}{\partial\varphi^2}\right]|\Theta(\theta)\Phi(\varphi)\rangle = E|\Theta(\theta)\Phi(\varphi)\rangle \tag{1.3}$$

Here the wave function is composed of two separate wave functions that depend only on the variables θ and φ respectively. In order to separate the variables we can multiply each side by $\dfrac{2I}{\hbar^2}$ and $\dfrac{-\sin^2\theta}{\Theta(\theta)\Phi(\varphi)}$ so that:

$$\frac{1}{\Theta(\theta)\psi(\varphi)}\left[\sin\theta\frac{\partial}{\partial\theta}\sin\theta\frac{\partial}{\partial\theta} + \frac{\partial^2}{\partial\varphi^2}\right]\Theta(\theta)\Phi(\varphi) = \frac{-2IE\sin^2\theta}{\hbar^2} \tag{1.4}$$

Noticing that $\dfrac{\partial}{\partial\theta}$ only acts on $\Theta(\theta)$ and $\dfrac{\partial^2}{\partial\varphi^2}$ only acts on $\Phi(\varphi)$, we can separate variables as:

$$\frac{1}{\Theta(\theta)}\left[\sin\theta\frac{\partial}{\partial\theta}\left(\sin\theta\frac{\partial}{\partial\theta}\right)\Theta(\theta) + \left(\frac{2IE}{\hbar^2}\sin^2\theta\right)\Theta(\theta)\right] = -\frac{1}{\Phi(\varphi)}\frac{\partial^2}{\partial\varphi^2}\Phi(\varphi) \tag{1.5}$$

Equation 1.5 implies that the two expressions have to be equal for every value of θ and φ, therefore they must be equal to a constant, that we call m_J^2. This allows us to separate variables obtaining:

$$\sin\theta\frac{d}{d\theta}\left(\sin\theta\frac{d}{d\theta}\right)\Theta(\theta)+\frac{2IE}{\hbar^2}\sin^2\theta\Theta(\theta)=m_J^2\Theta(\theta) \tag{1.6}$$

and

$$\frac{d^2}{d\varphi^2}\Phi(\varphi)=-m_J^2\Phi(\varphi) \tag{1.7}$$

The second one has immediate solution. Normalizing the eigenfunction and imposing cyclic boundary conditions, which signify that φ and $\varphi+2\pi$ have to be the same angle in the three dimensional space, we find that:

$$\Phi_m(\varphi)=\frac{1}{\sqrt{2\pi}}e^{\pm im_J\varphi} \tag{1.8}$$

where

$$m_J=\cdots,-3,-2,-1,0,1,2,3,\cdots \tag{1.9}$$

On the other hand, the solutions to 1.6 are found to be the associated Legendre functions, where it is required that:

$$\frac{2IE}{\hbar^2}=J(J+1) \tag{1.10}$$

Therefore we can say that equation 1.5 requires the energy to be quantized as:

$$E=J(J+1)\frac{\hbar^2}{2I}=J(J+1)B \tag{1.11}$$

where $B=7.35\ meV$ ($B=59.3\ cm^{-1}$) for molecular hydrogen [2]. It is important to note that every level is (2J+1)-degenerate since it is associated with values of m_J for which it has to be true that $|m_J|\leq J$. The eigenfunctions of 1.5, given by the product of $\Theta(\theta)$ and $\Phi(\varphi)$ are known as spherical harmonics. Spherical harmonics are labeled by the quantum numbers J and m_J, in particular the even states are labeled by even Js and odd states are labeled by odd Js.

As mentioned before the total wave function has to be anti-symmetric, this means that para-hydrogen will exist in even angular momentum states, J=0, 2, 4, ..., while ortho-hydrogen will have odd rotational states J=1, 3, 5, ...; it can

be shown that the energy of the singlet is in fact around 15 meV lower than that of the triplet [3]. As a consequence, the two modifications have different physical properties.

Thermodynamic properties of ortho- and para- hydrogen

To describe the thermodynamic properties of a system at equilibrium it is useful to construct its partition function. The total partition function of molecular hydrogen depends on multiple terms that arise from the different possible motions mentioned before. If we use the the Born–Oppenheimer, ideal gas, and rigid-rotor harmonic-oscillator approximations we can write the total partition function decoupling each degree of freedom as:

$$Z_{\text{tot}} = Z_{\text{elec}} Z_{\text{vib}} Z_{\text{rot}} Z_{\text{trans}} Z_{\text{spin}} \tag{1.12}$$

In order to focus on the differences between the two hydrogen modifications we can consider only the ortho- and para- partition functions, which are given by the product of the spin and rotational partition functions:

$$Z_{\text{ortho}} = Z_{\text{S,triplet}} Z_{r,\text{odd}} = 3 \sum_{J=1,3,5,\ldots} (2J+1) e^{-J(J+1)B/k_B T} \tag{1.13}$$

and

$$Z_{\text{para}} = Z_{\text{S,singlet}} Z_{r,\text{even}} = 1 \sum_{J=0,2,4,\ldots} (2J+1) e^{-J(J+1)B/k_B T} \tag{1.14}$$

While the total partition function of a system containing both modifications is:

$$Z_{\text{rot},S} = 1 \sum_{J=0,2,4\ldots} (2J+1) e^{-J(J+1)B/k_B T} + 3 \sum_{J=1,3,5,..} (2J+1) e^{-J(J+1)B/k_B T} \tag{1.15}$$

Knowing these functions, we can calculate the probability that the hydrogen molecule is in the ortho- or para-state, and therefore their concentrations, as a function of temperature. The relative concentrations of ortho- and para-hydrogen calculated using 1.13, 1.14 and 1.15 are shown in figure 1.2. We find that the relative populations of oH_2 and pH_2 depend on the temperature at which we observe the system: at room temperature their concentration depends primarily on the

singlet to triplet ratio. This means that 75% of the hydrogen molecules will be in the ortho- modification, and 25% in the para- modification. This changes at lower temperatures, in fact when approaching the ground state it becomes more convenient for the oH_2 to undergo an "ortho-para conversion" (opC) to the lower energy state [4].

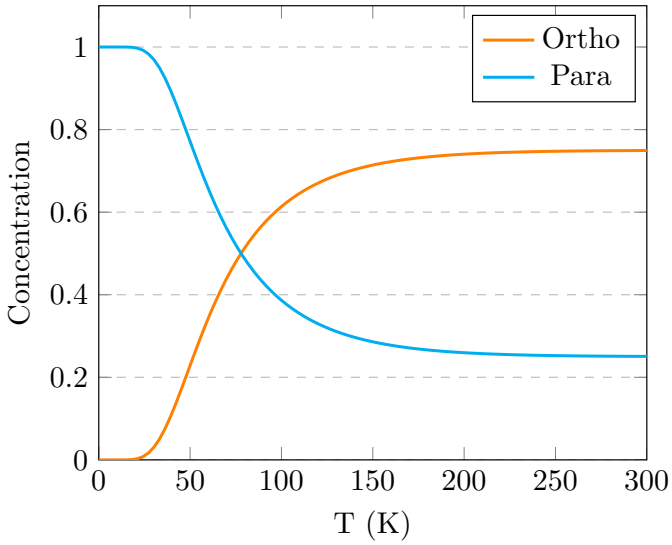

Figure 1.2: Ortho- and para-hydrogen concentration as a function of temperature, calculated for the case of free molecular hydrogen, which can be represented with the 3D rotor model.

The conversion has been investigated with infrared [5], Raman spectroscopy [6], thermal conductivity and NMR measurements [7][8], as it is also particularly interesting for spallation neutron sources. In fact pH_2 can be used as a neutron moderator, to optimize the experimental conditions. Recently, effort has been directed into finding a catalyst to expedite the reaction. It is important to take into account that the conversion phenomenon has undesired consequences for the hydrogen-storage industry. In fact, the conversion from oH_2 to pH_2 is an exothermic reaction, that can cause the evaporation of neighboring molecules. This process is known as "boil-off" and is relevant to hydrogen storage applications, as well as space applications [9]. Energy released during boil-off is of 525 kJ/kg at 20 K [9].

Moreover, using the ortho- and para- partition functions, it is possible to show that the two modifications have very different rotational, and therefore total, heat capacities at constant volume. The heat capacity at constant volume is defined

as:

$$C_V = \frac{\partial \langle E \rangle}{\partial T} \tag{1.16}$$

where:

$$\langle E \rangle = -\frac{\partial \ln Z_{\mathrm{rot,S}}}{\partial \beta} \tag{1.17}$$

Heat capacities at constant volume are shown in figure 1.3.

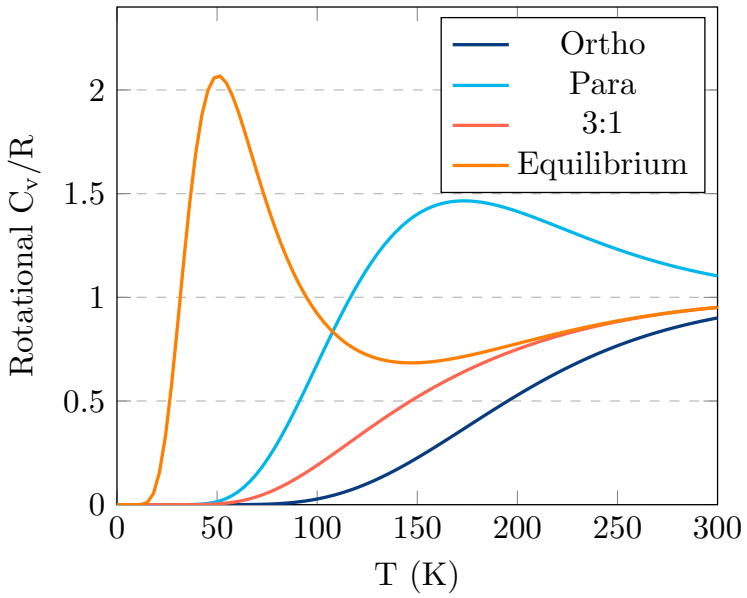

Figure 1.3: Ortho- and para-hydrogen rotational heat capacities at constant volume, normalized by the gas constant R, respectively in blue and cyan. The heat capacity is also shown for normal hydrogen with a concentration ratio of 3:1 (orange) and for the ratio given at the specific equilibrium temperature (violet). These are calculated for free molecular hydrogen, which can be described with a 3D rotor model.

These curves can be calculated by substituting the respective partition functions into equations 1.16 and 1.17.

From figure 1.3 it is possible to notice the difference between the rotational heat capacities of the two modifications. Moreover the picture shows the heat capacities for two other systems, composed of both ortho- and para-hydrogen molecules. The system marked as "equilibrium" has a concentration that varies depending on the temperature, as shown in figure 1.2, and can be calculated using the total

partition function. However this curve differs greatly from the experimental data, which is more similar to the curve marked as "3:1". The latter presents a fixed concentration ratio, that corresponds to that of room temperature, which means that the heat capacity is given by:

$$(C_V)_{\mathrm{rot,S}} = \frac{3}{4}(C_V)_{\mathrm{rot,S}}(\mathrm{ortho}) + \frac{1}{4}(C_V)_{\mathrm{rot,S}}(\mathrm{para}) \tag{1.18}$$

This happens because the ortho-para conversion for free hydrogen in an incredibly slow reaction (characteristic conversion time of around 79 hours [10]), so when H_2 is cooled the ratio continues to be close 3:1 for a long period of time.

Another relevant difference between the two isomers is in their neutron scattering cross section, which will be discussed in depth in chapter 2.

1.2 Hydrogen storage techniques

Recently molecular hydrogen (H_2) has gained increasing attention in the field of efficient and green transport technologies. Because of its high energy density, hydrogen is currently one of the most promising candidates to replace carbon-based energy sources. In fact hydrogen has a power density of 33.3 kW h kg^{-1} while that of methane and gasoline are respectively 13.9 kW h kg^{-1} and 12.4 kW h kg^{-1}. In addition, hydrogen is very abundant in nature and non-polluting.

During the last decades a substantial effort has been directed towards the problem of hydrogen storage: to fully exploit this resource we need cheaper and more efficient ways to safely store and transport molecular hydrogen. Currently hydrogen is stored in cryogenic pressurized tanks in the liquid form. The size of the tank can range between 1.5 m^3 and 75 m^3. Liquid hydrogen has higher density compared to the pressurized gas, however liquefaction requires a lot of energy and can be very expensive. This storage method is currently applied for many applications but has proved to be particularly unfit for transport technologies. In fact, cryogenic storage is convenient if large quantities are produced and if the application requires long storage periods [11].

Especially in the field of transportation, it is obviously impractical and unsafe to store on a vehicle large pressurized tanks that require daily refilling. For this reason, the properties of many different materials that have the capacity of adsorbing hydrogen under specific conditions have been explored. Based on the way the material interacts with the H_2 molecules, one can divide hydrogen storage materials into two categories: chemisorption-based materials and physisorption-

based materials. The first category includes all of those materials that chemically bond with the hydrogen atoms. In this case, the ability to bond, as well as the stability of the bond, strongly depend on the temperature and pressure of the system. Moreover those processes could be irreversible, or have a specific adsorption or desorption activation energy. We can divide chemisorption-based materials into two classes: on-board reversible hydrides, which are all of those hydrides that could be recharged on a vehicle, and off-board regenerable hydrides, that present a more complex mechanism of re-hydrogenation. Examples of on-board reversible hydrides are interstitial metal hydrides, covalent metal hydrides, complex covalent hydrides. Off-board regenerable hydride materials are ammonia borane, hydrocarbons and alane.

In physisorption-based materials the mechanism that regulates adsorption relates on van-der-Waals forces. In this case the attraction is relatively weak and it is due to electric forces that do not modify the chemical structure of the hydrogen molecule. Therefore the adsorption is easily reversible and the process never presents an activation energy. Physisorption materials are highly porous materials such as zeolites clathrates, organic polymers, and metal-organic frameworks. The storage capacity of these materials depends on the size shape of the pores, as well as their surface area and chemical composition. The weak intermolecular forces guarantee fast adsorption and desorption kinetics, which is relevant for on-board loading, as well as fast fuel availability. However, the weak nature of the bond entails that high storage capacities can only be reached at low temperature and/or high pressure. In the next section we will discuss one the most promising class of physisorption materials, underlying their main characteristics as well as the state of the art in the field of hydrogen storage [12].

1.3 Metal organic frameworks (MOFs)

Metal–organic frameworks (MOFs) are crystalline materials composed of metal ions linked together by organic ligands, forming a highly microporous network. While the firsts porous three-dimensional networks dates back to the late 1980s [13], MOFs were not developed until later, when it was found that aggregating metal ions with carboxylate rigid organic ligands allowed to produce a crystalline structure with high stability as well as high porosity. MOFs are in fact composed of metal–carboxylate subunits which constitute the nodes of the framework, and some other organic linker, on which depends the structure of the network. The wide variety of metal ions and organic ligands makes it possible to design many

different frameworks, which can differ in size of the pores and chemical properties. MOFs were firstly suggested as hydrogen storage materials in 2003 with Rosi et al. [14] and Ferey et al. [15]. They firstly showed that hydrogen can be stored by physisorption processes in MOFs. Rosi et al. reported an hydrogen maximum uptake of 45 mg per gram of MOF-5 (4.5 weight %) at a temperature of 78 K and pressure lower than 1 bar. They also reported the uptake at room temperature, which was found to increase linearly with pressure, giving 1.0 weight % at 20 bar. Rosi points out that, although very sensitive to preparation conditions, the capacity of MOF-5 at room temperature is comparable to the highest capacity of carbon nanotubes at cryogenic temperatures. Ferey et al. studied MIL-53 with two different metal ions Al^{3+}, Cr^{3+}, reporting a storage capacity at 77 K and 1.6 MPa of 3.8 wt.% and 3.1 wt.% respectively. Those findings firstly showed the potential of MOFs as hydrogen storage materials, and initiated a cascade of reports on the subject.

1.3.1 Investigation techniques

Hydrogen adsorption in MOFs is often investigated using vibrational spectroscopies, such as Inelastic Neutron Scattering (INS). This technique is particularly useful to identify hydrogen binding sites and explore the rotational transitions of adsorbed molecules. Using INS it is possible to show that MOFs present multiple binding sites, however assigning those sites to specific locations in the framework structure can be complicated, and it is usually necessary to integrate the results with computational methods. As an example, Rosewell used INS in 2005 to study the adsorption of molecular hydrogen in four different MOFs (IRMOF-1, IRMOF-8, IRMOF-11, and MOF-177) constructed from the same initial unit. All of these MOFs showed multiple adsorption sites. Implementing Monte Carlo simulations they were able to identify the strongest binding site of MOF-5 in the corners of the larger pores, on the faces of the $Zn_4O(O_2C-)_6$ clusters. Despite the similar structures of the four MOFs, the nature of the hydrogen bonds in each structure is found to vary considerably, showing that the organic units play a significant role in the adsorption process [16]. Similar findings for MOF-5 were reported by Mulder in 2008, who, using INS, identified five adsorption sites instead of the four found by Rowsell [17]. INS is also particularly useful to investigate the occupation order of the sites: it is shown that stronger binding sites are always filled first, if the pressure is increased or the temperature lowered, weaker binding sites are then filled [18]. Moreover INS allows us to investigate rotational properties of adsorbed

hydrogen [19][20].

Another technique used to determine hydrogen location inside the MOFs is neutron powder diffraction. This technique is particularly useful to determine the distance between constituent elements of the framework as well as between hydrogen molecules[18][21]. Moreover, Infrared adsorption spectroscopy can be performed to investigate the nature of the bond, measuring the binding enthalpy of each adsorption site. This reflects the energy change of the molecule from its free state to the bound state, which can indicate a stretching [18] [21]. It is shown by Nijem et al. that the IR shifts do not depend on the binding energy, but on the chemical environment, specifically H_2-H_2 interactions [18].

1.3.2 Surface area, pore dimension and open metal sites

MOFs are typically categorized by their surface area and pore dimensions. Their surface area is usually measured using BET model: this method is conventionally used in literature even though it is not perfectly appropriate for microporous materials such as MOFs. Hirscher and Panella report the hydrogen storage capacity as a function of BET specific surface area for many porous materials. The general trend shows a linear correlation between storage capacity and surface area. This indicates that the hydrogen uptake is independent from the material of the framework, but instead depends on its shape [22]. However, at a certain temperature the maximum uptake is reached at a pressure that depends on the specific material and on the heat of adsorption of each bond.

The heat of adsorption, which quantifies the strength of the interaction between adsorbate and adsorbent, is mainly influenced by the pore size. In particular, it was found that a higher heat of adsorption is associated with smaller pore size [23], this is because smaller pores allow the molecule to interact with the several atoms that surround it, instead of only one surface. Monte Carlo simulations contribute to demonstrate that a higher hydrogen uptake is associated with smaller pores and higher specific surface area [24]. Even though it is hard to imagine that a MOF will be able to satisfy the characteristics for room temperature storage, great effort is being put into synthesizing the MOFs with the best possible properties. Moreover, a study on Zeolite-like metal-organic frameworks (ZMOFs) demonstrates that the heat of adsorption is significantly improved by the presence of an electrostatic field inside the pore [25]. The electrostatic field can be introduced by having a charged framework, adding cations as in zeolites.

Another possible way to increase the heat of adsorption is to introduce open

bonds in the structure. MOFs with open metal sites have attracted great interest in the field of hydrogen storage. Open metal sites are constituted of metal ions centres with unsaturated bonds. Usually they can be achieved by weakly linking the metal to a solvent molecule, that is liberated during heating, leaving the bond exposed to the void region. Not all MOFs can present open metal sites: the framework needs to be sufficiently rigid in order to sustain the structure without collapsing [26]. It is also interesting to notice that results of experiments and calculations suggest that the strength of the bond between the cation and the hydrogen molecule depends on the ionic radius of the cation [27]. Adding open metal sites is one of the most effective way to increase the heat of adsorption, therefore those types of MOFs are the most studied.

1.3.3 MOFs for hydrogen storage: HKUST-1

Since the late 90s, when MOFs started becoming popular in many research fields, more than 90'000 structures have been synthesized and over 500'000 predicted [28], however not all of them are relevant for hydrogen storage applications. One of the most studied MOFs in this field is MOF-5 (or IRMOF-1), this MOF is particularly interesting because of its simple preparation process and cheap chemical constituents. Here inorganic $[OZn_4]^{6+}$ groups are joined to an octahedral array of $[O_2C{-}C_6H_4{-}CO_2]^{2-}$ (1,4-benzenedicarboxylate, BDC) groups. Rosi reports for this MOF an apparent surface area of 2500 to 3000 m^2g^{-1}. As mentioned before, its measured uptake at 78 K is of 45 mg of H_2 per gram of MOF-5 (4.5 weight%, which means 17.2 H_2 per $Zn_4O(BDC)_3$ formula unit). Rosi identifies two main adsorption sites for this MOF, associated with the Zn and the BDC linkers. But data shows that further increasing the loading could result in the emergence of new peaks, associated with different adsorption sites. MOF-5 was also the subject of numerous computational studies. Sillar et all use Density functional theory (DFT) and second-order Møller-Plesset perturbation theory (MP2) to simulate the interaction between H_2 and different elements of the MOF, taking into account dispersion interactions and zero-point vibrational energies [29]. It's found that the stronger site is at the $OZn_4(O_2Ph)_6$ node.

It is possible to construct slightly different MOFs, starting from the same initial unit $Zn_4O(O_2C{-})_6$, by changing the organic linking units. MOFs similar to MOF-5 are known as IRMOFs (isoreticular MOFs). As an example Rowsell studied MOF-5 as well as IRMOF-8, IRMOF-11, and MOF-177. Despite the similar structures, the nature of the hydrogen bonds in each MOF varies considerably, showing that

the organic units play a significant role: the adsorption isotherms show how the four samples present different capacities for hydrogen uptake.

Another example of interesting MOFs are zeolite-like MOFs which are anionic and have exchangable extra-framework cations. Here the nature of the binding is strongly influenced by the strong electrostatic field in the pores [25].

Some of the most promising MOFs, in the field of hydrogen storage, are those with unsaturated metal centers. An example of these is given by another family of isostructural MOFs, known as: M_2(dobdc) (M = Mg, Mn, Fe, Co, Ni, Zn) ($dobdc^{4-}$ = 2,5-dioxido-1,4-benzenedicarboxylate) which present exposed M_2^+ cation sites. Of these, the MOF with the Ni cation shows the shortest hydrogen-metal distance [30][31].

Other MOFs with open metal sites, interesting for hydrogen storage applications, are iron-based sodalite-type MOFs [32], fcu-MOFs [20], covalent organic frameworks (COFs) [20], isostructural MOFs of the type M-CUK-1 [33], as well as $Cr_3(BTC)_2$ [21] and In-soc-MOF [34].

For the purpose of this work we will focus on one particular open metal site MOF, which was used in the experiments: HKUST-1. This MOF is named after the Hong Kong University of Science and Technology, but is also known as MOF-199 or Basolite 300. This MOF is composed of copper nodes with 1,3,5-benzenetricarboxylic acid links between them ($Cu_3(BTC)_2$), disposed as in figure 1.4, for a total of 156 atoms. Here the Cu atoms, in the dehydrated phase, are unsaturated, favoring high binding enthalpies.

The largest pores, shown in figure 1.4, have a diameter of 9 Å and are formed by 12 dinuclear $Cu_2(OOC)_4$ subunits, arranged in a cuboctahedron. The second largest pores are composed of four benzene rings and have a 5 Å diameter. This MOF can be synthesized using hydrothermal methods. At 77 K this material adsorbs up to 2 wt % at 100 Pa (0.001 bar). The powder diffraction pattern showed the structure slightly expanding during the loading of gas. The most favored binding site lies next to the Cu atoms, specifically it occupies the unsaturated axial sites of the dinuclear Cu center, and has a distance of 2.39 Å from the Cu atom. Peterson et al. report the order in which the other binding sites are filled during loading, showing that it is consistent with the fact that smaller pores are filled first [35]. Brown et al. proves the rotational motion of hydrogen inside the main adsorption site to be slightly hindered: this means that the H_2 molecule has a tendency to lie in a plane perpendicular to the Cu-Cu bond [36].

In the following sections we will thoroughly discuss how adsorbed hydrogen behaves inside the pores, in particular we will focus on the kinetics of the ortho-

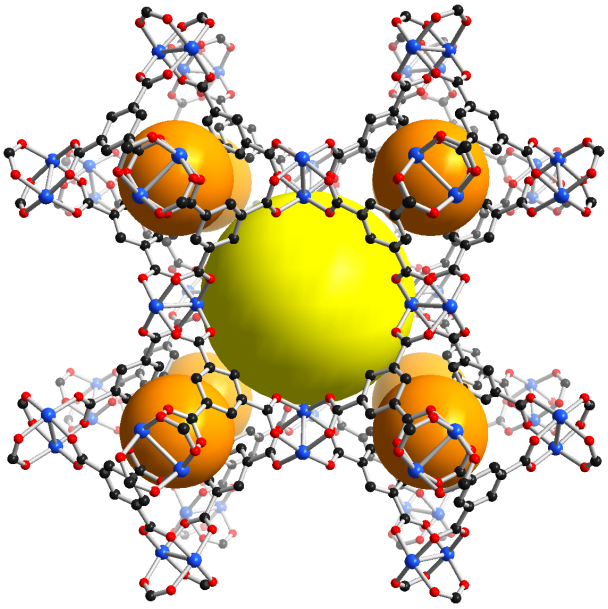

Figure 1.4: Representation of HKUST-1 metal organic framework, the spheres represent the pores of the framework.

para conversion, which appears to be catalyzed by the framework. We will then discuss the rotational levels of adsorbed hydrogen, showing how the rotation is often hindered in the presence of the adsorbant.

1.4 Kinetics of the catalysed ortho-para conversion

The ortho-para conversion happens at low temperatures, when a change of the rotational state from J=1 to J=0 occurs simultaneously with a total nuclear spin change, from S=1 to S=0, to guarantee the anti-symmetry of the wave function. The transition between states of different parity is not spontaneous, therefore it requires an external magnetic field, that in the case of free hydrogen is provided by neighbouring oH_2, that rotate producing a dipole. Here the rate of the conversion can be expressed in terms of the oH_2 concentration o as:

$$-\frac{do}{dt} = k_2 \frac{o(o - o_e)}{1 - o_e} \tag{1.19}$$

Where o_e is the concentration of oH_2 at equilibrium, and k_2 is the conversion rate constant. For liquid hydrogen at 15 K and 0.66 bar the value of the rate

constant can be found to be $k_2 = 0.0143$ $\mathrm{h}^{-1}\mathrm{o}^{-1}$. This results in a characteristic conversion time of around 79 hours [10]. While the conversion of free hydrogen is particularly slow, when the molecules are bound to a surface, its magnetic field can function as a catalyst of the reaction. This is observed in both magnetic and diamagnetic materials and can be attributed to potential anisotropies at the microscopic level. In the presence of a catalyst the conversion rate changes, in particular we have to distinguish the case where the surface is saturated, and the case where some of the adsorption sites are empty. The latter can usually be expressed as a fist order interaction as:

$$-\frac{do}{dt} = k_1 o \tag{1.20}$$

According to this, the ortho-hydrogen concentration as a function of time can be written as:

$$o(t) = o_0 e^{-\frac{(t-t_0)}{\tau}} \tag{1.21}$$

Where the characteristic time τ is defined as the inverse of the conversion rate constant:

$$\tau = \frac{1}{k_1} \tag{1.22}$$

Which gives us a time scale of the reaction. On the other hand when the surface is saturated the conversion rate may be independent from the concentration of ortho-hydrogen, and can be written as:

$$-\frac{do}{dt} = k_0 \tag{1.23}$$

The kinetics of the ortho-para conversion is particularly interesting in the field of hydrogen storage. Many materials that are studied for storage applications, are able to adsorb the H_2 molecules without modifying their chemical bonds. MOFs are one of those, and can be shown to act as a catalyst of the ortho-para conversion [37], therefore it is particularly important to investigate how the hydrogen molecules interact with the framework [38].

1.5 Rotational states of adsorbed H_2

Rotational levels of free hydrogen, in the gaseous, liquid or solid state, can be described using a free rotor model, also known as 3D rotor model. As mentioned before, the wave functions of the 3D rotor are the spherical harmonics $Y_{Jm_J}(\theta, \phi)$. They are labelled with two quantum numbers, the rotational quantum number J and the quantum number m_J that defines the projection of the angular momentum along the z-axis. The system is $(2J+1)$-fold degenerate and the rotational energies are given by:

$$E_{3D}(J) = BJ(J+1) \tag{1.24}$$

In some cases, the 3D rotor model can be used to describe the rotational states of adsorbed hydrogen, however, depending on the specific surface and the nature of the bond, the rotational motion could be hindered. As an example, H_2 molecules adsorbed by the Cu(100) surface, in absence of defects, can be described as a quasi-free 3D rotor, because the Cu(100) surface is particularly flat. On the other hand, when H_2 is adsorbed by the Cu(510) surface things change. Using electron-energy-loss spectroscopy, as well as density-functional calculations, Bengtsson and Svensson showed that the H_2 adsorbed on the steps on the Cu(510) surface is constrained to rotate as hindered rotor [39] [40].

This behaviour was modelled for the first time in 1976 by Silvera and Nielsen: they used inelastic neutron scattering (INS) to observe H_2 and D_2 molecules adsorbed by activated alumina. They were able to observe a broad peak around the value of B, as expected for a two dimensional rotor, and no peak around 2B, which one would have expected for a 3D rotor. The model they proposed for this system is that of a rotational Hamiltonian with a hindering potential:

$$H_{hind} = B\left[-\frac{1}{sin\theta}\frac{\partial}{\partial\theta}\left(sin\theta\frac{\partial}{\partial\theta}\right) + \frac{J_z^2}{sin^2\theta}\right] - \Phi_0 sin^2\theta \tag{1.25}$$

Where θ is the angle between the molecular axis and the direction z, which is perpendicular to the surface. If Φ_0 is assumed positive, the potential is hindered along the direction defined by the angle $\theta = \frac{\pi}{2}$, this means that the molecule is parallel to the surface. In absence of the hindering potential, at $\Phi_0 = 0$, the eigenstates of this Hamiltonian are those of the three-dimensional rotor. When $\Phi_0 \to \infty$ the lower energy states are those of the 2D rigid rotor, its spectrum is defined as:

$$E_{2D}(J) = BJ^2 \tag{1.26}$$

On the other hand, if Φ_0 is negative the molecule is oriented perpendicularly to the surface, therefore when $\Phi_0 \to -\infty$ it can no longer rotate. In this case the system is said to behave as a 1D rotor: it doesn't show rotational states, but can only vibrate along the z direction. It is also possible to express the hindering potential in terms of $cos^2(\theta)$ by redefining the sign of the potential. Silvera concludes that the most fitting model for hydrogen adsorbed on the activated alumina is a 1D modified model, this model however does not take into account translational motion. Moreover the model fails to predict high energy transitions.

Bengtsson and Svensson investigated rotational as well as vibrational motion for the H_2 adsorbed at the step edges of Cu(510): The Hamiltonian proposed by Silvera and Nielsen was used to investigate the rotational motion, while DFT total-energy calculations were implemented to construct a 3D potential-energy surface used to simulate vibrational motion. The transition energies for a hindered 3D rotor as a function of the hindering strength Φ_0 is reported in [40]. Here we calculated the energy levels as well as the transition energies for a hindered rotor, by numerically solving the eigenvalue equation for Hamiltonian in 1.25.

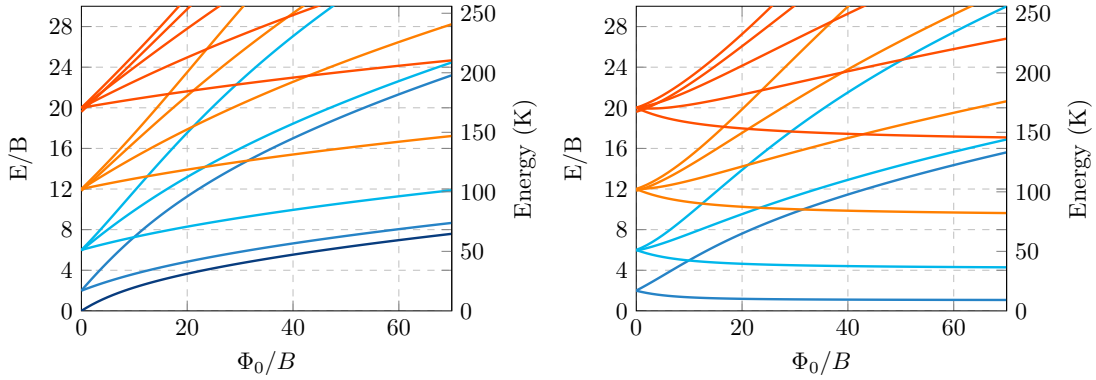

Figure 1.5: Energy levels (a) and transition energies (b) for a 3D rotor subject to a hindering potential as a function of the scaled hindering strength Φ_0. In the right axis of each plot, energy was normalized using the Boltzmann constant in order to express the energy in Kelvin. This allows us to infer what levels would be occupied at a certain temperature. The calculations were performed using Wolfram Mathematica, assuming an hindered potential equal to $\Phi_0 sin^2\theta$.

In figure 1.5a and 1.5b they are reported as a function of the scaled hindering

potential Φ_0. We chose to reproduce calculations shown in [40] as they will be useful in the following chapters.

Figure 1.5a represents the energy levels of the hindered rotor, on the right axis we normalized energy by the Boltzmann constant, therefore expressing it as a function of temperature, so that one can roughly infer how many levels would be occupied at a certain temperature. In figure 1.5b each line shows the transition energy from the state $(J, m_J) = (0, 0)$, to states with $(J, m_J) \neq (0, 0)$. When $\Phi_0 = 0$ the states are m_J-degenerate, however, when the hindering potential is turned on, each level splits for different m_J. For each J, the state with the lowest energy is the one that approaches the 2D rotor energy state given by BJ^2. As a result, when the hindering barrier is sufficiently high, the first accessible states are well represented by a two dimensional rotor.

Knowing the energy levels, it is possible to compute the partition function of the hindered rotor, for a specific hindering strength. The partition functions of confined ortho- and para-hydrogen molecules can be written as:

$$Z_{\text{ortho}} = Z_{\text{S,triplet}} Z_{r,\text{odd}} = 3 \sum_{J=1,3,5,\ldots} \sum_{m_J=0}^{J} g_{m_J} e^{-E_{Jm_J}/k_B T} \tag{1.27}$$

and

$$Z_{\text{para}} = Z_{\text{S,singlet}} Z_{r,\text{even}} = 1 \sum_{J=0,2,4,\ldots} \sum_{m_J=0}^{J} g_{m_J} e^{-E_{Jm_J}/k_B T} \tag{1.28}$$

where E_{Jm_J} are the energies levels shown in figure 1.5a, evaluated at a specific hindering strength, and g_{m_J} is the degeneracy of each level, specifically:

$$g_{m_J} = \begin{cases} 1 & \text{if } \; m_J = 0 \\ 2 & \text{else} \end{cases} \tag{1.29}$$

Using equations 1.27 and 1.28 we calculated the ortho- and para-concentrations for a hindering strength of $\Phi_0 = 70\ B$. In figure 1.6 it is reported a comparison between the 2D and 3D concentrations.

Similarly to the 3D case, it is possible to calculate the heat capacities of the ortho- and para-hydrogen when their rotational motion is hindered. These heat capacities are shown in figure E.1, and it is interesting to notice that their shape is similar to those of the 3D case, but they are slightly smaller since the rotation is hindered.

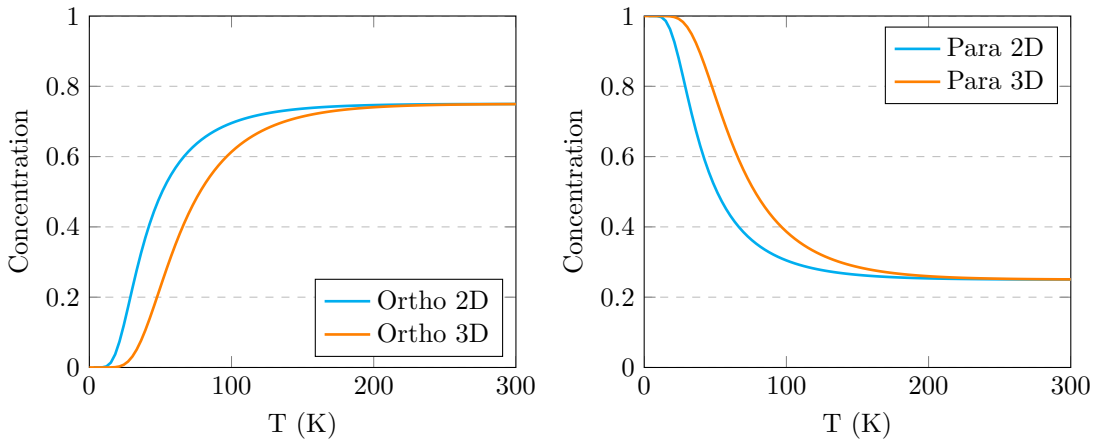

Figure 1.6: Comparison between the ortho- and para-hydrogen concentrations of a 2D and 3D rotors as a function of temperature.

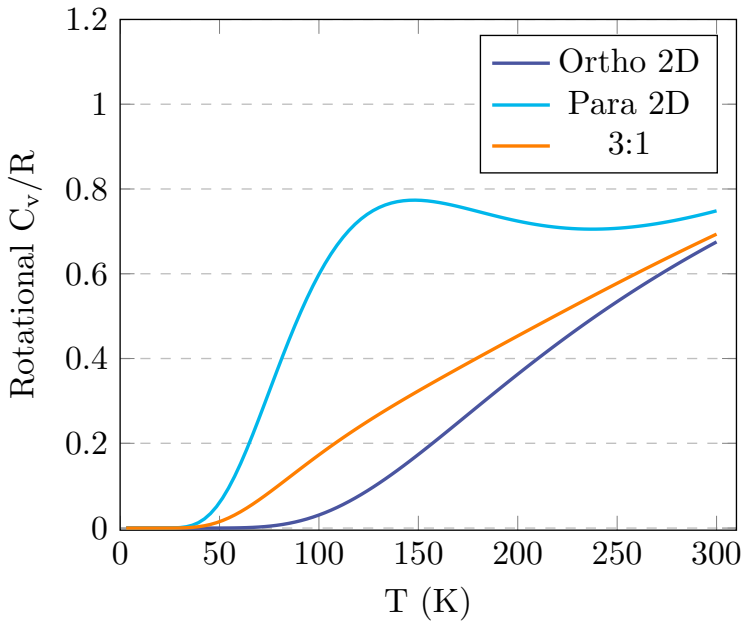

Figure 1.7: Ortho- and para-hydrogen heat capacities for a 2D rotor, normalized by the gas constant R.

In addition to the theoretical calculations implemented by Bengtsson, Teillet-Billy and Gauyac present a theoretical study where the sudden rotational approximation, usually used for free molecules, is applied to the case of hydrogen molecules

adsorbed by the Cu(510) surface. The model makes it possible to justify the various peaks in the electron energy loss spectrum [41].

The two dimensional rotor behaviour can be observed not only on stepped surfaces and defects, but also in porous materials. Two different examples are provided by Ramirez-Cuesta et al. In 2001 they studied molecular hydrogen adsorbed by a cobalt aluminophosphate catalyst (CoAIPO). Here, dihydrogen was adsorbed at the cobalt(III) sites. From both INS experiments and DFT simulations it is clear that absorbed hydrogen molecules can not be treated as unhindered 3D rotors. In particular, two types of bonds are detected at the Co(III) site: a weaker bond is present when the hydrogen molecule is perpendicular to the surface of the catalyst, in this case we observe peaks typical of a 1D rotor. Conversely, when dihydrogen is bound parallel to the surface, the bond is stronger and the molecule behaves as a 2D rotor. At 30 K the weakly adsorbed species desorb and the spectrum only presents peaks of the 2D rotor.

In 2007 Ramirez-Cuesta et al. used INS to study the adsorption of dihydrogen on a copper substituted ZSM5 zeolite. In the adsorption sites H_2 molecules appear to be bound to behave as 1D rotor, when their axis is parallel to the electric field, or in a plane perpendicular to the electric field as a 2D rotor. This paper shows how INS is a particularly useful tool to investigate the interaction between H_2 molecules and their binding sites: this technique allows us to measure the rotational constant, as well as observe the conversion of para-hydrogen into ortho-hydrogen.

In more complex materials as MOFs, various adsorption sites that display different properties may complicate the interpretation of INS spectrums, it is possible to chose the hydrogen loading so that only the main adsorption site is observed [42] [43].

Chapter 2

Introduction to inelastic[1] neutron transmission and imaging

Neutron imaging is a versatile and non-destructive technique that has proven to be very useful to investigate materials, for a vast range of applications. The good properties of neutrons make it possible to perform high resolution radiography and tomography on engineering-sized samples, at controlled environmental conditions. Although fairly expensive, neutrons have a very important role as complementary probes to X-rays. Especially in the last decades, neutron imaging evolved from a strict adsorption based contrast, to many different contrast based techniques (phase contrast, Bragg edge imaging, resonance adsorption imaging and so on) that are being used and developed to this day. In this chapter we will briefly discuss the main properties of neutrons, trying to underline what makes them interesting for materials investigations. Additionally we will illustrate the Beer-Lambert law and the mechanism behind neutron transmission, physical phenomenon that is essential for understanding the functioning of neutron transmission and neutron imaging instruments. We will then focus on neutron production, large scale facilities and the properties of two specific transmission-based instruments: IMAT and VESUVIO.

[1]For *inelastic* neutron transmission we refer to the measurements of those neutrons that do not undergo an inelastic scattering process.

2.1 Neutron as a probe

When the first nuclear reactors were developed in the 1940s, researchers soon realized that the neutrons produced in the reactions could serve as a probe to investigate condensed matter. Neutrons are subatomic particles, with neutral charge and half integer spin. Their mass is slightly grater than the mass of a proton and they have an intrinsic magnetic dipole moment. Neutrons are stable when they are part of an atomic nucleus, but become unstable when they are free: a neutron decays into a proton, an electron, and an antineutrino, with mean lifetime of approximately 14 minutes.

Table 2.1: Main properties of neutrons [44].

Physical quantity	Value
Mass	1.0087 a.m.u.
Charge	0
Spin	1/2
Magnetic moment	-1.913 μ_N
Mean lifetime	(879.4 $\pm$ 0.6)s

Neutrons can be classified according to their kinetic energies, as shown in table 2.2. Fission processes, as well as spallation processes, produce very energetic neutrons, known as fast neutrons, that are mainly used to simulate the effect of cosmic rays on electronic devices. Thermal neutrons on the other hand are much more useful to investigate vibrational or rotational properties matter. Thermal neutrons can be obtained from fast neutrons through a process called moderation, which consists in slowing them down. As an example, it is interesting to notice that para-hydrogen, among other materials, can be used as a neutron moderator.

Neutrons represent an ideal probe to study properties of matter for multiple reasons. For starters, their charge is neutral, which means they do not interact with the electric shells, but only with the atomic nuclei. The distances between nuclei are typically a factor 10^5 larger than the size of the nucleus itself, and since the nuclear forces are very short range, neutrons can travel long distances into materials without being scattered or adsorbed. This means that they are particularly indicated to investigate bulk properties, as opposed to protons or electrons, which cannot penetrate as deep. Moreover, when the neutrons have an energy comparable to that of the lattice vibrations at room temperature (around 25 meV), their wavelength happens to be comparable to the inter-atomic spacing of condensed matter. This makes them particularly ideal to investigate the structure

of solids. Neutrons are also useful to study magnetic properties of matter, since they have a half integer spin, but null charge. Furthermore, they are usually sensible to different isotopes, which means they can be used to study a contrast variation in the composition of a mixture of different isotopes [44].

Table 2.2: Neutron classification based on their energies.

Classification	Energy
Cold	$<$ 20 meV
Thermal	20-500 meV
Epithermal	500 meV - 10 keV
Fast	$<$ 10 keV - 10 MeV

In order to use neutrons as probes, it is essential to understand and model their interaction with matter. Neutrons can interact with a certain substance in a multitude of ways, depending both on the properties of the target and on the characteristics of the neutron beam. Each interaction phenomena can be described by a quantity known as cross section σ, which quantifies the probability that a specific process will take place. This quantity is expressed in unit of area (barns), and even though it is not strictly related to the dimension of the target atoms, it can be thought of as an effective area that the neutron must cross in order for the process to occur. In imaging experiments, it is particularly useful to define the scattering cross section of the process: an in-depth mathematical derivation of the scattering cross section is given in chapter 3, here the general discussion is accompanied by that of a more specific case, interesting for this study.

2.2 Neutron transmission: Beer-Lambert law

The Beer-Lambert law relates the attenuation of radiation travelling through a sample, to the properties of the material itself. To derive this formula lets consider a monochromatic neutron beam with intensity I_0. The beam is composed of neutrons travelling parallel to each other, impinging on a sample of thickness x.

One can divide the sample into thin slices along the x-axis, as shown in figure 2.1. The intensity of the beam that passed through one slice can be expressed as:

$$I_0 + dI \tag{2.1}$$

We can express the differential dI as:

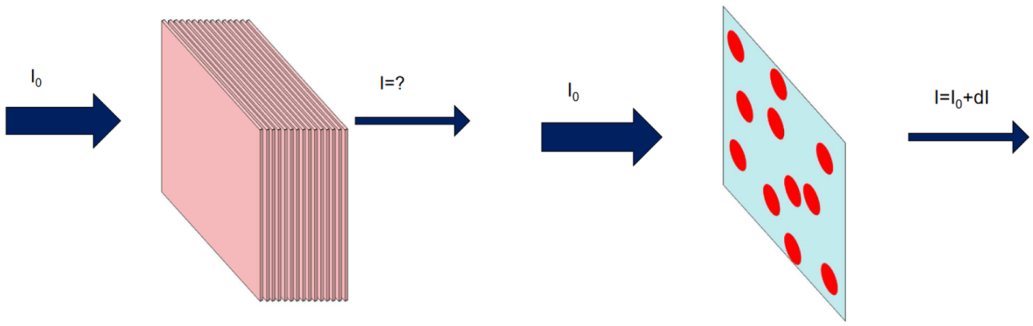

Figure 2.1: Representation of a sample irradiated by a neutron beam.

$$dI = -I_0 \cdot n(x) \cdot \sigma(x) dx \tag{2.2}$$

Where n is the number of adsorbers per unit volume, that is the concentration of the material, σ is the microscopic cross section and dx is the thickness of the slice. The negative sign expresses the fact that some of the neutrons are either adsorbed or scattered, and the intensity of the outgoing beam is reduced. We can now solve the equation integrating over the whole material, with thickness t:

$$\int_{I_0}^{I} \frac{dI}{I_0} = -\int_0^t n \cdot \sigma \cdot dx \tag{2.3}$$

Assuming that the concentration of the adsorber and its microscopic cross section don't depend on the position along the x-axis, this integral gives:

$$I = I_0 e^{-n\sigma t} \tag{2.4}$$

We can now assume that the material is composed of multiple chemical species, with different concentrations and microscopic cross sections: In this case the intensity of the outgoing neutron beam can be expressed as:

$$I = I_0 e^{-\sum_i n_i \sigma_i t} \tag{2.5}$$

From this relation we can define transmission as the ratio between outgoing intensity I and initial intensity I_0, which gives the Beer-Lambert law:

$$T = \frac{I}{I_0} = e^{-\sum_i n_i \sigma_i t} \tag{2.6}$$

2.3 Neutron sources and facilities: ISIS

It is possible to identify many different reactions and methods to produce neutrons, which vary from one another for characteristics like neutron energy, rate of the reaction, as well as cost and size of the source. In the field of neutron scattering, most research infrastructure rely on spallation or fission reactions to produce neutrons.

Fission sources: In the case of fission sources, two or three neutrons are produced when a thermal neutron is absorbed by a fissile material. The neutrons produced can induce a chain reaction by impacting on another fissile atom. All the neutrons that do not participate in the chain reaction can be channelled in a continuous beam that can be used to investigate matter. Some examples of facilities that rely on fission reactions are the NIST [45] reactor (Gaithersburg, USA), the HFIR [46] reactor (Oak Ridge Laboratory, USA), and the Institute Laue-Langevin (ILL) [47] in (Grenoble, France). Because of safety measures, reactor sources have a power limit, which results in a limit on the neutron flux.

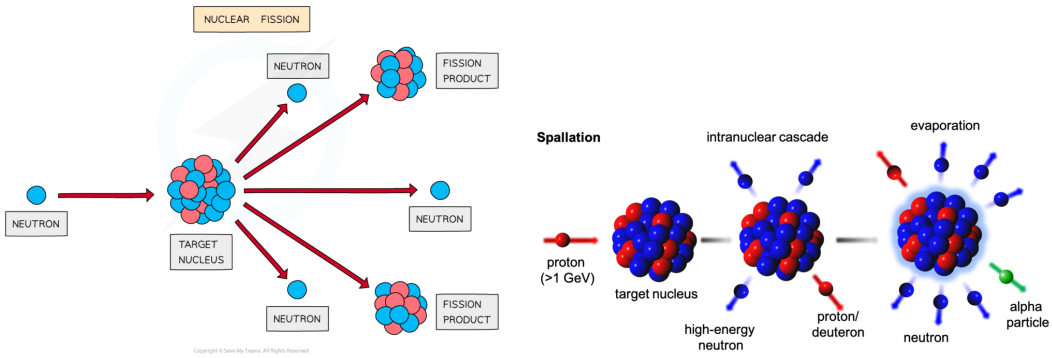

Figure 2.2: Representation of the fission chain reaction(a) and spallation reaction (b) for neutron production.

Spallation sources: Accelerator based neutron sources, on the other hand, can produce the most intense pulsed neutron beams. The main spallation sources are the Los Alamos Neutron Science Center [48] (Los Alamos National Laboratory, USA), the ISIS [49] facility (Rutherford-Appleton Laboratory in Didcot, UK) and the European Spallation Source [50] (Copenaghen, Denmark), which is still under

construction. Since the knowledge of the neutron source is necessary to correctly interpret data, for the purpose of this work we will focus on the functioning of the spallation source where data was collected: the ISIS neutron and muon source.

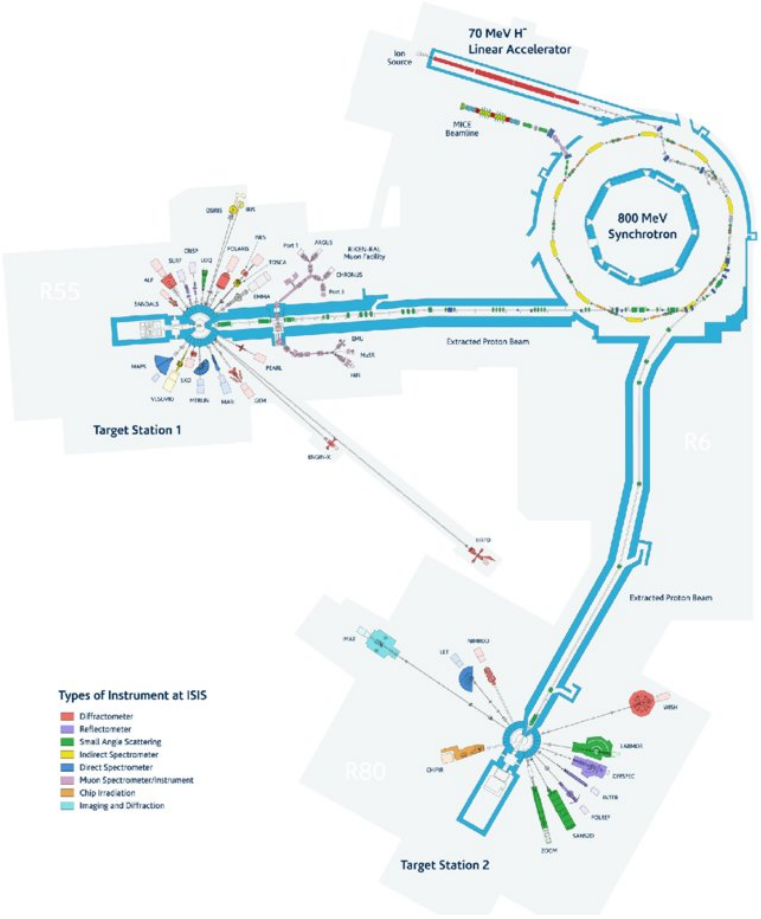

Figure 2.3: Representation of the layout of the ISIS facility.

Here, negatively charged hydrogen atoms are produced by an ion source and injected into a particle accelerator (LINAC), that accelerates them up to tens of MeV. The hydrogen atoms are then stripped of electrons and packed into bunches inside a synchrotron, which further accelerates them. The proton bunches come out of the synchrotron with energies up to 800 MeV and bunch rate of 50 Hz. The 160 kW proton beam collides on a tungsten target, causing the neutrons in the material to spall off. Tungsten is particularly indicated as a spallation target because it has a high atomic mass, which results in a high number of neutrons produced per proton. Moreover it has a high melting point, high thermal conductivity, and

it is safe and largely available. Neutrons are then expelled in every direction, they enter a complex system of reflectors and moderators, and they are later channeled through guides that lead them to many different instrument, each one optimized to investigate different characteristics of matter. Since the proton source is pulsed, neutrons come out in bunches that are particularly indicated for time-of-flight experiments, which allow to measure energy and wavevector transfer. ISIS instruments are divided into two target stations, the first one, TS-1, utilizes the protons at 40 Hz, while TS-2 has two 10 Hz pulsed magnets and a septum magnet that extract a proton beam with a bunch rate of 10 Hz. In the next sections we will discuss two particular instruments, that were used in this work to investigate the properties of molecular hydrogen adsorbed by HKUST-1: IMAT and VESUVIO.

2.4 Imaging beamline: IMAT

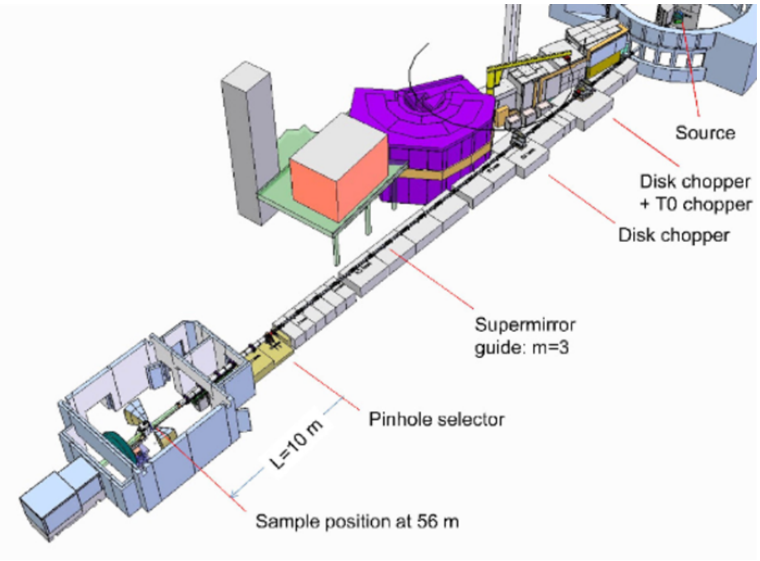

Figure 2.4: Layout of the main IMAT components.

IMAT is a neutron imaging and diffraction instrument, used to investigate the properties of matter in a broad range of material sciences. IMAT allows to perform neutron radiography, neutron tomography, and energy selective and dispersive neutron imaging, on engineering-sized samples (up to 1.5 tonnes). The instrument is located on the west 5 beam port of the second target station at ISIS. After fast neutrons are emitted by the source at the TS-2, they are thermalized

using moderators. Traveling through a supermirror guide, they pass into a pinhole, continuing inside flight tubes and finally arriving to the sample. Some of the neutrons will interact with the sample, others will be transmitted. IMAT is equipped with multiple kinds of detectors, which make it possible to perform different types of complementary analysis. Understanding their functioning is crucial to correctly interpreting the results, therefore we will now discuss the main properties of each constituent element.

2.4.1 Moderators

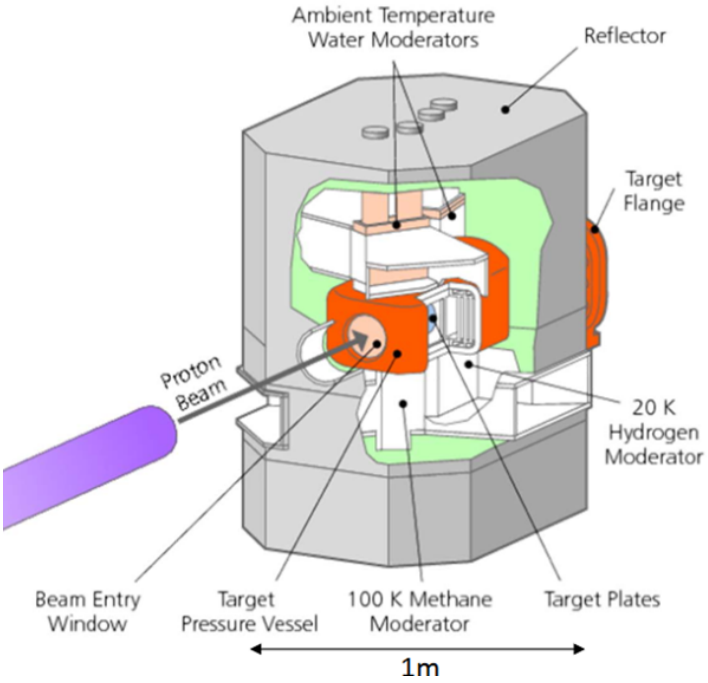

Figure 2.5: IMAT moderators layout.

Moderators are materials with a high neutron scattering cross section, low adsorption cross section and high neutron energy loss per collision. These properties allow the material to reduce the speed of fast neutrons generated during spallation processes without capturing them, thus thermalizing them to the temperature of the moderator. Moderating neutrons is essential to any scattering experiments as well as adsorption experiments, since thermal neutron interact more easily with nuclei, and are sensitive to the dynamics and structure of condensed matter. Because

of the conservation of energy and momentum, neutrons experience the highest energy transfer per collision when they interact with nuclei with similar mass, such as hydrogen nuclei, but it is also important to take into account the absorption cross section. Moreover, the type of the moderator and its thermodynamic conditions can be changed to select the energy range of the neutrons. For these reasons the most commonly used moderators are water and heavy water, particularly useful because they are easily found and can also be used as cooling medium in reactors, as well as graphite, that presents a particularly small adsorption cross section. On the other hand the beam port W5 where IMAT is installed utilizes both liquid hydrogen ($L{-}H_2$) and solid methane ($S{-}CH_4$) to reach a colder neutron energy spectrum, particularly useful in imaging and diffraction experiments. The moderator can be coated with reflecting or absorbing material, in these cases the moderator is said to be coupled and decoupled respectively. A decoupled moderator prevents the neutrons from bouncing on the walls of the moderator by absorbing them. The neutrons that are absorbed are the main contribution to the tail of the emission time distribution. A decoupled moderator therefore allows for a better time-of-flight resolution because it shortens the pulse length, but it also reduces the neutron flux. A similar result to decoupling can be obtained by poisoning the moderator, mixing it with an absorbing material, which results in an even shorter tail and lower flux. The moderator used for IMAT is a coupled moderator, because imaging applications require the highest possible neutron flux, then choppers are used to shorten the tail of the bunch.

2.4.2 Guiding system

Neutrons that emerge from the moderator are transported to the pinhole trough a supermirror guide. Neutron guides are long channels coated with reflective materials, that are supposed to redirect neutrons impacting with very small scattering angles. The reflective surface typically used for neutron guides is a polished multilayered device, known as supermirror. The functioning of the supermirror is based on Bragg diffraction by multilayers. They are made of alternating substrates of a high refractive index material, such as nickel, and a low refractive index material, like titanium, deposited on glass. Each bilayer has a different thickness, the neutrons are reflected by the bilayer that satisfies the Bragg condition, as shown in figure 2.6.

This allows to obtain a good reflectivity over a wide range of wavelengths. The materials chosen for the supermirror should also be nearly non-magnetic so as not

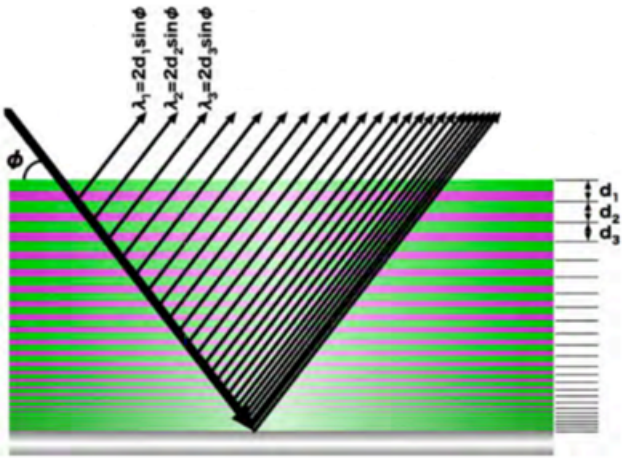

Figure 2.6: Schematization of the supermirror layers.

to disturb the neutron polarization. To reduce scattering, and the deposition of impurities on the substrate, the whole neutron guide is in a vacuum. At IMAT the supermirror guides have a square section, with dimensions 10×10 cm^2, and they are 44 m long. Different guide sections are placed inside a continuous vacuum system.

2.4.3 Energy selectors: choppers

IMAT uses choppers to select the energy of the incident neutron beam. Choppers are disks made of materials with high neutron adsorption cross section.

They are provided with an opening slit, so that when the beam is aligned with the slit the neutrons are able to pass through. Choppers rotate around their axis with a certain angular velocity and chop the neutron beam. Using the time-of-flight technique it is possible to use choppers to select a certain range of energies: Neutrons that are emitted at the same time by the pulsed source, impinge on the chopper at different times, depending on their energy. Choosing the rotational frequency of the chopper we can select the neutrons that are able to pass, while the others are adsorbed by the chopper. It is important to take into account that a smaller energy range entails lower neutron flux. IMAT uses choppers with a 1 m radius, the first one is a T0 chopper, that has the purpose of removing fast neutrons and gamma radiation, the other two are double-disk choppers, which use two different disks rotating in opposite directions, that ensures a better resolution.

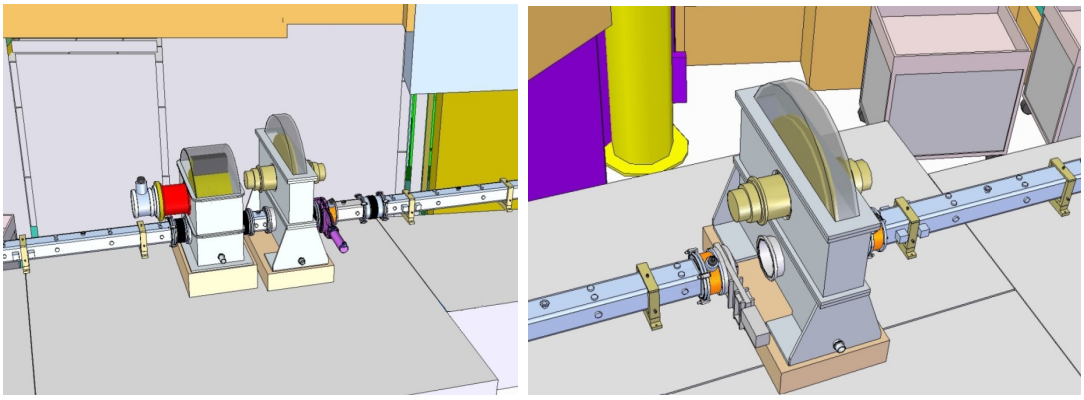

Figure 2.7: Schematization of the double disk choppers 1 (a) and 2 (b), respectively located at 12.2 m and 20.4 m from the moderator system.

2.4.4 Pinhole

The pinhole is the aperture that selects the beam size, and it is positioned at a distance of 10 m from the sample. The aperture selector allows to choose between five different apertures, their diameters are respectively 5, 10, 20, 40, 80 mm. This is useful to select a different ratio between distance from the sample and aperture diameter (L/D), which affects resolution. In fact, the spatial resolution can be quantified by the image blurring d defined by:

$$d = lD/L \tag{2.7}$$

Where D is the diameter of the pinhole, L the distance between pinhole and sample and l is the distance between sample and detector. The latter can not be as small as desired because the detector is located outside of the closed-circuit refrigerator, that has a certain dimension. The maximum field of view (FOV) is 20×20 cm^2 which makes it ideal for imaging applications on macroscopic samples. The FOV was chosen taking into account the space available for operational movements of the sample and the position where the diffraction detectors will be located. The aperture selector can also be left open for diffraction experiments. In this case a set of five jaws and a set of slits, located closer to the sample, can be adjusted to obtain a minimum beam size of 1 mm.

2.4.5 Sample environment and sample container

The sample stage at IMAT is equipped to support many different types of samples. The heavy duty positioning system can hold up to 1.5 tonnes, and it is equipped with a rotating stage for tomography applications. Moreover, the equipment from the ISIS sample environment pool allows the user to study the sample in different environments and subject it to different types of strains. For the purpose of this work we will use a rectangular aluminium container with a 5 cm width and 6 cm height.

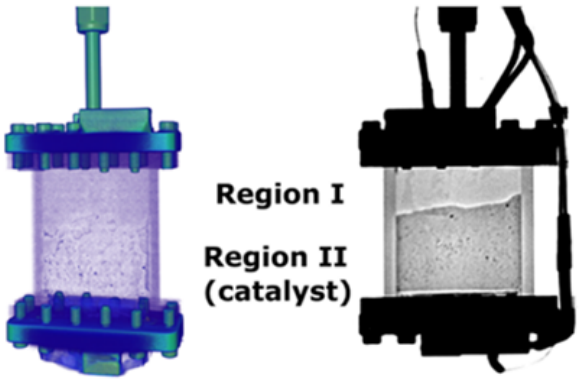

Figure 2.8: Neutron tomography (left) and radiography (right) of the sample container [38].

The aluminium was chosen because of its low neutron scattering and adsorption cross sections, which makes it practically transparent to neutrons. The container, shown in figure 2.8, was inserted in a closed-circuit refrigerator (CCR). A CCR is a device that generates low temperature by mechanically compressing and expanding an isolated gas. The CCR was inserted in a vacuum tank to allow cryogenic vacuum, and placed on the IMAT stage.

The container is connected at the top to a gas panel, which is located outside the IMAT blockhouse. The gas panel allows us to dose the gas that we want to study, in order to select its concentration in the sample. The gas is initially in a bottle, with a 10 bar pressure. The panel is equipped with four buffers of 1 L volume (fig. 2.9). The buffers can be filled with the gas at a desired pressure. Knowing the temperature of the buffers (300 K), it is possible to choose the pressure in order to select the desired number of moles for the gas. Buffers are equipped with valves that can be opened slowly to pour the gas into the sample container. The CCR

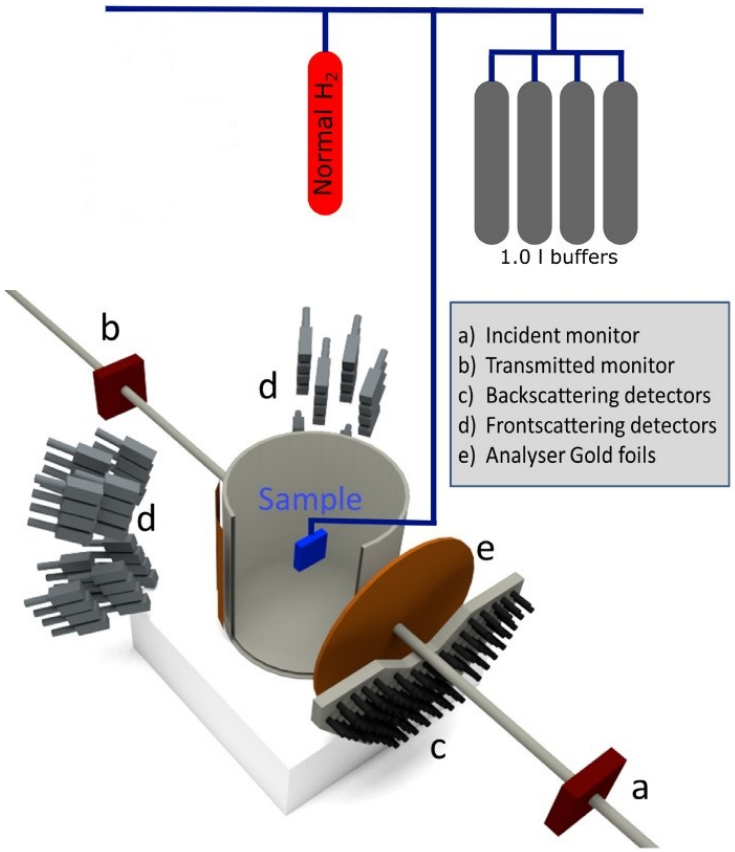

Figure 2.9: Schematic representation of the equipment layout.

ensure that the sample container is at a lower temperature than the buffers, which means that the gas will spontaneously stream into the container and condensate.

2.4.6 Detectors

IMAT is equipped with different imaging detectors, as well as beam monitors for diagnostics and normalizations. A detector based on microchannel plates (MCP) is used for energy resolved neutron imaging, but was not available for this experiment. This type of detector measures the energy of the neutron with the time-of-flight technique, as well as the position where the neutron impacts and has a field of view (FOV) of 28×28 mm^2 . In our experiment we used a CCD system. This camera, with FOV 20×20 cm^2, can be used for white beam radiography and tomography, as well as energy selective neutron imaging. It is particularly useful for contrast

enhancement or contrast variations experiments. Moreover a glass scintillator monitor (GS20) can be used to measure the flux of the incident neutron beam. For the purposes of this work we will focus on the functioning of the CCD system, which will be used to perform time resolved energy selective neutron imaging. The CCD-based system is housed in a light-tight camera box, which can be moved to vary its distance from the sample. Various scintillator screens can be accommodated on the front of the camera box, they vary for dimensions and materials and need to be chosen depending on the application. The photons emitted by the scintillator are reflected at 90° by a mirror, towards the CCD camera. The camera has 2048 x 2048 pixels and is kept at a temperature of 203 K to minimize the signal to noise ratio due to the shot noise.

2.5 Imaging experiment for the catalysed hydrogen conversion

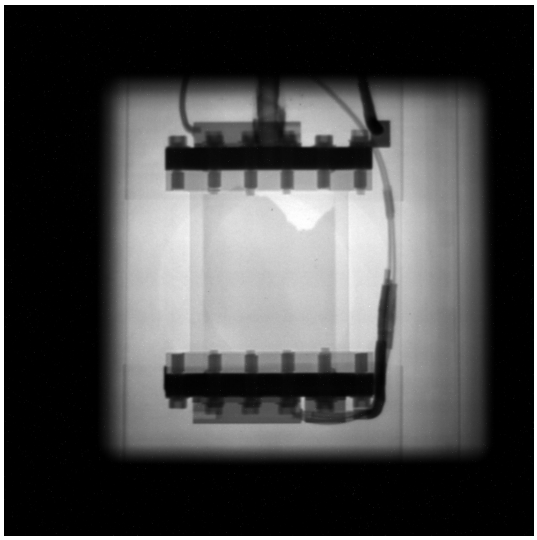

Figure 2.10: Example of a radiograph of the sample container, loaded with HKUST-1 and hydrogen. This image has been processed, increasing contrast and brightness, for better visualization.

The last chapter of this work presents an experimental study performed at the IMAT beamline of the ISIS neutron and muon source. The purpose of this study was to investigate the catalysed ortho-para conversion of hydrogen adsorbed by

HKUST-1. Here energy selective neutron imaging was used to characterize the conversion rate as a function of time, by acquiring radiographs of the sample at regular time intervals. Figure 2.10 shows one of the radiographs obtained by irradiating the sample container with the IMAT neutron beam for 30 s. Acquiring many similar radiographs allowed us to observe the time dependence of the process. This technique is known as time-resolved neutron imaging, it relies on the great difference between the ortho and para hydrogen scattering cross sections to measure the variation of contrast as a function of time. Moreover imaging techniques allow us to explore the spatial distribution of the sample, rendering them particularly appealing for industrial and engineering applications.

2.6 Neutron transmission beamline: VESUVIO

The VESUVIO spectrometer operates at the first target station of the ISIS neutron and muon source. This spectrometer performs transmission measurements, as well as inelastic neutron scattering at high energy ($\hbar\omega \geq 1$ eV) and high momentum transfer (q ≥ 20 Å^{-1}), technique known as deep inelastic neutron scattering (DINS). VESUVIO faces a water moderator, that operates at 295 K. The resulting neutron beam is polychromatic: it presents a broad peak around 0.03 eV, and a tail in the epithermal region, up to 10^7 eV. Unlike IMAT, VESUVIO is not equipped with choppers, therefore the sample is irradiated with the whole polychromatic beam. In order to measure the energy of the incoming neutrons this instrument makes use of the time-of-flight (ToF) technique. This technique consists of calculating the neutron energy by measuring the time it takes for it to travel from the moderator to the detector. If the lengths of the flight paths from moderator to sample (L_0) and from sample to detector (L_1) are known, the time of flight can be written as:

$$ToF = \frac{L_0}{v_0} + \frac{L_1}{v_1} = \sqrt{\frac{m}{2}}\left(\frac{L_0}{\sqrt{E_i}} + \frac{L_1}{\sqrt{E_f}}\right) \tag{2.8}$$

where v_0 and v_1 are the neutron velocities of that incident neutrons, and neutrons that come out of the sample respectively. These velocities are written in terms of neutron energies in the right hand side.

In the case of **DINS experiments**, this instrument operates in inverse geometry mode, which means that the measured neutron final energy is fixed, while the incident neutron energy can be evaluated using the ToF technique. Here, the

final energy of neutrons is selected using a foil of a material that presents a single nuclear resonance in the considered energy range, usually gold. During data acquisition this foil is placed between sample and detector. Later the same measurements are acquired without the foil. The difference between these two data sets gives the number of neutrons absorbed by the foil, which provides a measure of how many neutrons scattered from the sample, at that specific angle, have a final energy that corresponds to the gold resonance energy. The foil cycling technique is used at multiple scattering angles, which allows the user to measure the wave vector. Since the final energy is fixed, we are able to calculate the initial energy with the ToF technique.

On the other hand for **transmission measurements** the energy of the neutron can be calculated considering that the energy of transmitted neutrons does not change. This means that we can consider $v_1 = v_0$ and therefore calculate the energy of neutrons taking into account that their flight path now has a length equal to $L_1 + L_0$. To do so the neutron detector needs to measure the flux of incoming neutrons, as well as the time at which they arrive on the detector. VESUVIO transmission detector is a glass scintillator, in particular a GS20. For neutron applications, the glass of these type of detectors is usually enriched with lithium-6, the GS20 has a 95% enrichment, which corresponds to a Li-6 content of 7.33% by weight. Lithium-6 is particularly interesting for this application because it has a neutron absorption cross section of 930 barn at thermal wavelengths. This detector, although not particularly efficient, presents a good stability compared to other solutions. However it is important to take into account that it is also sensible to γ-ray, which means that measurements will be subject to a background noise.

The sample container and environment at the VESUVIO beamline are identical to what we described for IMAT. Here the sample container is again placed inside a CCR and loaded with hydrogen using bottles and buffers, as shown in figure 2.9 [51].

Chapter 3

Neutron scattering cross section for diatomic molecules

As mentioned before, neutrons interact only weakly with matter, into which they can penetrate deeply. When a neutron interacts with a nucleus, it can be either scattered or adsorbed. Adsorption reactions include neutron capture reactions as well as fission reactions, and are extremely important for a vast number of applications. For the purpose of this work however, we are mainly interested in scattering phenomena. In fact, modeling the scattering process we are able to investigate structural properties of matter by detecting scattered or transmitted neutrons. In this chapter we will discuss the theory behind scattering reactions, finally defining an important quantity known as scattering cross section. The cross section will be calculated for a generic sample, and later for diatomic molecules.

3.1 Scattering cross section

To investigate matter using neutrons, we firstly need to understand how a thermal neutron beam interacts with a certain substance. When a neutron with the wave vector $\boldsymbol{k}$ impacts on a target, it is scattered into a different state, with wave vector $\boldsymbol{k'}$. The properties of the outgoing neutron can be investigated in various ways, but the measurements always depend on a basic quantity called double differential cross section. The double differential cross section gives information on the fraction of total neutrons that is scattered into a small solid angle $d\Omega$, with a final energy between E' and $E' + dE'$. Therefore it is proportional to the probability of a neutron to be scattered in a certain direction with a certain energy. It is usually

denoted by the expression:

$$\frac{d^2\sigma}{d\Omega dE'} \tag{3.1}$$

This quantity has the dimension of an area, and is usually expressed in barn (1 barn = 10^{-24} cm^2). Integrating the differential cross section over energy and solid angle, we obtain a total scattering cross section, which is defined by the ratio between the number of neutron scattered on the whole solid angle, and the flux of incident neutrons.

The cross section depends on both the properties of the probe and the target, in particular it is possible to identify a relevant dependence on the isotope. Table 3.1 reports as an example the value of coherent, incoherent scattering cross sections, as well as total scattering cross section and absorption cross section for neutrons impinging on different hydrogen and carbon isotopes. This allows us to observe contrast variations from one isotope to another, which makes them easily distinguishable.

Table 3.1: Values of coherent cross sections, incoherent cross sections, total scattering cross section and absorption cross section for different isotopes expressed in barn.

Isotope	Coh xs	Inc xs	Scatt xs	Abs xs
H	1.7568	80.26	82.02	0.3326
1H	1.7583	80.27	82.03	0.3326
2H	5.592	2.05	7.64	0.000519
3H	2.89	0.14	3.03	0
C	5.551	0.001	5.551	0.0035
12C	5.559	0	5.559	0.00353
13C	4.81	0.034	4.84	0.00137
Al	1.495	0.0082	1.503	0.231

To be able to correctly understand the experimental results, it is important to derive a theoretical expressions for the cross section of the specific target. In the next sections we will derive an equation for the differential scattering cross section, underlying the distinction between incoherent and coherent scattering, and we will then specialize the formula to the case of diatomic molecules. For now, we will start considering the simplest case: a single fixed nucleus, that interacts with one neutron of wave vector $\boldsymbol{k}$. If the z axis is along the direction of $\boldsymbol{k}$ the initial wave function of the neutron can be expressed as:

$$\Psi_{inc} = e^{i\boldsymbol{kz}} \tag{3.2}$$

Since the nuclear forces have a range of around 10^{-14} and the wavelength of a thermal neutron is around 10^{-10} the process depends mainly on the S waves, which have spherical symmetry. As a consequence, the wave function of the scattered neutron can be written as a spherical wave:

$$\Psi_{sc} = -\frac{b}{r} e^{i\boldsymbol{kr}} \tag{3.3}$$

Where b is known as the scattering length, and it depends on the particular nucleus and its spin, compared to that of the neutron. In fact, if the nucleus has spin I, the total spin of the system neutron-nucleus can be of $I + \frac{1}{2}$ or $I - \frac{1}{2}$, to each state corresponds a different value of b, that can be measured experimentally.

In the simple case of one neutron scattering on a single nucleus, the differential cross section can be evaluated in terms of the scattering angle by considering the number of neutron passing through an area dS in the unit of time, which is given by:

$$v dS |\Psi_{sc}|^2 = v dS \frac{b^2}{r^2} = v b^2 d\Omega \tag{3.4}$$

Where v is the velocity of the neutron, before and after the scattering process. The flux of incident neutrons is given by:

$$\Phi = v |\Psi_{inc}|^2 = v \tag{3.5}$$

Applying the definition of the differential cross section, which tell us that $\frac{d\sigma}{d\Omega}$ is equal to the number of neutron scattered into $d\Omega$ in the unit of time, divided by the flux of incident neutrons $\Phi(E)$, it is possible to evaluate the differential cross section in terms of the scattering angle:

$$\frac{d\sigma}{d\Omega} = \frac{v b^2 d\Omega}{\Phi d\Omega} = b^2 \tag{3.6}$$

Integrating over the whole solid angle this gives a total cross section of:

$$\sigma_{tot} = 4\pi b^2 \tag{3.7}$$

This suggests that in this simple case the neutron sees the atom as a sphere of radius b, thus σ_{tot} is an effective area that quantifies the probability of the scattering event.

While this simple model gives an interesting interpretation of the scattering length, a more complete theory requires us to consider a system with many nuclei. Given a system with N nuclei, we indicate with $\boldsymbol{R_j}$ the position vector of the j-th nucleus, and $\boldsymbol{r}$ that of the neutron. As the neutron is scattered, and its wave vector changes from $\boldsymbol{k}$ to $\boldsymbol{k'}$, the scattering system changes state, from an initial state λ to the final state λ'. In this case the differential scattering cross section needs to take into account all the possible processes during which the system state changes from λ to λ' and the neutron state changes from $\boldsymbol{k}$ to $\boldsymbol{k'}$.

The double differential scattering cross section $\frac{d^2\sigma}{d\Omega dE'}$ can be defined as the number of neutron with energies between E' and $E' + dE'$ scattered into $d\Omega$ in the unit of time, divided by the flux of incident neutrons $\Phi(E)$:

$$\frac{d^2\sigma}{d\Omega dE'} = \frac{\text{neutrons scattered per second}}{\Phi(E) d\Omega dE'} \tag{3.8}$$

To quantify the number of neutron scattered per second in $d\Omega$ we can use the Fermi golden rule, which states that the rate of transitions from the state $\boldsymbol{k}, \lambda$ to $\boldsymbol{k'}, \lambda'$ is given by:

$$W_{\boldsymbol{k},\lambda \to \boldsymbol{k'}\lambda'} = \frac{2\pi}{\hbar} \rho_{\boldsymbol{k'}} |\, \langle \boldsymbol{k'}\lambda' | V | \boldsymbol{k}\lambda \rangle \,|^2 \tag{3.9}$$

Where $\rho_{\boldsymbol{k'}}$ is the number of momentum states per unit energy in $d\Omega$. To write $\frac{d^2\sigma}{d\Omega dE'}$ it is important to consider all the possible $\boldsymbol{k'}$ that end up in the solid angle $d\Omega$, however, the derivation of the golden rule shows that the probability of the transition is negligible for all the $\boldsymbol{k'}$ that don't correspond to the conservation of energy, which states that:

$$E + E_\lambda = E' + E_{\lambda'} \tag{3.10}$$

Where the left hand side of the equation shows the energies of neutron and scattering system before the scattering, and the the right hand side after the scattering. As a consequence, the energy distribution of the scattered neutron can be written as a δ-function, and the differential scattering cross section can be expressed in terms of the energy as:

$$\left(\frac{d^2\sigma}{d\Omega dE'} \right)_{\lambda \to \lambda'} = \frac{1}{\Phi d\Omega dE'} \frac{2\pi}{\hbar} \rho_{\boldsymbol{k'}} |\, \langle \boldsymbol{k'}\lambda' | V | \boldsymbol{k}\lambda \rangle \,|^2 \delta(E_\lambda - E_{\lambda'} + E - E') \tag{3.11}$$

We can now explicate the flux ϕ and density $\rho_{\boldsymbol{k'}}$. The flux of incident neutrons

is given by their velocity of particles in a volume Δ as:

$$\Phi = \frac{1}{\Delta}\frac{\hbar k}{m} \tag{3.12}$$

The density of final scattering states per unit of energy is given by:

$$\rho_{\boldsymbol{k'}}(E) = \frac{\Delta}{(2\pi)^3}\frac{d\boldsymbol{k'}}{dE} \tag{3.13}$$

Since:

$$d\boldsymbol{k'} = k'^2 d\Omega dk' = k^2 d\Omega dk \tag{3.14}$$

and:

$$dE = \frac{\hbar^2 k}{m} dk \tag{3.15}$$

we can write $\rho_{\boldsymbol{k'}}$ as:

$$\rho_{\boldsymbol{k'}} = \frac{\Delta}{(2\pi)^3}\frac{mk}{\hbar^2} d\Omega \tag{3.16}$$

Substituting 3.12 and 3.16 into 3.11 we obtain:

$$\left(\frac{d^2\sigma}{d\Omega dE'}\right)_{\lambda\to\lambda'} = \frac{k'}{k}\left(\frac{m}{2\pi\hbar^2}\right) |\, \langle \boldsymbol{k'}\lambda'|V|\boldsymbol{k}\lambda\rangle \,|^2 \delta(E_\lambda - E'_{\lambda'} + E - E') \tag{3.17}$$

Where we notice that the normalization volume Δ correctly canceled out since it is arbitrary.

The differential scattering cross section can be further evaluated by calculating the matrix element. For this purpose we need to define the potential V that the neutron feels when approaching the scattering system. Since the potential has to depend on the distance between the neutron and each nucleus, we can write it as:

$$V = \sum_j V_j(\boldsymbol{r} - \boldsymbol{R_j}) = \sum_j V_j(\boldsymbol{x_j}) \tag{3.18}$$

Where V_j is the potential due to the j-th nucleus. We substitute this into the matrix element:

$$\langle \boldsymbol{k'}\lambda'|V|\boldsymbol{k}\lambda\rangle = \sum_j \int \chi^*_{\lambda'} e^{-i\boldsymbol{k'}\cdot\boldsymbol{r}} V_j(\boldsymbol{r} - \boldsymbol{R_j}) \chi_\lambda e^{i\boldsymbol{k}\cdot\boldsymbol{r}} d\boldsymbol{R} d\boldsymbol{r} \tag{3.19}$$

Where we called χ_λ and $\chi_{\lambda'}$ the wave function of the scattering system before and

after the scattering event.Writing the neutron wavefunction we assumed that in the initial and final states, where the neutron is far from the sample, it can be described as a plane wave. Substituting $\boldsymbol{r} = \boldsymbol{x_j} + \boldsymbol{R_j}$:

$$= \sum_j \int \chi^*_{\lambda'} e^{-i\boldsymbol{k'}\cdot(\boldsymbol{x_j}+\boldsymbol{R_j})} V_j(\boldsymbol{x_j}) \chi_\lambda e^{i\boldsymbol{k}\cdot(\boldsymbol{x_j}+\boldsymbol{R_j})} d\boldsymbol{R} d\boldsymbol{r} = \sum_j V_j(\boldsymbol{q}) \langle \lambda' | e^{i\boldsymbol{q}\boldsymbol{R_j}} | \lambda \rangle \quad (3.20)$$

Where $\boldsymbol{q}$ is the scattering vector $(\boldsymbol{k} - \boldsymbol{k'})$ and $V_j(\boldsymbol{q})$ is the Fourier transform of $V_j(\boldsymbol{x_j})$.

To further evaluate the expression we need to substitute a specific function for $V_j(\boldsymbol{x_j})$, a good approximation to the real potential is given by the Fermi Pseudo-potential. The main idea behind this pseudo-potential is that, since V depends on nuclear forces, and is therefore really short range compared to the wavelength of the neutron, we can assume it is of the form:

$$V(\boldsymbol{x}) = a\delta(\boldsymbol{x}) \quad (3.21)$$

Where $\delta(\boldsymbol{x})$ is the three dimensional Dirac delta function. We can derive the constant a by considering once again the case of one neutron scattering on a fixed nucleus, specifically we want to rewrite the expression for $\frac{d\sigma}{d\Omega}$ found in 3.6, using this new formalism. If the nucleus is only one we have $j = 1$ and no sum over j. Moreover we can assume the nucleus is in the origin, so $\boldsymbol{R} = 0$, and since the nucleus is fixed $\lambda = \lambda'$. Using this formalism 3.19 becomes:

$$\langle \boldsymbol{k'}\lambda' | V | \boldsymbol{k}\lambda \rangle = \int \chi^*_\lambda \chi_\lambda d\boldsymbol{R} \int V(\boldsymbol{r}) e^{i\boldsymbol{q}\cdot\boldsymbol{r}} d\boldsymbol{r} = \int V(\boldsymbol{r}) e^{i\boldsymbol{q}\cdot\boldsymbol{r}} d\boldsymbol{r} \quad (3.22)$$

Where we used that χ_λ is normalised. We can now substitute the matrix element into the formula for the differential cross section.

$$\frac{d\sigma}{d\Omega} = \left(\frac{m}{2\pi\hbar^2}\right)^2 \left| \int V(\boldsymbol{r}) e^{i\boldsymbol{q}\cdot\boldsymbol{r}} d\boldsymbol{r} \right|^2 \quad (3.23)$$

Where we also used that $k' = k$. Now we can substitute $V(\boldsymbol{r}) = a\delta(\boldsymbol{r})$:

$$\frac{d\sigma}{d\Omega} = \left(\frac{m}{2\pi\hbar^2}\right)^2 \left| \int a\delta(\boldsymbol{r}) e^{i\boldsymbol{q}\cdot\boldsymbol{r}} d\boldsymbol{r} \right|^2 = \left(\frac{m}{2\pi\hbar^2}\right)^2 a^2 \quad (3.24)$$

Comparing this to 3.6 we notice that the constant a can be written in terms of the scattering length b as:

$$a = \frac{2\pi\hbar^2}{m} b \tag{3.25}$$

Therefore we find the Fermi pseudo-potential:

$$V(\boldsymbol{r}) = \frac{2\pi\hbar^2}{m} b\delta(\boldsymbol{r}) \tag{3.26}$$

We can now use this in the expression for the general scattering system, defining:

$$V_j(\boldsymbol{x_j}) = \frac{2\pi\hbar^2}{m} b_j\delta(\boldsymbol{x_j}) \tag{3.27}$$

That has the following Fourier transform:

$$V_j(\boldsymbol{q}) = \frac{2\pi\hbar^2}{m} b_j \tag{3.28}$$

Substituting the pseudopotential in the formula for $\left(\frac{d^2\sigma}{d\Omega dE}\right)_{\lambda\to\lambda}$, found in 3.17, we can now evaluate the matrix element by inserting 3.28 into 3.20:

$$\left(\frac{d^2\sigma}{d\Omega dE'}\right)_{\lambda\to\lambda'} = \frac{k'}{k}\left|\sum_j \langle\lambda'|b_j e^{i\boldsymbol{q}\cdot\boldsymbol{R_j}}|\lambda\rangle\right|^2 \delta(E_\lambda - E_{\lambda'} + E - E') \tag{3.29}$$

It is possible to rewrite this expression substituting the integral representation of the δ-function:

$$\delta(E_\lambda - E_{\lambda'} + E - E') = \frac{1}{2\pi\hbar}\int_{-\infty}^{\infty} e^{i(E_\lambda - E_{\lambda'})t/\hbar} e^{-i\omega t} dt \tag{3.30}$$

Where ω is defined by $\hbar\omega = E - E'$. We can write the differential scattering cross section of the process as:

$$\left(\frac{d^2\sigma}{d\Omega dE'}\right)_{\lambda\to\lambda'} = \frac{1}{2\pi\hbar}\frac{k'}{k}\langle\lambda|\sum_{j'} b_{j'} e^{-i\boldsymbol{q}\cdot\boldsymbol{R_{j'}}}|\lambda'\rangle\ \langle\lambda'|\sum_j b_j e^{i\boldsymbol{q}\cdot\boldsymbol{R_j}}|\lambda\rangle \int_{-\infty}^{\infty} e^{i(E_{\lambda'} - E_\lambda)t/\hbar} e^{-i\omega t} dt \tag{3.31}$$

This formula describes the differential cross section of a scattering process in which the system goes from a state λ to a state λ'. However, in actual experiment, it is not possible to measure this quantity, because the scattering system never goes exactly from one state to another. Instead we need to sum over all possible initial

states λ, weighted with the probability p_λ that the scattering system is in that state, and over all possible final states λ', so that:

$$\frac{d^2\sigma}{d\Omega dE'} = \sum_{\lambda\lambda'} p_\lambda \left(\frac{d^2\sigma}{d\Omega dE'}\right)_{\lambda\to\lambda'} \tag{3.32}$$

The probability p_λ is defined using the Boltzmann distribution as:

$$p_\lambda = \frac{1}{Z} e^{-E_\lambda \beta} \tag{3.33}$$

Where Z is the partition function defined as $Z = \sum_\lambda e^{-E_\lambda\beta}$ and $\beta = \frac{1}{k_B T}$.

$$\begin{aligned}\frac{d^2\sigma}{d\Omega dE'} =& \sum_{\lambda\lambda'} p_\lambda \frac{1}{2\pi\hbar}\frac{k'}{k} \langle\lambda|\sum_{j'} b_{j'} e^{-i\boldsymbol{q}\cdot\boldsymbol{R_{j'}}}|\lambda'\rangle \ \langle\lambda'|\sum_{j} b_j e^{i\boldsymbol{q}\cdot\boldsymbol{R_j}}|\lambda\rangle \times \\ &\times \int_{-\infty}^{\infty} e^{i(E_{\lambda'}-E_\lambda)t/\hbar} e^{-i\omega t} dt\end{aligned} \tag{3.34}$$

To further evaluate this formula we need to establish if there is any correlation between the values of the scattering length b of neighbouring atoms. In the case of diatomic molecules, there's a strong correlation between scattering lengths and atom dispositions, therefore we will dedicate an entire section to this particular case. Here we will briefly discuss how to treat the case where no correlation occurs, in order to better compare the two situations. If different isotopes are randomically mixed, there is no correlation between the values of b and atoms disposition, in this case the differential scattering cross section becomes:

$$\frac{d^2\sigma}{d\Omega dE'} = \frac{k'}{k}\frac{1}{2\pi\hbar} \sum_{jj'} \overline{b_{j'} b_j} \int_{-\infty}^{\infty} e^{-i\omega t} \sum_\lambda p_\lambda \langle\lambda| e^{-i\boldsymbol{q}\cdot\boldsymbol{R_{j'}}} e^{i\boldsymbol{q}\cdot\boldsymbol{R_j(t)}} |\lambda\rangle \, dt \tag{3.35}$$

Where the sum over λ' in 3.32 was evaluated using the closure relation as in:

$$\sum_{\lambda'} \langle\lambda|A|\lambda'\rangle \ \langle\lambda'|B|\lambda\rangle = \langle\lambda|AB|\lambda\rangle \tag{3.36}$$

and the matrix element was written in terms of the Heisenberg operator $\boldsymbol{R_j(t)}$ defined as:

$$\boldsymbol{R_j(t)} = e^{iHt/\hbar} \boldsymbol{R_j} e^{-iHt/\hbar} \tag{3.37}$$

We can write the thermal average with the symbol $[\cdot]_T$, obtaining:

$$\frac{d^2\sigma}{d\Omega dE'} = \frac{k'}{k}\frac{1}{2\pi\hbar}\sum_{jj'}\overline{b_{j'}b_j}\int_{-\infty}^{\infty} e^{-i\omega t}\left[\langle\lambda|e^{-i\boldsymbol{q}\cdot\boldsymbol{R_{j'}}}e^{i\boldsymbol{q}\cdot\boldsymbol{R_j(t)}}|\lambda\rangle\right]_T dt \tag{3.38}$$

In the next paragraphs we will discuss the simple case of system composed of one element, in order to discuss the difference between coherent and incoherent scattering. We will then focus on diatomic molecules, that are of particular interest for this study. Diatomic molecules represent an example of a system in which there's correlation between the value of the scattering lengths and atom disposition.

3.2 Coherent and incoherent scattering

In a generic system, even if it's composed of only one element, the scattering length b is never a constant. In fact it can vary from one isotope to another, and depending on the spins of the nucleus compared to that of the impacting neutron. Let us now consider the possible values that b assumes in a system consisting of one element, each b_i occurs with a frequency f_i, so that:

$$\sum_i f_i = 1 \quad \text{and} \quad \bar{b} = \sum_i f_i b_i \tag{3.39}$$

Where the frequency f_i does not depend on the value of b_i of neighbouring atoms. As shown before, the cross section that we measure can be written in terms of the $b_j b_{j'}$ averaged over random isotopes distribution and relative spin orientations, as:

$$\frac{d^2\sigma}{d\Omega dE'} = \frac{k'}{k}\frac{1}{2\pi\hbar}\sum_{jj'}\overline{b_{j'}b_j}\int_{-\infty}^{\infty} e^{-i\omega t}\left[\langle\lambda|e^{-i\boldsymbol{q}\cdot\boldsymbol{R_{j'}}}e^{i\boldsymbol{q}\cdot\boldsymbol{R_j(t)}}|\lambda\rangle\right]_T dt \tag{3.40}$$

where:

$$\overline{b_j b_{j'}} = \begin{cases} \overline{b_j}\ \overline{b_{j'}} = |\bar{b}|^2 & \text{if } \ j \neq j' \\ \overline{|b_j|^2} = \overline{|b|^2} & \text{if } \ j = j' \end{cases} \tag{3.41}$$

Writing equation 3.40 we are once again assuming that there is no correlation between the values of b of each atom, and the atom position, this allowed us to extract the average over the scattering lengths.

Substituting the two values for the average expressed in 3.41 into 3.40, the

cross section becomes the sum of two terms, that we can manipulate as follows:

$$\begin{aligned}\frac{d^2\sigma}{d\Omega dE'} &= \frac{k'}{k}\frac{1}{2\pi\hbar}(\bar{b})^2\sum_{j\neq j'}\int_{-\infty}^{\infty}e^{-i\omega t}\left[\langle\lambda|e^{-i\boldsymbol{q}\cdot\boldsymbol{R_{j'}}}e^{i\boldsymbol{q}\cdot\boldsymbol{R_j(t)}}|\lambda\rangle\right]_T dt+\\ &+\frac{k'}{k}\frac{1}{2\pi\hbar}\overline{b^2}\sum_{j}\int_{-\infty}^{\infty}e^{-i\omega t}\left[\langle\lambda|e^{-i\boldsymbol{q}\cdot\boldsymbol{R_{j'}}}e^{i\boldsymbol{q}\cdot\boldsymbol{R_j(t)}}|\lambda\rangle\right]_T dt=\\ &=\frac{k'}{k}\frac{1}{2\pi\hbar}(\bar{b})^2\sum_{jj'}\int_{-\infty}^{\infty}e^{-i\omega t}\left[\langle\lambda|e^{-i\boldsymbol{q}\cdot\boldsymbol{R_{j'}}}e^{i\boldsymbol{q}\cdot\boldsymbol{R_j(t)}}|\lambda\rangle\right]_T dt+\\ &+\frac{k'}{k}\frac{1}{2\pi\hbar}(\overline{b^2}-(\bar{b})^2)\sum_{j}\int_{-\infty}^{\infty}e^{-i\omega t}\left[\langle\lambda|e^{-i\boldsymbol{q}\cdot\boldsymbol{R_{j'}}}e^{i\boldsymbol{q}\cdot\boldsymbol{R_j(t)}}|\lambda\rangle\right]_T dt\end{aligned} \tag{3.42}$$

Now the two terms can be written respectively as:

$$\frac{d^2\sigma}{d\Omega dE'} = \left(\frac{d^2\sigma}{d\Omega dE'}\right)_{coh} + \left(\frac{d^2\sigma}{d\Omega dE'}\right)_{inc} \tag{3.43}$$

We can see from the equations that the coherent scattering depends on the position of two nuclei j and j' at different times, and is summed over all possible j and j'. The coherent scattering is the scattering that the system would produce if all scattering lengths were equal to $\bar{b}$. This term gives interference effects, based on the position of the nuclei. On the other hand the incoherent scattering terms depend only on the $j-th$ nucleus, therefore this term depends on the correlation between the same nucleus at different times, which does not give interference. The incoherent term is proportional to the deviations of all the scattering length from their mean value.

We can now discuss the values of the frequencies f_i for a specific case, that are useful to calculate $\bar{b}$ and $\overline{b^2}$. In the simplest case where we have one isotope with nuclear spin zero, all values of b are equal. If the system is composed of a single isotope with nuclear spin I, the spin of the nucleus-neutron system can be equal to $I+\frac{1}{2}$ or $I-\frac{1}{2}$, which identifies two possible scattering lengths, usually known as b^+ and b^- respectively. If the neutron beam is not polarised and the nuclear spins are randomly oriented each spin state has the same probability. The number of states with spin $I+\frac{1}{2}$ is $2(I+\frac{1}{2})-1=2I+2$, the number of states with spin $I-\frac{1}{2}$ is $2(I-\frac{1}{2})-1=2I$. From this follows that the scattering length b^+ occurs with frequency:

$$f^+ = \frac{2I+2}{4I+2} = \frac{I+1}{2I+1} \tag{3.44}$$

And similarly:

$$f^- = \frac{2I}{4I+2} = \frac{I}{2I+1} \tag{3.45}$$

Knowing this we can evaluate the mean value of b:

$$\overline{b} = \frac{1}{2I+1}[(I+1)b^+ + Ib^-] \tag{3.46}$$

If the scattering system is composed of different isotopes the mean value of b can be calculated by multiplying each frequency by the relative abundance of the isotope.

3.3 Scattering by diatomic molecules

For the purpose of this work we are interested in calculating the differential scattering cross section of diatomic molecules, in order to model the interaction between neutrons and molecular hydrogen. As described in chapter 1, the hydrogen molecule is composed of two atoms bound together, with an average length of the bond a. The molecule can vibrate along the joint and rotate about the centre of mass, which, in the case of H_2, is in the centre point of the bond. We can express the position of the $m-th$ hydrogen atom in terms of the vector $\boldsymbol{x_m}$:

$$\boldsymbol{x_m} = \boldsymbol{r_l} + (-)^n \frac{\boldsymbol{R_l}}{2} \tag{3.47}$$

where $\boldsymbol{r_l}$ is the position of the centre of mass of the $l-th$ molecule, and $\boldsymbol{R_l}$ expresses the coordinate of each atom in the $l-th$ molecule, by varying the index n. The index n can assume two values: n=1 and n=2, that represent the two atoms of the molecule, for which the coordinates have opposite signs.

We can rewrite equation 3.34 substituting the vector $\boldsymbol{x_m}$ to describe the scattering cross section of a hydrogen molecule:

$$\frac{d^2\sigma}{d\Omega dE'} = \frac{1}{2\pi\hbar}\frac{k'}{k}\sum_{\lambda'}\int_{\infty}^{\infty} dt[e^{i(\omega - E_\lambda + E_{\lambda'})\frac{t}{\hbar}}\sum_{l\neq j}\sum_{n,p=1}^{2}\langle\lambda|a_{jp}e^{-i\boldsymbol{q}\cdot\boldsymbol{r_j}-i(-)^p\frac{\boldsymbol{R_j}\cdot\boldsymbol{q}}{2}}|\lambda'\rangle\times$$
$$\langle\lambda'|a_{ln}e^{-i\boldsymbol{q}\cdot\boldsymbol{r_l}-i(-)^n\frac{\boldsymbol{R_l}\cdot\boldsymbol{q}}{2}}|\lambda\rangle]_T +$$
$$+\frac{1}{2\pi\hbar}\frac{k'}{k}\sum_{\lambda'}\int_{\infty}^{\infty} dt[e^{i(\omega - E_\lambda + E_{\lambda'})\frac{t}{\hbar}}\sum_{l}\sum_{n,p=1}^{2}\langle\lambda|a_{lp}e^{-i\boldsymbol{q}\cdot\boldsymbol{r_l}-i(-)^p\frac{\boldsymbol{R_l}\cdot\boldsymbol{q}}{2}}|\lambda'\rangle\times$$
$$\langle\lambda'|a_{ln}e^{-i\boldsymbol{q}\cdot\boldsymbol{r_l}-i(-)^n\frac{\boldsymbol{R_l}\cdot\boldsymbol{q}}{2}}|\lambda\rangle]_T \tag{3.48}$$

Where the subscript T means that the thermal average is taken over the initial states as in equation 3.34. One can consider the second term equation 3.48, this term contains only the contribution of the molecule l, it can therefore be referred to as a self term. One can now rewrite the wave functions of the states λ and λ'. Assuming that the translational modes can be separated from rotational and vibrational modes, we call Ψ_{it} the initial wave function of the translational modes, and Ψ_i and Ψ_f the initial and final roto-vibrational and spin dependent wave functions. The self term becomes:

$$\frac{d^2\sigma_s}{d\Omega dE'} = \frac{1}{2\pi\hbar}\frac{k'}{k}\sum_{f}\int_{\infty}^{\infty} dt\sum_{l}\langle\Psi_{it}|e^{-i\boldsymbol{q}\cdot\boldsymbol{r_l}(0)}e^{i\boldsymbol{q}\cdot\boldsymbol{r_l}(t)}|\Psi_{it}\rangle_T\times$$
$$\times\left[\left|\langle\Psi_f|\sum_{n=1}^{2}b_{ln}e^{(-)^n i\frac{\boldsymbol{q}\cdot\boldsymbol{R_l}}{2}}|\Psi_i\rangle\right|^2\times e^{i(\omega - E_i' + E_f')t/\hbar}\right]_T \tag{3.49}$$

Where we wrote $\boldsymbol{r_l}$ in the Heisenberg notation as in 3.37. It is important to note that now E_i' and E_f' refer only to the roto-vibrational and spin dependent energies of the initial and final states, instead of the total energies of the system. Let us call the matrix element in the second part of equation 3.49 $g(t)$, which is defined as:

$$g(t) = \left[\sum_{f}\left|\langle\Psi_f|\sum_{n=1}^{2}b_{ln}e^{(-)^n i\frac{\boldsymbol{q}\cdot\boldsymbol{R}}{2}}|\Psi_i\rangle\right|^2 e^{i(\omega - E_i' + E_f')t/\hbar}\right]_T \tag{3.50}$$

We now compute $g(t)$ taking into account the nuclear spin correlations. The

explicit form of $g(t)$ is:

$$g(t) = \sum_{J,S} \frac{P_{JS}}{2J+1} \frac{1}{2S+1} \frac{1}{2} \sum_{\sigma_z \sigma'_z = \pm\frac{1}{2}} \sum_{J'} e^{i(E_{J'} - E_J)t/\hbar} \times$$
$$\times \sum_{n=0} e^{in\omega t} \sum_{m_J m'_J} \sum_{S'} \sum_{S_z S'_z} |\langle J' m'_J, S' S'_z, \sigma'_z, n | B | J m_J, S S_z, \sigma_z, n = 0 \rangle|^2 \tag{3.51}$$

Here the thermal average was written in its explicit form, P_{JS} is the statistical weight of initial rotational state J with spin S. J and J' are initial and final angular momenta of the hydrogen molecule, with their z components m_J and m'_J. Similarly, S and S', as well as S_z and S'_z, are referred to initial and final spin states. The initial and final z components of the neutron spin are indicated by σ_z and σ'_z. Since the Hamiltonian is spin independent and we neglect the coupling between rotations and vibrations it is possible to state that:

$$|J, S, n\rangle = |J\rangle \, |S\rangle \, |n\rangle \tag{3.52}$$

The rotational energies E_J are given by 1.24. In terms of ω we can write the vibrational energy, that in the case of hydrogen is $\hbar\omega = 0.546 \; eV$. The molecules are initially in the vibrational ground state, $n = 0$. The parameter B resumes exponential terms of the two hydrogen atoms as:

$$M = b_1 e^{i\boldsymbol{q}\cdot\frac{\boldsymbol{R}}{2}} + b_2 e^{-i\boldsymbol{q}\cdot\frac{\boldsymbol{R}}{2}} \tag{3.53}$$

3.3.1 Spin correlations

Let us now construct the scattering length operator $\hat{b}$, in order to rewrite the parameter B. The total spin of the neutron-proton system $\hat{t}$ can assume two different values depending on the neutron spin. This results in two possible states, that we will call $|+\rangle$ and $|-\rangle$, that represent respectively the state with positive neutron spin $\frac{1}{2}$ and negative neutron spin $-\frac{1}{2}$. Applying $\hat{b}$ to those states we obtain the two different values of the scattering length as:

$$\hat{b} \, |\pm\rangle = b_\pm \, |\pm\rangle \tag{3.54}$$

It is possible to express the scattering length operator as a function of the nuclear spin of the nucleus $\boldsymbol{I_m}$ and the neutron spin $\boldsymbol{\sigma}$ as:

$$\hat{b} = A + B\boldsymbol{I_m} \cdot \boldsymbol{\sigma} \tag{3.55}$$

where the values of the constants A and B can be found by remembering how the operators $\hat{I_m}$, $\hat{\sigma}$ and $\hat{t}$ act on the states $|+\rangle$ and $|-\rangle$:

$$\hat{t^2} |\pm\rangle = t_\pm(t_\pm + 1) |\pm\rangle \tag{3.56}$$

$$\hat{I_m^2} |\pm\rangle = I_m(I_m + 1) |\pm\rangle \tag{3.57}$$

$$\hat{\sigma^2} |\pm\rangle = \frac{1}{2}\frac{3}{2} |\pm\rangle \tag{3.58}$$

Where we specified the neutron spin, but not the nucleus spin, so that we can discuss a more general case.

Since:

$$\hat{t^2} = \hat{I_m^2} + \hat{\sigma^2} + 2\hat{I_m} \cdot \hat{\sigma} \tag{3.59}$$

it is possible to show that:

$$\hat{I_m} \cdot \hat{\sigma} |+\rangle = \frac{I_m}{2} |+\rangle \tag{3.60}$$

$$\hat{I_m} \cdot \hat{\sigma} |-\rangle = -\frac{I_m + 1}{2} |-\rangle \tag{3.61}$$

Finally solving for A and for B the equations:

$$\begin{aligned} b_+ &= A + B\frac{I_m}{2} \\ b_- &= A - B\frac{I_m + 1}{2} \end{aligned} \tag{3.62}$$

we find that:

$$b_m = \frac{I_m + 1 + 2\boldsymbol{I_m} \cdot \boldsymbol{\sigma}}{2I_m + 1} b_+ + \frac{I_m - 2\boldsymbol{I_m} \cdot \boldsymbol{\sigma}}{2I_m + 1} b_- \tag{3.63}$$

It is possible to define the coherent and incoherent scattering lengths by weigh-

ing the two scattering lengths b_+ and b_- with their statistical weight. This gives:

$$b_{coh}^2 = <b>^2 = [\frac{1}{(2I+1)^2}][(I+1)b_+ + Ib_-]^2 = \frac{1}{16}(3b_+ + b_-)^2 \tag{3.64}$$

$$b_{inc}^2 = <b^2> - <b>^2 = [\frac{I(I+1)}{(2I+1)^2}][b_+ + b_-]^2 = \frac{3}{16}(b_+ + b_-)^2 \tag{3.65}$$

Since I_m is the hydrogen spin $I_m = \frac{1}{2}$. The total spin of the molecule is given by $I_1 + I_2 = S = 1$, B becomes:

$$\frac{M}{2} = b_{coh}\cos\left(\frac{\boldsymbol{q}\cdot\boldsymbol{R}}{2}\right) + \frac{2}{\sqrt{3}}b_{inc}\left[\cos\left(\frac{\boldsymbol{q}\cdot\boldsymbol{R}}{2}\right)\boldsymbol{\sigma}\cdot\boldsymbol{S} + i\sin\left(\frac{\boldsymbol{q}\cdot\boldsymbol{R}}{2}\right)\boldsymbol{\sigma}\cdot(\boldsymbol{I_2} - \boldsymbol{I_2})\right] \tag{3.66}$$

We can now distinguish between cases with same of different parity. States with same parity have the same molecular spin S, in this case only the symmetric part of B contributes to the matrix element. If we call α the initial state, and β the final state, we have that:

$$|\langle\beta|M|\alpha\rangle_{S=S'}|^2 = |\langle J'm'_J n|\cos\left(\frac{\boldsymbol{q}\cdot\boldsymbol{R}}{2}\right)|Jm_J n=0\rangle|^2 \times |\langle\sigma'_z S' S'_z|P|\sigma_z S S_z\rangle|^2 \tag{3.67}$$

where P is given by:

$$P = 2b_{coh} + \frac{4}{\sqrt{3}}b_{inc}\boldsymbol{\sigma}\cdot\boldsymbol{S} \tag{3.68}$$

If we sum over the final spin states, using the closure relation as in 3.36 we get:

$$\sum_{\sigma'_z S' S'_z} |\langle\beta|M|\alpha\rangle|^2 = |\langle J'm'_J n|\cos\left(\frac{\boldsymbol{q}\cdot\boldsymbol{R}}{2}\right)|Jm_J n=0\rangle|^2 \times \langle\sigma_z S S_z|P^2|\sigma_z S S_z\rangle \tag{3.69}$$

Where:

$$P^2 = 4b_{coh}^2 + \frac{16}{3}b_{inc}^2(\boldsymbol{\sigma}\cdot\boldsymbol{S})^2 + \frac{16}{\sqrt{3}}a_{coh}a_{inc}\boldsymbol{\sigma}\cdot\boldsymbol{S} \tag{3.70}$$

We also want to sum over the neutron spin states σ_z. In doing so, the matrix element given by the last term of 3.70 averages to zero. The first term is easily

computable, while the second one depends on the eigenvalues of $\boldsymbol{S^2}$, since:

$$\sum_{\sigma_z} \langle \sigma_z | (\boldsymbol{\sigma} \cdot \boldsymbol{S}) | \sigma_z \rangle = \frac{1}{2} \boldsymbol{S^2} \tag{3.71}$$

Therefore summing over the neutron spin states we obtain:

$$\sum_{\sigma_z} \langle \sigma_z S S_z | P^2 | \sigma_z S S_z \rangle = 8[b_{coh}^2 + \frac{1}{3} b_{inc}^2 S(S+1)] \tag{3.72}$$

We can now sum over S and substitute 3.69 and 3.72, we obtain the term $g(t)$ for the spin-conserving transitions

$$\begin{aligned} g_{S=S'}(t) =& 4 \sum_J \frac{P_{JS}}{2J+1} [b_{coh}^2 + \frac{b_{inc}^2}{3} S(S+1)] \times {\sum_{J'}}' e^{i(E_{J'}+E_J)t/\hbar} \sum_{n=0} e^{in\omega t} \times \\ & \times \sum_{m_J m'_J} | \langle J' m'_J n | \cos\left(\frac{\boldsymbol{q} \cdot \boldsymbol{R}}{2} \right) | J m_J n = 0 \rangle |^2 \end{aligned} \tag{3.73}$$

where we indicate the sum over J' states of same parity as J with the symbol $\sum'$.

The same can be done for transitions between states of opposite parity, choosing only the antisymmetric part of B as in:

$$| \langle \beta | M | \alpha \rangle |^2_{S \neq S'} = | \langle J' m_J n | \sin\left(\frac{\boldsymbol{q} \cdot \boldsymbol{R}}{2} \right) | J m_J n = 0 \rangle |^2 \times | \langle \sigma'_z S' S_z ` | Q | \sigma_z S S_z \rangle |^2 \tag{3.74}$$

where:

$$Q = (\frac{4}{\sqrt{3}}) b_{inc} \boldsymbol{\sigma} (\boldsymbol{I_1} - \boldsymbol{I_2}) \tag{3.75}$$

We once again sum over final spin states and using:

$$\sum_{\sigma_z} \langle \sigma_z | [\boldsymbol{\sigma} \cdot (\boldsymbol{I_1} - \boldsymbol{I_2})]^2 | \sigma_z \rangle = \frac{1}{2} (\boldsymbol{I_1} - \boldsymbol{I_2})^2 = \boldsymbol{I_1^2} + \boldsymbol{I_2^2} - \frac{1}{2} \boldsymbol{S^2} \tag{3.76}$$

we find $g(t)$ for states with different parity, where we indicate with the symbol $\sum''$

the sum over states J' with different parity compared to J.

$$\begin{aligned} g_{S\neq S'}(t) =& 4\sum_J \frac{P_{JS}}{2J+1} b_{inc}^2 [1 - \frac{S(S+1)}{3}] \times \sum_{J'}{}'' e^{i(E_{J'}-E_j)t/\hbar} \sum_{n=0} e^{in\omega t} \times \\ & \times \sum_{m_J m'_J} |\left\langle J' m'_J n \right| \sin\left(\frac{\boldsymbol{q}\cdot\boldsymbol{R}}{2}\right) |Jm_J n = 0\rangle|^2 \end{aligned} \tag{3.77}$$

3.3.2 Vibrations

The molecules are able to vibrate along their H-H bond, we call x the amount the bond is stretched, if the average length of the bond is a the total length of the bond is $R = a + x$. All the molecules are initially in their ground vibrational states, vibrational transitions are only relevant when the energy of the incident neutron is high ($\frac{q^2}{8M\omega} > 1$). We can write the stretch x as a function of phonon creation and annihilation operators a and $a^\dagger$ as:

$$x = i\frac{1}{\sqrt{M\omega\hbar}}[a - a^\dagger] \tag{3.78}$$

We can therefore further explicate the matrix elements in 3.73 and 3.77 substituting R into:

$$\langle n| e^{\pm i\frac{qR\cos\theta}{2}} |0\rangle = e^{\pm i\frac{qa\cos\theta}{2}} \langle n| e^{\mp\frac{q\cos\theta}{2\sqrt{M\omega}}(a-a^\dagger)} |0\rangle \tag{3.79}$$

where θ is the angle between $\boldsymbol{q}$ and $\boldsymbol{R}$. Observing that:

$$e^A e^B = e^{A+B+\frac{1}{2}[A,B]} \tag{3.80}$$

we can rewrite the matrix element of 3.73 as:

$$\begin{aligned} & |\left\langle J' m_J \text{`} n \right| \cos\left(\frac{\boldsymbol{q}\cdot\boldsymbol{R}}{2}\right) |Jm_J n = 0\rangle|^2 = \\ & = \left(\frac{q^2}{4M\omega}\right)^n \frac{1}{n!} |\left\langle J' m'_J \right| \cos^n\theta e^{-\frac{q^2\cos^2\theta}{8M\omega}} \left(\frac{e^{iqa\cos\theta/2} + (-)^n e^{-iqa\cos\theta/2}}{2}\right) |Jm_J\rangle|^2 = \\ & = \left(\frac{q^2}{4M\omega}\right)^n \frac{1}{n!} |\left\langle J' m'_J \right| \cos^n\theta e^{-\frac{q^2\cos^2\theta}{8M\omega}} e^{iqa\cos\theta/2}) |Jm_J\rangle|^2 \end{aligned} \tag{3.81}$$

which gives:

$$g_{S=S'}(t) = 4\sum_J \frac{P_{JS}}{2J+1}[b_{coh}^2 + \frac{b_{inc}^2}{3}S(S+1)]\times$$
$$\times \sum_{J'}{}' e^{i(E_{J'}-E_J)t/\hbar} \sum_n e^{in\omega t}\left(\frac{q^2}{4M\omega}\right)^n \frac{1}{n!}\sum_{m_J m'_J} |\langle J'm'_J|\cos^n\theta e^{-\frac{q^2\cos^2\theta}{8M\omega}+iqa\cos\theta/2)}|Jm_J\rangle|^2 \tag{3.82}$$

and similarly:

$$g_{S\neq S'}(t) = 4\sum_J \frac{P_{JS}}{2J+1}b_{inc}^2[1-\frac{S(S+1)}{3}]\times$$
$$\times \sum_{J'}{}'' e^{i(E_{J'}-E_J)t/\hbar} \sum_{n=0} e^{in\omega t}\left(\frac{q^2}{4M\omega}\right)^n \frac{1}{n!}\sum_{m_J m'_J} |\langle J'm'_J|\cos^n\theta e^{-\frac{q^2\cos^2\theta}{8M\omega}+iqa\cos\theta/2)}|Jm_J\rangle|^2 \tag{3.83}$$

3.3.3 Rotations

Assuming there is no coupling between rotational and vibrational motion, and that the rotation is not hindered, the wavefunctions of the rotational states are simply the spherical harmonics:

$$|Jm_J\rangle = Y_{Jm_J}(\theta,\phi) \tag{3.84}$$

Knowing this, the rotational matrix elements can be written as:

$$\langle J'm'_J|\cos^n\theta e^{-\frac{q^2\cos^2\theta}{8M\omega}+i\frac{qa\cos\theta}{2}}|Jm_J\rangle = \int d\Omega\cos^n\theta e^{-\frac{q^2\cos^2\theta}{8M\omega}+i\frac{qb\cos\theta}{2}}Y_{J'm'_J}(\theta,\phi)\times Y_{Jm_J}(\theta,\phi) \tag{3.85}$$

Let us now apply the coupling theorem for the spherical harmonics, which states:

$$Y_{l_1m_1}(\theta,\phi)Y_{l_2m_2}(\theta,\phi) = \sum_{l=|l_1-l_2|}^{l_1+l_2}\left(\frac{(2l_1+1)(2l_2+1)}{4\pi(2l+1)}\right)^{1/2}\times$$
$$\times C(l_1l_2l;m_1m_2)C(l_1l_2l;00)Y_{l,m_1+m_2}(\theta,\phi) \tag{3.86}$$

Where $C(l_1 l_2 l; m_1 m_2)$ are the Clebsch-Gordan coefficients. It is important to note that the Clebsch-Gordan coefficients vanish for $m_1 = m_2 = 0$ unless $l_1 + l_2 + l$ is even. We can apply the coupling theorem remembering that $Y^*_{l,m} = (-1)^m Y_{l,-m}$

$$\langle J' m'_J | \cos^n\theta e^{-\frac{q^2\cos^2\theta}{8M\omega} + i\frac{qb\cos\theta}{2}} | J m_J \rangle = \delta_{m'_J m_J} (-)^{m'_J} \sum_{l=|J'-J|}^{J'+J} \left(\frac{(2J'+1)(2J+1)}{4\pi(2l+1)} \right)^{1/2} \times$$
$$\times C(JJ'l; m_J m'_J) C(JJ'l; 00) \int d\Omega \cos^n\theta e^{-\frac{q^2\cos^2\theta}{8M\omega} + i\frac{qb\cos\theta}{2}} Y_{l,m_J - m'_J}(\theta, \phi) \tag{3.87}$$

Using the closure relation of the Clebsch-Gordan coefficients:

$$\sum_{m_J} C(JJ'l'; m_J - m_J) C(JJ'l; m_J - m_J) = \delta_{ll'} \tag{3.88}$$

and defining the constant A_{nl} in terms of the Legendre polynomial $P_l(\cos\theta)$:

$$A_{nl} = \int_{-1}^{1} d\cos\theta \cos^n\theta e^{-\frac{q^2\cos^2\theta}{8M\omega} + i\frac{qb\cos\theta}{2}} P_l(\cos\theta) \tag{3.89}$$

we can once again rewrite g(t) as:

$$g_{S=S'}(t) = [b^2_{coh} + \frac{b^2_{inc}}{3} S(S+1)] \sum_J P_{JS} \times$$
$$\times \sum_{J'}{}' e^{i(E_{J'} - E_J)t/\hbar} (2J'+1) \sum_n e^{in\omega t} \left(\frac{q^2}{4M\omega} \right)^n \frac{1}{n!} \sum_{l=|J'-J|}^{J'+J} |A_{nl}|^2 \times C^2(JJ'l; 00) \tag{3.90}$$

and similarly:

$$g_{S\neq S'}(t) = b^2_{inc}[1 - \frac{S(S+1)}{3}] \sum_J P_{JS} \times$$
$$\times \sum_{J'}{}'' e^{i(E_{J'} - E_J)t/\hbar} \sum_{n=0} e^{in\omega t} \left(\frac{q^2}{4M\omega} \right)^n \frac{1}{n!} \sum_{l=|J'-J|}^{J'J} | \langle J' m'_J | \cos^n\theta e^{-\frac{q^2\cos^2\theta}{8M\omega} + iqa\cos\theta/2}) | J m_J \rangle |^2 \tag{3.91}$$

3.3.4 Translations

It is possible to assume that the translations are free, in this case we can solve the translational part of 3.49 independently as:

$$\langle \Psi_{it} | e^{-iq\cdot \boldsymbol{r_l}(0)} e^{iq\cdot \boldsymbol{r_l}(t)} | \Psi_{it} \rangle_T = e^{-\frac{q^2\hbar^2}{4M}(-i+tT)} \tag{3.92}$$

3.3.5 Scattering cross sections

We are finally able to write the equations for the self term scattering cross section, for pH_2 and oH_2, by using equations 3.90 and 3.91 as well as 3.92, inside 3.49:

$$\begin{aligned}\left(\frac{d\sigma_s}{d\Omega dE'}\right)_{para} &= \frac{k'}{k}\left(\frac{M}{\pi q^2 T}\right)^{1/2} \sum_n \frac{1}{n!}\left(\frac{q^2\hbar^2}{4M\omega}\right) \sum_{J=0,2,4...} P_J \times \\ &\times [b_{coh}^2 \sum_{J'=0,2,4...} + b_{inc}^2 \sum_{J'=1,3,5...}] \times (2J'+1) e^{-\frac{(E'+\Delta E+\frac{q^2}{4M})^2}{q^2 T/M}} \times \\ &\times \sum_{l=|J'-J|}^{J'+J} |A_{nl}|^2 \times C^2(JJ'l;00)\end{aligned} \tag{3.93}$$

$$\begin{aligned}\left(\frac{d\sigma_s}{d\Omega dE'}\right)_{ortho} &= \frac{k'}{3k}\left(\frac{M}{\pi q^2 T}\right)^{1/2} \sum_n \frac{1}{n!}\left(\frac{q^2\hbar^2}{4M\omega}\right) \sum_{J=1,3,5...} P_J \times \\ &\times [b_{inc}^2 \sum_{J'=0,2,4...} + (3b_{coh}+2b_{inc}^2) \sum_{J'=1,3,5...}] \times (2J'+1) e^{-\frac{(E'+\Delta E+\frac{q^2}{4M})^2}{q^2 T/M}} \times \\ &\times \sum_{l=|J'-J|}^{J'+J} |A_{nl}|^2 \times C^2(JJ'l;00)\end{aligned} \tag{3.94}$$

The same equations can be written for low temperatures, where the molecules are in their ground rotational as well as vibrational states:

$$\begin{aligned}\left(\frac{d\sigma_s}{d\Omega dE'}\right)_{para} &= \frac{k'}{k}\left(\frac{M}{\pi q^2 T}\right)^{1/2} \sum_n \frac{1}{n!}\left(\frac{q^2\hbar^2}{4M\omega}\right) \times [b_{coh}^2 \sum_{J'=0,2,4...} + b_{inc}^2 \sum_{J'=1,3,5...}] \times \\ &\times (2J'+1) e^{-\frac{(E'+E_{J'}+n\omega-\frac{q^2}{4M})^2}{q^2 T/M}} \times |A_{nJ'}|^2\end{aligned} \tag{3.95}$$

$$\left(\frac{d\sigma_s}{d\Omega dE'}\right)_{ortho} = \frac{k'}{3k}\left(\frac{M}{\pi q^2 T}\right)^{1/2} \sum_n \frac{1}{n!}\left(\frac{q^2\hbar^2}{4M\omega}\right) \times$$
$$\times [b_{inc}^2 \sum_{J'=0,2,4...} + (3b_{coh} + 2b_{inc}^2) \sum_{J'=1,3,5...}] \times \tag{3.96}$$
$$\times (2J'+1) e^{-\frac{(E'+E_{J'}+E_1+n\omega-\frac{q^2}{4M})^2}{q^2 T/M}} \times ((J'+1)|A_{n,J'+1}|^2 + J|A_{n,J'-1}|^2)$$

The same equations can be modified for the 2D rotor by considering the correct eigenvalues with their degeneracy, as well as a modified distribution P_J [52].

Using these formulas we are able to plot the neutron scattering cross section for ortho- and para- hydrogen, as well as for a certain concentration of the two, in the case of the 3D rotor.

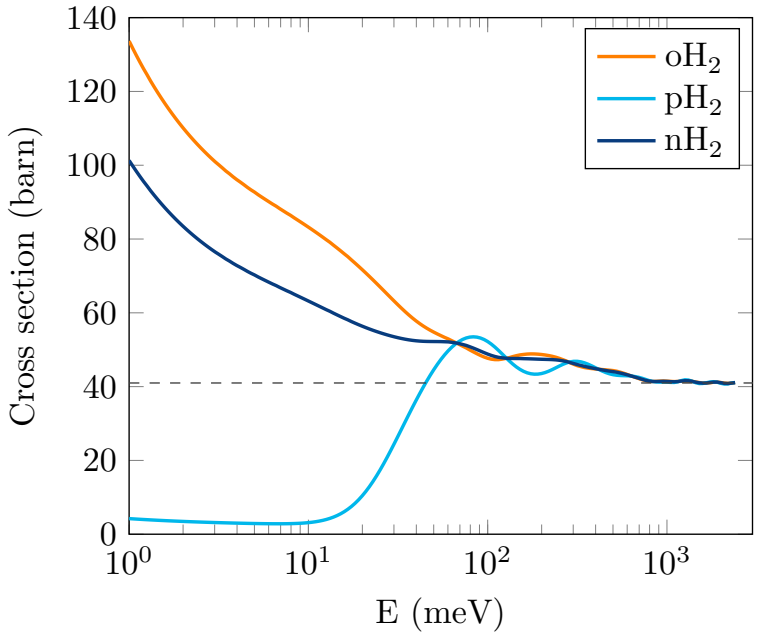

Figure 3.1: Neutron cross sections for pH$_2$, oH$_2$, and normal hydrogen (nH$_2$) as a function of neutron energy for a 3D rotor. The normal hydrogen curve corresponds to a pH$_2$ concentration of 25%, typical of the room temperature system. The dashed line represents the limit of free scattering cross section [53].

Figure 3.1 shows the scattering cross sections for pH$_2$, oH$_2$ and normal hydrogen nH$_2$, as a function of the energy of the neutron. The dashed line represents the

limit of free scattering cross section σ_f, defined as:

$$\sigma_f = 4\pi b_f^2 \tag{3.97}$$

where:

$$b_f = \frac{b_{bound}}{m}\mu \tag{3.98}$$

which is the scattering length in the limit of a free atom. Both ortho- and para-cross section tend to σ_f at high energies because energetic neutrons interact with the two protons of the molecule as if they were free particles.

From figure 3.1 it is possible to notice that at lower neutron energies, in the range of cold and thermal neutrons, the scattering cross sections of ortho and para hydrogen differ by almost two orders of magnitude. This makes neutron scattering particularly useful to investigate the concentrations of the two modifications.

Chapter 4

Measurements and data analysis

The purpose of this experimental analysis is to investigate the ortho-para conversion and cross sections of molecular hydrogen adsorbed inside a metal organic framework, specifically HKUST-1. Experiments were performed at the IMAT beamline and at the VESUVIO beamline of the ISIS Neutron and Muon Source. In this chapter we illustrate the methods for data analysis and the experimental strategy, as well as the background noise correction procedures that were implemented on the images. The characteristic conversion time of the opC will be estimated for multiple regions of interest. Moreover we report the measured scattering cross section of adsorbed molecular hydrogen at 30 K, comparing it to theoretical models.

4.1 Software for data analysis

The data analysis was performed using multiple software, two of which are particularly popular in imaging processing and neutron data analysis: ImageJ and Mantid respectively. We will illustrate below their main caratheristics, while the programs used in the data analysis are reported in the appendices.

- **ImageJ**: ImageJ is an image processing program born from a collaboration between the National Institutes of Health of the United states and the Laboratory for Optical and Computational Instrumentation (LOCI, University of Wisconsin). The program is provided of Java plug-ins as well as recordable macros that allow the user to automate the imaging processing and analysis. ImageJ allows the user to manage stacks of radiographs, which contain images that are ordered as a function of time. Here, ImageJ was used to

perform the background noise corrections on the radiographs. Once the corrections were implemented on the stacks, it allowed us to extract the neutron transmission as a function of time [54][55].

- **Mantid**: Mantid is a software developed to analyse neutron scattering and muon spectroscopy data. It was created by the shared effort of the ISIS Neutron and Muon Facility, and the Oak Ridge National Laboratory. Mantid is a python based software that provides a framework for high performance data visualization and data analysis. In this work it was used to perform the fitting of neutron data, in order to infer the best trend for the ortho-para conversion [56].

4.2 Experimental procedure

The **imaging experiment** was performed at the IMAT beamline, where energy selective neutron imaging was implemented to obtain in situ/operando radiographs of the MOF. Before loading, the MOF was annealed for 1 day at a temperature of 453 K, in order to evaporate water molecules that would otherwise occupy adsorption sites. The MOF was then inserted into the sample container shown in figure 2.8, which was then loaded into the closed-circuit refrigerator (CCR). Hydrogen was first dosed inside the buffers, this is useful to control the amount of molecules inserted into the MOF. In order to only fill the first adsorption site, the amount of hydrogen was chosen so that there was one H_2 molecule for every Cu atom. Hydrogen was then slowly loaded into the sample container during data acquisition, using the gas panel. The temperature of the CCR was chosen to be of 17 K, this is because at this temperature free hydrogen is in its liquid form, making the loading procedure smoother.

By tuning the two double-disk choppers, the energy of the incident neutrons was chosen to be lower than 9 meV, in order to guarantee maximum contrast between ortho- and para-hydrogen. In fact, figure 3.1 shows how the para-hydrogen scattering cross section presents a plateaux at lower energies, and starts increasing around 9 meV. This is due to the inability to promote transitions from J=0 to J=1 at these lower energies. Here the cross section is only proportional to the coherent term.

The radiographs were acquired at regular time intervals in order to characterize the time dependence of the process. The data acquisition was started before the loading procedure in order to observe the hydrogen entering the sample container,

and therefore the MOF. During this initial phase, the exposure time is 5 s, in the final loading phase it is set at 15 s and after the hydrogen is fully loaded the exposure time is set at 30 s to observe the later stages opC. This is because the time scale of loading is faster than that of the opC.

The radiographs were acquired using the CCD camera described in paragraph 2.4.6, which works at a temperature of 203 K. The pinhole was chosen to be of 40 mm to reduce beam divergence. The imaging system provides a field of view of 20×20 cm^2.

Besides the radiographs of the sample, other two set of radiographs were acquired, which were used to perform background noise corrections. We will discuss those in the next paragraph.

The **transmission experiment** was performed at the VESUVIO beamline. The sample was prepared using the same procedure described above. The VESUVIO beamline is equipped with the same type of buffers as IMAT, therefore hydrogen was again dosed and loaded as above. Since VESUVIO is not equipped with choppers, this data is acquired on a much greater energy range, which allows us to better investigate the cross section. In this case we performed 3 runs at a temperature of 30 K, each one with a different hydrogen concentration. The three suns present a hydrogen concentration, compared to that of the Cu atoms, of 1:1.3, 1:1, and 1:2 respectively. These three concentrations were chosen because even though we are interest in having hydrogen only in the first adsorption site, the detector we used is particularly sensible to γ-rays, which contribute to a background that could ruin the measurements if hydrogen concentration is too low. In addition to the three runs containing hydrogen, transmission data of the MOF alone was also acquired, in order to perform a background correction.

4.3 Neutron imaging: background noise corrections

In order to perform the darkfield and flatfield corrections other two sets of data were acquired. For the darkfield correction the radiographs were acquired with the neutron beam turned off, to detect the electronic noise of the CCD camera. On the other hand for the flatfield correction the radiographs of the empty CCR are needed. Both sets of data were acquired at 5s, 15s, and 30s, in order to compare them with the H_2 radiographs. In the following section we will describe the procedure chosen to perform the corrections, which were implemented using the software ImageJ.

4.3.1 Darkfield correction

The purpose of this correction is to subtract detector artifacts, as dark current, bias current or readout noise, due to the properties of the CCD itself, as well as identify dark or hot pixels. The dark radiographs were acquired with the neutron beam turned off, in order to only capture the noise produced by the detector. Since the intensity due to the noise depends on the exposure time, the dark frames were acquired at the same exposure times as the H_2 data, which were chosen to be of 5, 15 and 30 s. For every exposure time, 50 frames were acquired, in order to average them out.

The purpose of this section is to obtain three images, one for every exposure time, that best represent the noise due to the CCD and can therefore be subtracted from the original data.

The three dark stacks appear to have a background electronic noise as well as some hot pixels, which are easily identifiable because they remain in a fixed position for every slice of the stack. Using the software ImageJ it is possible to perform different operations on the images: we compared three different filters that are often used to treat the dark frames:

- **Gaussian blur**: this filter performs a Gaussian blur on every slice of the stack, it is possible to select its standard deviation as a function of the number of pixels with the macro command:

```
run("Gaussian Blur...", "sigma=4 stack");
```

- **Remove outliers**: this filter replaces outlier pixels by the median of the pixels in the surrounding. It is possible to choose a threshold in terms of the standard deviation, to define which pixels are treated as outliers. The macro command is:

```
run("Remove Outliers", "block_radius_x=40 block_radius_y=40
    standard_deviations=3 stack");
```

  where the block radius indicates the radius used to calculate the median and substitute the value of the outlier. Both radius and standard deviation are given as a function of the number of pixels.

- **Median**: this filter replaces each pixel with the median of the value of neighboring pixels. It can be applied in 2D or 3D by changing the radius in the z direction, using the macro:

  ```
  run("Median 3D...", "x=2 y=2 z=2");
  ```

  where the third dimension is time. This means that the median is calculated using the preceding and following slices. The three parameters are again expressed as a function of the number of pixels used.

Figure 4.1 shows the three corrections compared with the original data. The left plot shows the pixel intensity evaluated along a line of pixels, as a function of the pixel number. The line was chosen with the purpose of showing a region with very intense outliers. The second plot represents the average intensity of the x-th column of pixels, as a function of the column number.

In figure 4.1 and 4.2, we chose to represent the corrections with the default standard deviations suggested by the software for each filter. In particular, the standard deviation of the Gaussian filter is over a radius of 4 pixels; the threshold that defines the outliers is of 3 standard deviations, calculated over a radius of 40 pixels; the median filter calculates the median in a 3D neighborhood with a 2 pixel radius.

Upon observing the radiographs it is possible to notice a lower intensity background that varies with time, and many hot pixels with higher intensity, that do not vary with time. It is important to chose the best way to treat such a system.

The "Gaussian filter" lowers the gray value of a hot pixel, but also increases the gray value of the surrounding pixels. While it seems to maintain the same average as the original data over the rectangle (figure 4.1b) in figure 4.1a it is possible to notice that the Gaussian blur induces a systematic error, since it presents peaks where the original data has a baseline. This effect is due to the fact that the intensity of neighbouring hot pixels on different lines is spread beyond their position, onto the observed line.

The filter "remove outliers" defines the outlier value based on the median of the surrounding pixels, for this reason not all the pixel with the same value are removed. Moreover the average value calculated over the rectangle appears to be lower than that of the original data, but higher than the average median (see figure 4.1b).

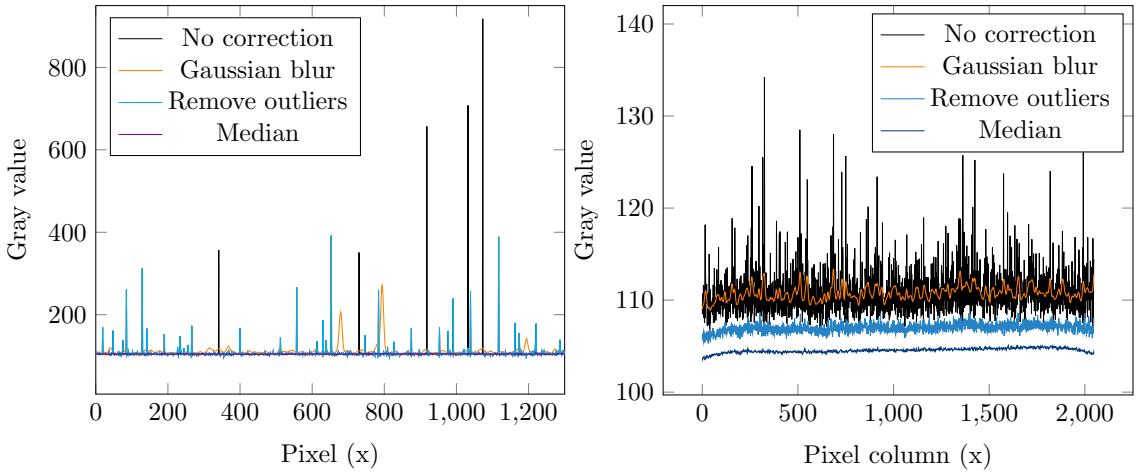

Figure 4.1: The three corrections are compared with the original data. In the first plot, each curve represents the grayvalue of the pixel as a function of the pixel number, the data were acquired along the line defined with the macro: 'makeLine(148, 720, 1448, 720)'. In the second image the grayvalue of every plot is an average of the pixels intensity along the x-th pixel column, this data were acquired with the macro: 'makeRectangle(0, 0, 2048, 2048)'.

The median filter on the other hand seems to better reproduce the background noise, but doesn't take into account hot pixels, for this reason its average over the rectangle is significantly lower than that of the original data.

In figure 4.2 the first two corrections are applied simultaneously, since the two filters do not commute, they were applied in both orders. When the Gaussian blur is applied before removing the outliers is still present a significant systematic error. Removing the outliers before applying the Gaussian blur gives a better result but it still doesn't treat hot pixels. Moreover, the Median alone still gives a better reproduction of the baseline of the noise. For this reason we choose to use the median filter to treat the Dark stacks. After the filter is applied the stacks are averaged out to create a single image that can be subtracted to implement the dark field correction, using the macro:

```
run("Grouped Z Project...","projection=[Average Intensity]
group="+nSlices);
```

While this correction is sufficient for the application in this work, usually it would be necessary to remove the white spots by designing a proper filter [57].

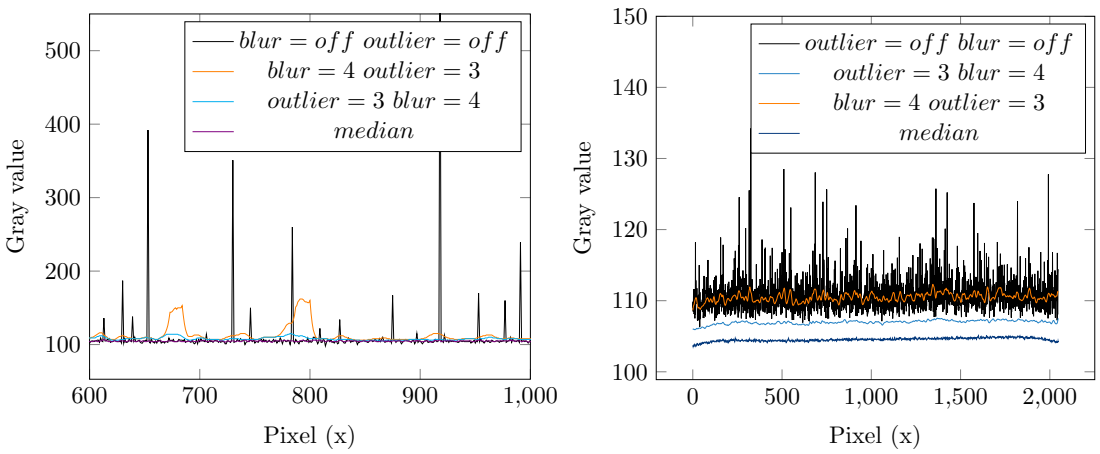

Figure 4.2: The functions "Gaussian blur" and "remove outliers" are applied sequentially. The order in which they are reported represents the order in which they were applied.In the first plot, each curve represents the grayvalue of the pixel as a function of the pixel number, the data were acquired along the line defined with the macro: 'makeLine(148, 720, 1892, 720)'. In the second image the grayvalue of every plot is an average of the pixels intensity along the x-th pixel column, this data were acquired with the macro: 'makeRectangle(0, 0, 2048, 2048)'.

The darkfield correction was applied not only to the sample radiographs, but also to the stack of radiographs of the empty CCR, used for the flatfield correction.

4.3.2 Flatfield correction

The flatfield correction consists of dividing the sample radiographs by a reference flatfield image, in order to obtain the neuron transmission due to the sample. This correction was performed using reference stacks of the empty CCR, that were acquired with acquisition times of 5 s, 15 s, and 30 s. For each of the three acquisition times multiple radiographs were taken, those will be averaged to obtain three flatfield images, that can be used to divide the sample radiographs with the corresponding acquisition time. Flatfield stacks are acquired by uniformly radiating the CCR with the neutron beam, thus obtaining images that contain informations on the transmission due to instrumental setup. For simplicity, the flatfield correction was performed on the empty CCR instead of the sample container. Just like sample radiographs, flatfield images record an intensity that depends on the camera artifacts, as well as the neutron transmission. Therefore the darkfield correction was also performed on the flatfield stacks.

When working with neutrons it is important to take into account that their flux may vary significantly from one radiography to another.

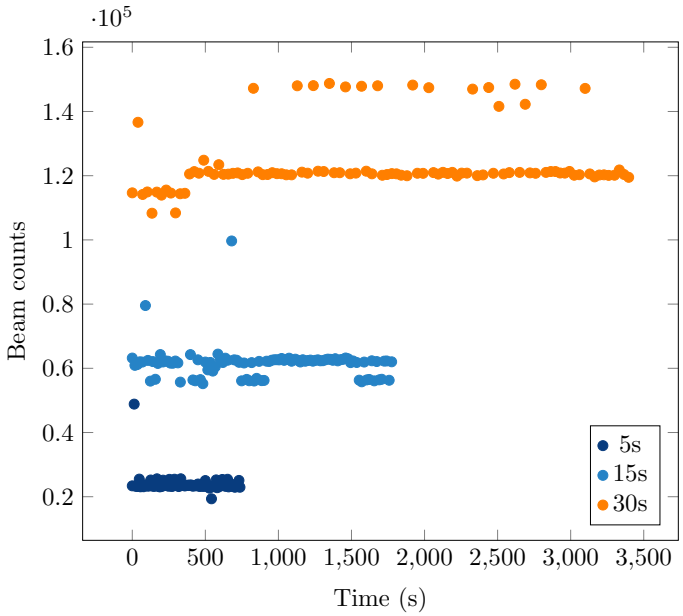

Figure 4.3: Beam counts as a function of time measured by the GS20 detector, for three different acquisition times.

Figure 4.3 reports as an example the beam counts as a function of time, registered during the experiment, for three different data acquisitions. The beam count represents the total number of neutrons that are measured by the GS20 monitor during the 5 s, 15 s or 30 s long data acquisitions. It is clear that this flux might vary significantly from one radiography to another, thus we have to take this into account when constructing the flatfield correction image. Two types of corrections were assessed:

- **Normalization correction**: this consists of normalizing each flatfield radiography by the number of its neutron counts. In order to obtain intensity values grater than one in each pixel, we actually divide by the number of counts of the respective radiography and multiply by the mean value of the counts of each radiography of the stack.
- **Standard deviation correction**: given the total number of counts of every slice in the stack, for each of the three acquisition times, it is possible to

construct its standard deviation. This number is used to discard slices that have a number of counts that exceeds the standard deviation, which are considered outliers.

The macros for both these corrections are shown in appendix B. It is important to notice that each of the corrections has to be implemented on a radiography where the blackfield is already been subtracted. Moreover once the correction is performed, the stack is again averaged to obtain one image, using the same macro command used to average the darkfield stacks.

The two corrections were compared to the image obtained by averaging the stack without implementing any correction. In order to compare them, each correction image was divided by the non-corrected image by using the macro:

```
imageCalculator("Divide create slice",
"AVG_Result of CCR_5s_PH40-1","AVG_Result of CCR_5s_PH40");
```

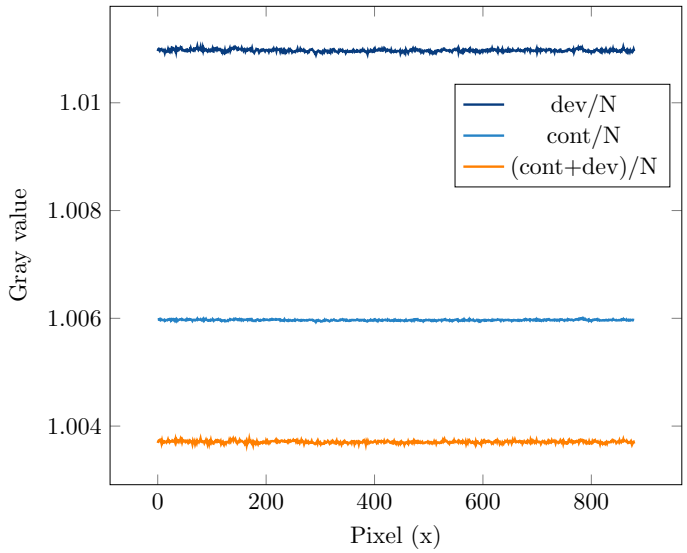

Figure 4.4: Comparison between normalization and standard deviation corrections, normalized by non-corrected image. This image only represents the central area obtained using the macro makeRectangle(556, 548, 880, 900);

Results are shown in figure 4.4. Both corrections do not differ more than 1% from the raw data average and therefore we consider them equally valid. We choose to treat flatfield images with the standard deviation correction assuming that the results would improve by excluding outliers. Moreover, not dividing each

radiography by the number of counts allows us to work with pixel that still have integer intensities.

4.3.3 Field of view correction

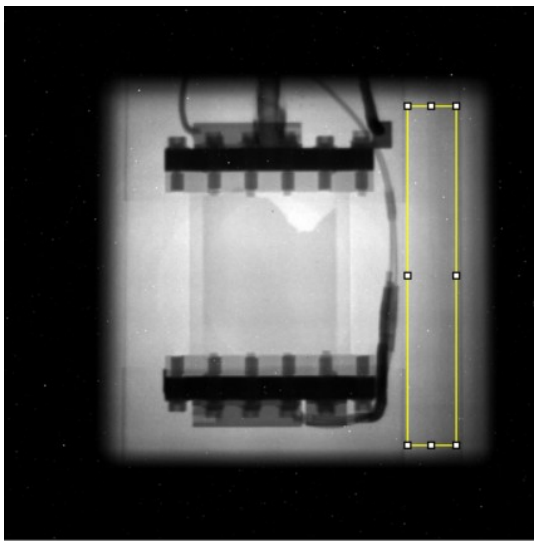

Figure 4.5: Example of a radiography showing the area chosen in order to perform the field of view correction, the area is identified with the macro: makeRectangle(1548, 384, 188, 1300);.

As shown in figure 4.3 the neutron flux has a strong time dependence that is due to the specifics of the source. It is therefore important to take into account that the number of transmitted neutrons also depends on the number of incident neutrons. A possible solution to this is to apply the normalization correction described before for the flatfield stacks, however it is preferred to use a field of view correction, for both flatfield and sample radiographs. This correction consists in selecting an area of each sample radiography, where the neutrons are being transmitted and the sample is not present. As an example figure 4.5 shows the area chosen for our setup. Using the function:

```
run("Measure");
```

It is possible to obtain the mean intensity of pixels in this area, that can be used to normalize the entire slice. This correction was performed on every slice of the sample stacks, but only after the other corrections were applied.

4.3.4 Implementation of corrections and systematic errors

The total implementation of background noise corrections allowed us to obtain three corrected stacks of radiographs that we will analyze in the next section. The operations that are performed on raw data to obtain the corrected stack can be summarized by the following formula:

$$\mathrm{STACK}_{\mathrm{Corrected}} = \frac{\mathrm{STACK}_{\mathrm{Raw}} - \mathrm{SLICE}_{\mathrm{Dark}}}{\mathrm{SLICE}_{\mathrm{Flat}} - \mathrm{SLICE}_{\mathrm{Dark}}} \tag{4.1}$$

Where $\mathrm{SLICE}_{\mathrm{Dark}}$ and $\mathrm{SLICE}_{\mathrm{Flat}}$ are the two images obtained by averaging the dark stacks and flat stacks, after corrections are performed, and $\mathrm{STACK}_{\mathrm{Raw}}$ is the stack of the raw sample data. After this operations were performed, the field of view correction was implemented on the corrected stacks. While interpreting the resulting stacks it is important to take into account that these corrections could induce some systematic errors. As an example, the method chosen to treat the dark stacks does not treat hot pixels, however for the purpose of this work we are going to average the transmission value on areas of the image that are big enough to neglect this error. Moreover, the intensity of hot pixels does not depend strongly on time, and its dependence is stochastic, therefore their contribution may constitute an off-set on the transmission value, but will not disrupt the time dependence of ortho-para conversion.

Another offset on the transmission is due to the fact that the flatfield correction is performed using empty CCR radiographs instead of radiographs of the MOF before hydrogen adsorption. However the MOF is a powder, which means that it could have different densities depending on the observed section, and it could move around during hydrogen loading. Therefore it was preferred to use a more uniform background. As a consequence, the material of the sample container is also not accounted for, however due to scattering cross section of aluminium being so small we can neglect this contribution.

The field of view correction was implemented assuming a uniform spatial distribution of neutrons in the incident beam, in order to reduce the error due to this correction the field of view was chosen to be as big as possible. It is also important to notice that scattered neutron can still reach the detector, disrupting the intensity of transmitted neutrons. Moreover the neutron source is not monoenergetic, therefore we neglect the error due to the energy dependence of the scattering processes [58].

All of the corrections that were performed in this work can more easily be

implemented using packages for tomographic data processing as NeuTomPy [59].

4.4 Neutron imaging for the catalysed ortho-para conversion

In this section we will describe the procedure used to obtain the characteristic conversion time of the catalysed ortho-para conversion. In particular, this procedure will be implemented in multiple regions of interest, obtaining a grid of values for the conversion time, which allowed us to explore the spatial distribution of this phenomenon.

4.4.1 Ortho-para conversion: transmission measurements

Once the raw transmission data has been treated following the procedure in the previous section, it is possible to extract time dependence of the measured transmission by using the following ImageJ command on a selected area:

```
run("Plot Z-axis Profile");
```

Given a certain stack of radiographs, this function will plot the selected area mean gray value versus the slice number. Since the slices inside the stack progress as a function of time, this allowed us to extract a time dependence. Before using the command above, it is important to choose the region of interest (ROI) of which we want to extract the time dependent transmission. ROIs can be selected using the macro:

```
makeRectangle(x, y, width, height)
```

This creates a rectangle that has the top left corner in the coordinates (x,y), which are expressed as a function of the number of pixels, and has specified width and height. Ideally, one could choose a ROI as big as the whole sample, however this area is too big to obtain meaningful results because hydrogen may not reach every point of the sample, and does not reach them simultaneously. Therefore we want to investigate multiple smaller ROIs and compare the results. We choose ROIs of 50×50 pixels, which roughly correspond to 1 cm^2 sections of the sample. As an example, we chose to represent five different ROIs, labeled with letters from A to E. These are defined by varying the y coordinate and maintaining the x fixed, therefore varying the depth within the sample. Figures from 4.6 to 4.10 report the

location of the five ROIs, as well as plots of the average pixel grayvalue in that area, which is proportional to transmission, as a function of time.

Every plot is constituted of three curves following each other: each one refers to a different stack, acquired at a certain acquisition time.

As mentioned before, slices were acquired with shorter acquisition times during loading because this process has a shorter time scale compared to the opC.

Observing the plots in figures from 4.6 to 4.10, it is possible to notice an initial plateaux, which represents the value of the transmission before hydrogen is loaded. Here, transmission depends on the scattering cross section of sample container and MOF, and it is therefore constant as a function of time.

After a couple of minutes, the hydrogen is loaded: this is when the scattering cross section increases abruptly, consequently decreasing transmission.

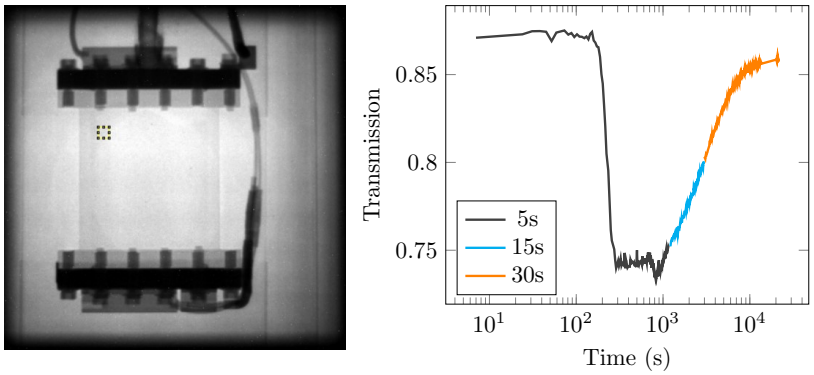

Figure 4.6: ROI A, selected with the function 'makeRectangle(800, 800, 50, 50)'

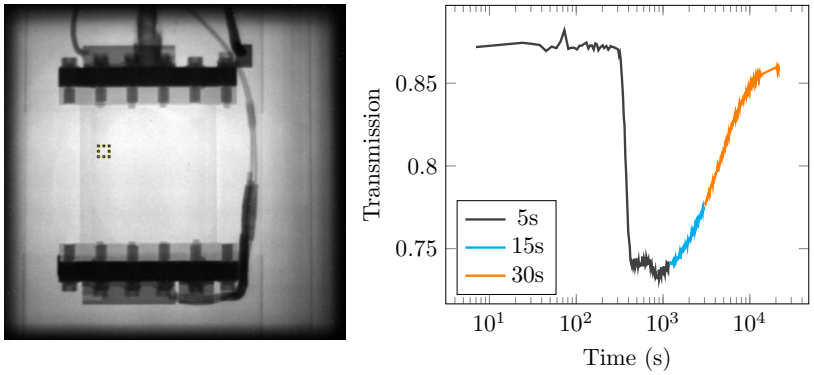

Figure 4.7: ROI B, selected with the function 'makeRectangle(800, 900, 50, 50)'

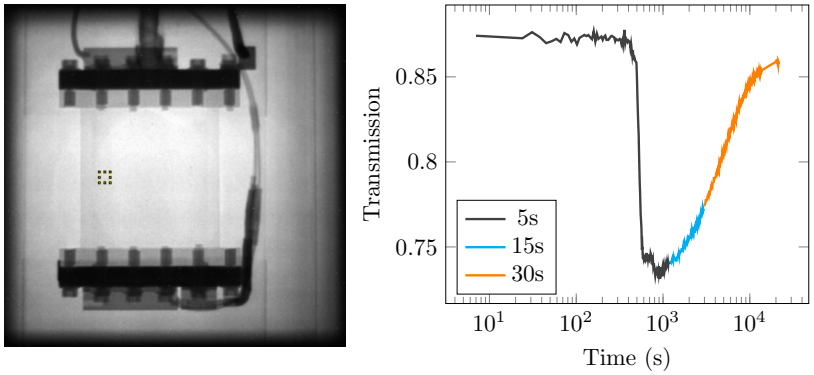

Figure 4.8: ROI C, selected with the function 'makeRectangle(800, 1000, 50, 50)'

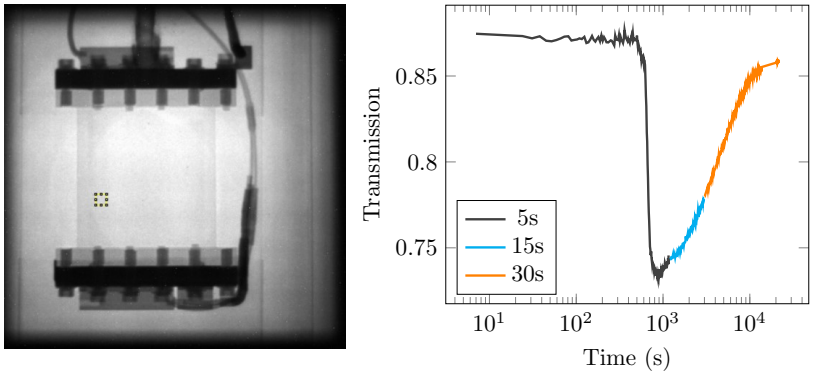

Figure 4.9: ROI D, selected with the function 'makeRectangle(800, 1100, 50, 50)'

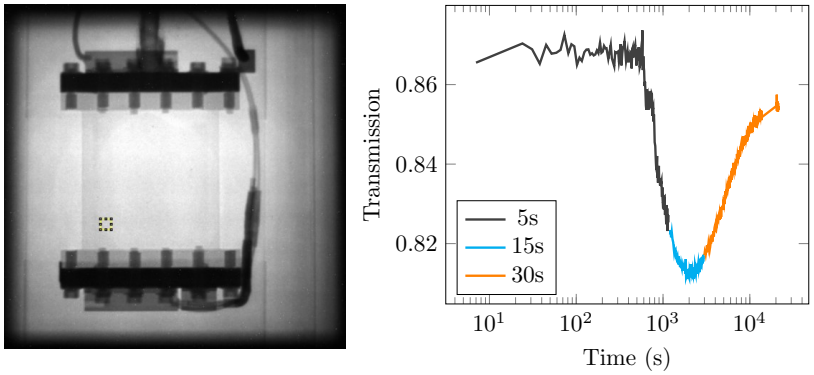

Figure 4.10: ROI E, selected with the function 'makeRectangle(800, 1200, 50, 50)'

The jump in the transmission depends on the fact that loading is fast compared to the almost three hours long experiment. However, comparing plots from 4.6 to 4.10, it is possible to notice the hydrogen molecules percolating inside the powder by observing that the transmission jump happens slightly later at the bottom of the container.

Especially for the ROIs that are closer to the surface, transmission is slightly disturbed by the hydrogen loading, because the powder moves around. After loading is complete, the ortho-para conversion is clearly visible in each graph. The same measurements are performed for other four ROIs, which were chosen in order to sample the superficial layers of the powder. These ROIs have the same dimension as before (50×50 pixels), and are labeled with letters from F to I (figures from 4.11 to 4.14).

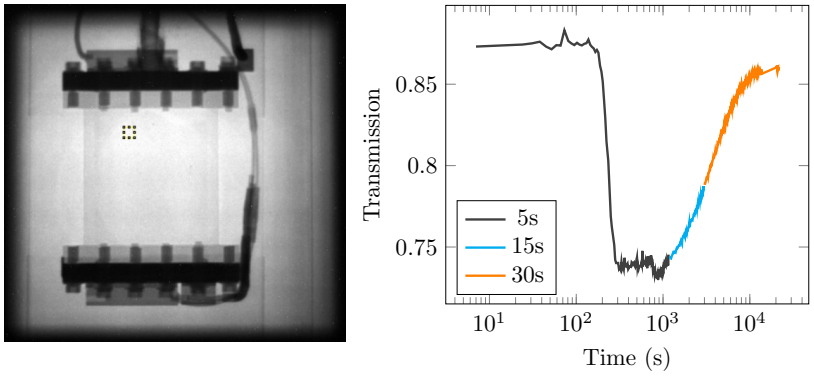

Figure 4.11: ROI F, selected with the function 'makeRectangle(900, 800, 50, 50)'

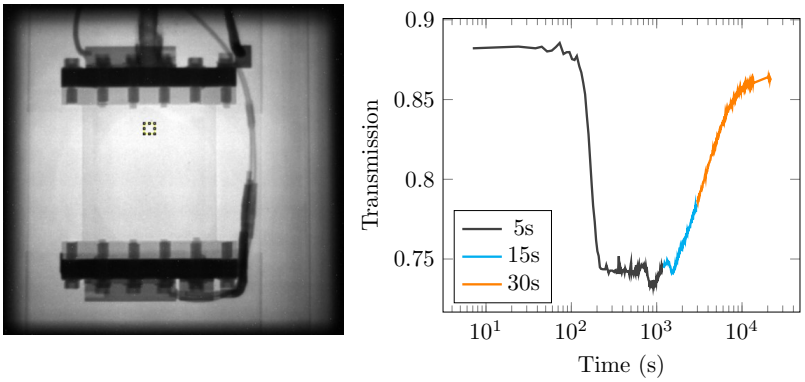

Figure 4.12: ROI G, selected with the function 'makeRectangle(1000, 800, 50, 50)'

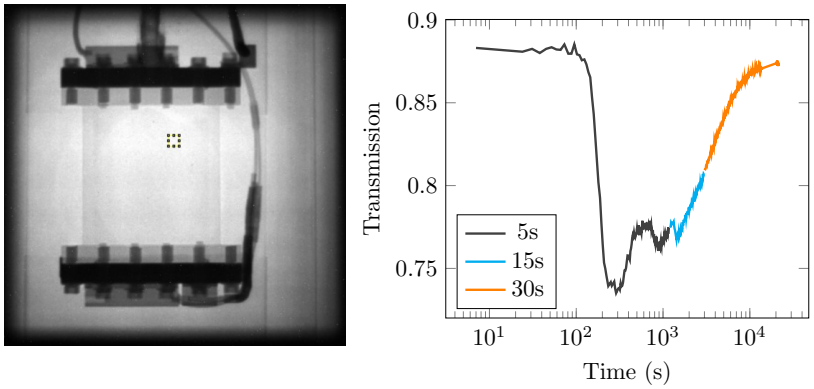

Figure 4.13: ROI H, selected with the function 'makeRectangle(1100, 850, 50, 50)'

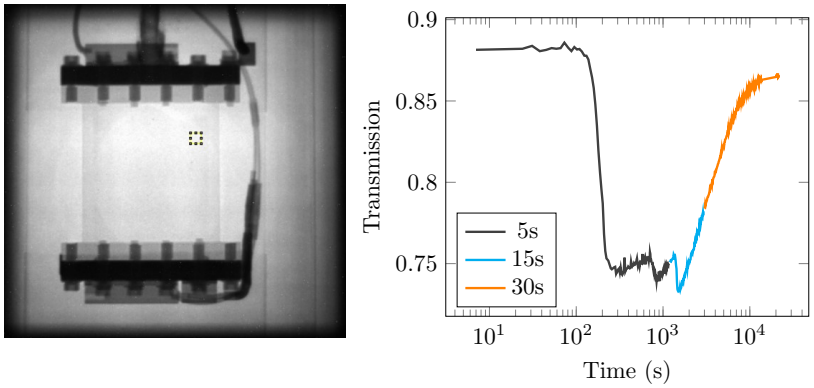

Figure 4.14: ROI I, selected with the function 'makeRectangle(1200, 850, 50, 50)'

It is possible to notice a more complex behaviour for those ROIs that are closer to the surface. In particular, ROI H and I are very close to a region where the powder is absent, near the top right corner of the container. The absence of powder is noticeable because the area is lighter in color, due to higher transmission.

4.4.2 Characteristic conversion time

From transmission plots obtained in the previous section, it is possible to extract the time dependence of the ortho-hydrogen concentration. To do so, we firstly consider the Beer-Lambert law (equation 2.6) introduced in chapter 2. In our specific case, transmission depends on multiple terms: we need to take into account the sample container, the MOF powder, and the two hydrogen modifications.

However, only the concentrations of ortho- and para-hydrogen have a time dependence, therefore we can consider transmission due to sample container and MOF as a multiplying constant. The Beer-Lambert law becomes:

$$T = T_{MOF}T_{container}e^{-o(t)\sigma_o x}e^{-(1-o(t))\sigma_p x} = T_s T_c e^{-\sigma_p x}e^{-o(t)(\sigma_o-\sigma_p)x} \tag{4.2}$$

where $o(t)$ is the ortho-concentration as a function of time, and $(1 - o(t))$ is the para-concentration. From the equation above it is clear that the negative logarithm of transmission can be written as:

$$-\ln T = C + o(t)(\sigma_o - \sigma_p)x \tag{4.3}$$

where the constant C contains information on the sample and container transmission, as well as para-hydrogen cross section and sample thickness. Applying the negative logarithm to transmission data is therefore the first step in studying the time dependence of the opC.

Figure 4.15 represents the negative logarithm of the transmission for the ROIs chosen in the previous section.

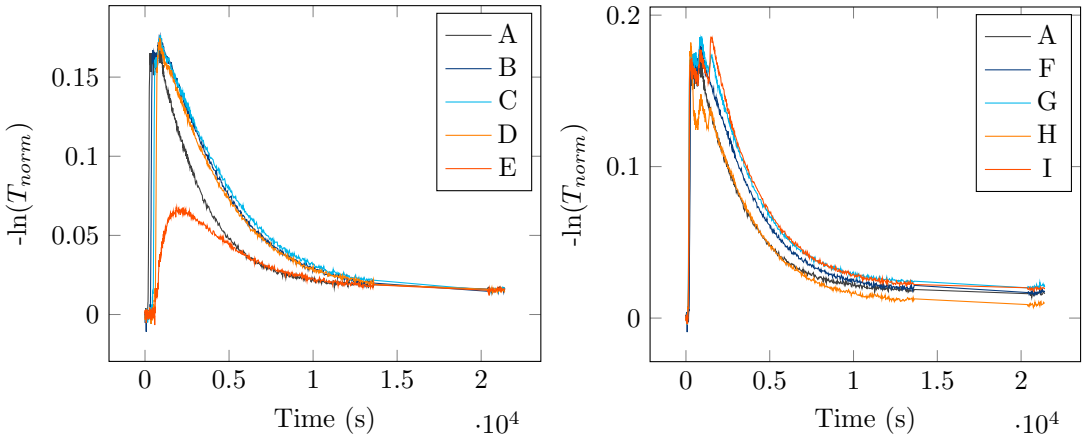

Figure 4.15: -ln(T_{norm}) is plotted as a function of time for the different ROIs chosen above.

The two plots separately show the ROIs that vary vertically and horizontally respectively. In these figures, the transmission was normalized by a constant containing information on T_M and T_c. This constant was calculated as the average transmission value of the plateaux, which can be observed at initial times of the transmission plots, before hydrogen loading. This procedure is not essential, but it

allows us to visualize data so that the initial ortho-concentration is equal to zero, as it should be since there's no hydrogen in the MOF.

In order to infer the correct time dependence of the ortho-concentration, it is necessary to fit our data. We expect to observe the trend typical of adsorbed hydrogen, reported in equation 1.21. For this reason we fit our data with the function:

$$F = Ae^{-\frac{t-t_0}{\tau}} + C \tag{4.4}$$

Where A contains the constant $[(\sigma_o - \sigma_p)x]$ as well as the initial ortho-concentration o_0, and t_0 is the time at which the conversion starts.

Fitting is performed using Mantid. In this Python-based software it is possible to fit data with a user defined function, using the command:

```
Fit(Function='name=UserFunction,Formula=A*exp(-(t-t0)/tau)+C,
A=0.108322, t0=2000,tau=2929.79,B=0.00920422,ties=(t0=2000)',
InputWorkspace='lnT_tot_17K_X'+str(x)+'_Y'+str(y),
Output='lnT_tot_17K_X'+str(x)+'_Y'+str(y), OutputCompositeMembers
=True, StartX=x0, EndX=21301, Normalise=True)
```

where we provided the formula, as well as the initial guess for each parameter. We chose to fix the value of $t_0 = 2000$ ($\simeq$ 33 min). This fixed parameter was selected in order to accommodate each curve, taking into account that the conversion starts at slightly different times in each ROI, depending on the depth within the sample. Fitting range is therefore t=2000-21301 s ($\simeq$ 33-355 min), except for ROI E, which is fitted in the interval t=3500-21301 s ($\simeq$ 58-355 min).

To calculate errors for the parameters A, B and τ, we firstly need to estimate transmission errors. ImageJ allows the user to calculate the mean value and the corresponding standard deviation of pixels, in a selected area. Doing this over 50×50 ROIs, in different slices, it is possible to notice that the standard deviation is on average equal to 2% of the corresponding transmission value. Taking into account other possible errors due to the instrument setup, we estimated the transmission error to be equal to 5% the corresponding value ($\Delta T = 0.05\ T$). Errors of the quantity $(-\ln(T))$ can be computed by error propagation as:

$$d(-\ln(T)) = \left|\frac{d(-\ln(T)}{dT}\right| \Delta T = \frac{1}{T} 0.05T = 0.05 \tag{4.5}$$

Knowing this, Mantid is able to calculate the errors of the fitted parameters, which are reported in table 4.1 together with their corresponding value.

Table 4.1: Fitting parameters obtained for each ROI.

ROI	τ	A	B
A	2573 ± 573	0.100 ± 0.009	0.017 ± 0.004
B	3812 ± 676	0.134 ± 0.008	0.013 ± 0.006
C	4155 ± 749	0.135 ± 0.008	0.012 ± 0.007
D	3807 ± 709	0.127 ± 0.008	0.013 ± 0.006
E	3796 ± 2415	0.063 ± 0.01	0.015± 0.008
F	2916 ± 533	0.123 ± 0.008	0.016 ± 0.005
G	2868 ± 488	0.132 ± 0.008	0.020 ± 0.005
H	2929 ± 610	0.108 ± 0.008	0.009 ± 0.005
I	2880 ± 459	0.141± 0.008	0.019 ± 0.005

Apart for the specific case of ROI E, the relative uncertainty of the characteristic conversion time of each ROI is around 20 % of the corresponding value.

4.4.3 Spatial distribution

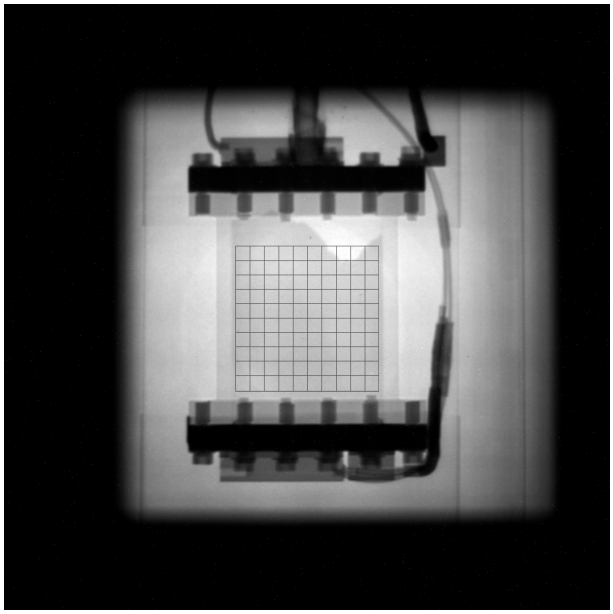

Figure 4.16: Radiograph of the sample container loaded with HKUST-1 and liquid H_2, a grid is overlaid to represent the different ROIs for which the conversion time (τ) is calculated.

The next step in this study was to investigate the spatial distribution of this phenomena. We chose to sample the radiographs in a 10 × 10 grid, where each

ROI still has a dimension of 50×50 pixels. Data acquisition was automated using ImageJ macros, specifically using a program reported in appendix C. The grid is represented in figure 4.16, here it was overlaid on a sample image, in order to show the different ROIs for which the conversion time is calculated.

Mantid analysis was also implemented for the grid, and is reported in appendix D. In figure 4.17a we report values for the characteristic conversion time in each ROI of the grid, represented by a color map.

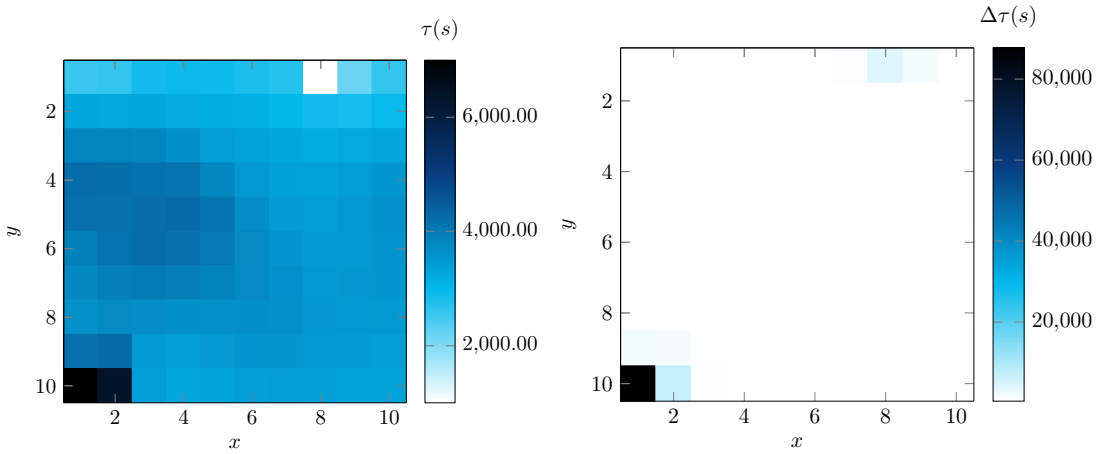

Figure 4.17: Color map of the values of τ (a), and its error (b).

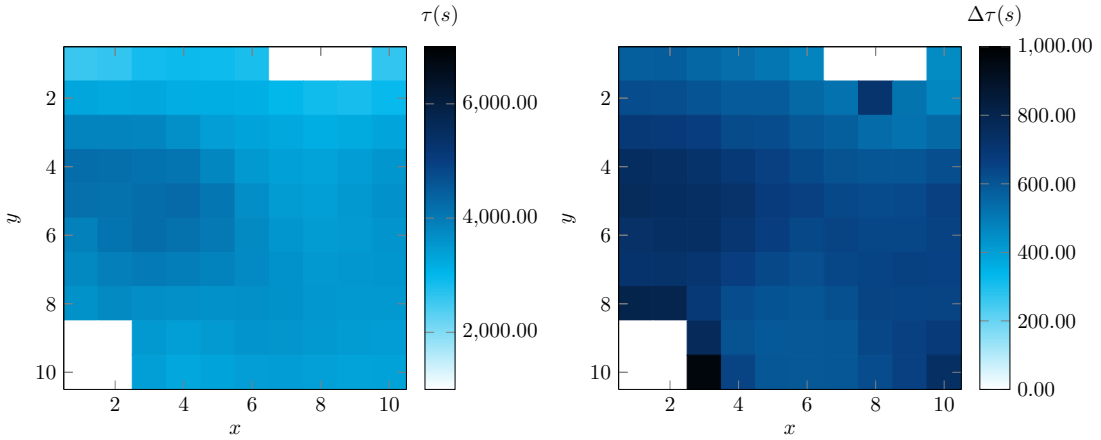

Figure 4.18: Color map of the values of τ (a), and its error (b), obtained by removing outliers.

Figure 4.17a shows their corresponding errors. From both the τ values and their errors in the color maps, it is possible to notice some outliers. In the top

right corner outliers are due to the fact that data is acquired where there is no powder. This can be easily seen from figure 4.16. In the bottom left corners outliers portray an area where hydrogen failed to reach.

Removing the outliers, the color maps are easier to interpret (see figure 4.18). Observing the color map in figure 4.18a, it is possible to notice that the value of τ seems to vary systematically in the central area. However, the error color map in 4.18b shows that this systematic increment in the values of τ corresponds to a systematic increment in their error. This can therefore be explained as a consequence of fitting, that we consider uncorrelated with physical phenomena. Except for this systematic error, the distribution of the values of τ, reported in figure 4.19, seems to be consistent with a normal distribution.

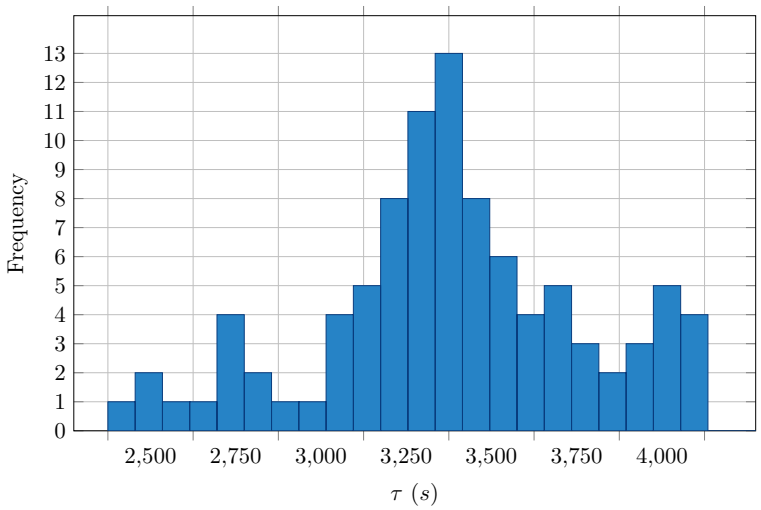

Figure 4.19: Histogram of the values of τ.

The value of the characteristic conversion time was calculated for many ROIs, therefore it is now possible to calculate their average and standard deviation, and confront the latter with experimental errors.

In figure 4.20 the rows of the grid are shown. Each point corresponds to a ROI in the grid, with its error bar. The mean value of τ is represented as a black line. The orange lines represent the error given by one standard deviation.

The mean value of τ obtained by excluding the outliers gives a characteristic conversion time equals to 3512 s, with a standard deviation of 393 s. Therefore we can conclude that:

$$\tau = 58 \pm 6 \text{ minutes} \tag{4.6}$$

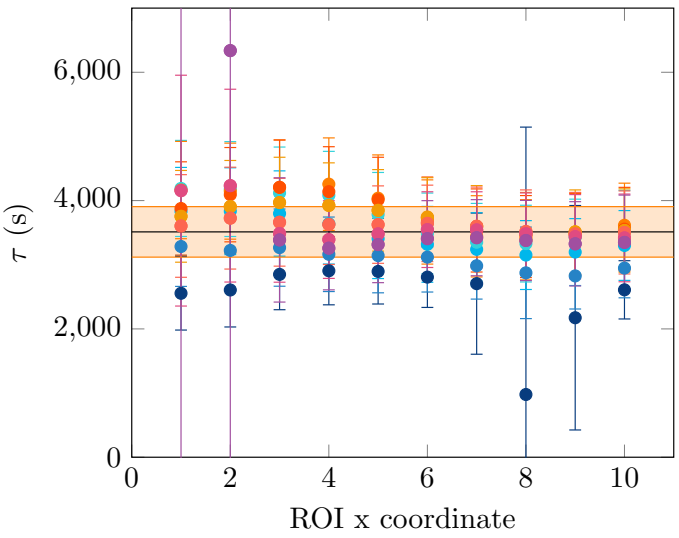

Figure 4.20: Values of τ represented for different rows, as a function of the x coordinate of the ROI.

This result is 80 times smaller compared to that of the free hydrogen, which is coherent with results obtained for other catalysts. As an example Romanelli et al. report a characteristic conversion time of ca. 100 min [38].

4.5 Neutron transmission for ortho- and para- cross sections

Neutron transmission data were acquired at the VESUVIO beamline of the ISIS neutron and muon source. The purpose of this experiment was to measure the adsorbed dihydrogen scattering cross section at 30 K, as a function of the incident neutron energy, in order to establish if they differ from those of the 3D rotor, as we would expect for this type of material.

4.5.1 Data analysis

Transmission data of the MOF containing H_2 were acquired for three different hydrogen concentrations, as a function of incident neutron energy. Each of the three measurements is composed of multiple runs, that we summed in order to obtain an average spectrum with high S/N ratio. Since at a temperature of 30 K molecular hydrogen undergoes the opC, we need to make sure that there's no kinetics

involved before averaging the measurements, so that we obtain the cross section of the system at equilibrium. Knowing the characteristic conversion time obtained in the previous section, we are able to discard the first three measurements, during which the conversion is still tacking place.

In order to perform background noise corrections flatfield data were also acquired. Both H_2 data and flatfield data were normalized by the number of counts of the incoming beam, also as a function of the incident neutron energy, in order to take into account the variability of the neutron source flux.

In contrast to the imaging setup, here the sample is smaller, has fixed thickness in every point and the powder can not move around as much, therefore it makes sense to acquire flatfield data of the CCR containing the MOF. This allows us to subtract both the MOF and sample container contribution to the cross section. To do so we divide the normalized H_2 data by the normalized flatfield data using Mantid.

Finally, just like for the imaging data, we perform the negative logarithm of transmission, in order to take into account the Beer-Lambert law (equation 2.6). In this case, we assume the concentration of ortho- and para-hydrogen to be fixed, as well as the sample thickness. This means that they only contribute as an offset to the scattering cross section.

4.5.2 Neutron scattering cross section of adsorbed hydrogen

After processing, we are able to plot the experimental scattering cross sections as a function of energy, for hydrogen adsorbed by HKUST-1. Figure 4.21 portraits the three different runs with their experimental error. These errors are estimated from the ToF dependent beamcounts assuming they reproduce a Poisson distribution. It is interesting to notice that the error bars are smaller in the central region, this is due to the H_2O moderator, which thermalizes neutrons so that the their distribution has a peak around $\frac{3}{2}K_BT$.

The shape of the cross sections as a function of energy appears to be consistent in each run. The difference between the three measurements is due to the different hydrogen concentrations. It is possible to prove this by comparing their average value at high energies, which correspond to the limit of σ_f. In fact, the three runs tend to values of 0.021 ± 0.003, 0.017 ± 0.003 and 0.032 ± 0.004 respectively. These values were obtained averaging the data at energies higher than 10^3 meV, and their errors are estimated with the respective standard deviations. It is possible to show that their ratios correspond within the error to the ratios of their

concentrations. In fact the ratio between run 1 and run 2, which is 1:1.3=0.77 corresponds to a measured ratio of 0.8 ± 0.2, similarly the ratio 1.3:2=0.65 corresponds to the measured ratio 0.6 ± 0.2 and 1:2=0.5 corresponds to 0.5 ± 0.2. Here each error was estimated by propagating the two standard deviations associated with each average value.

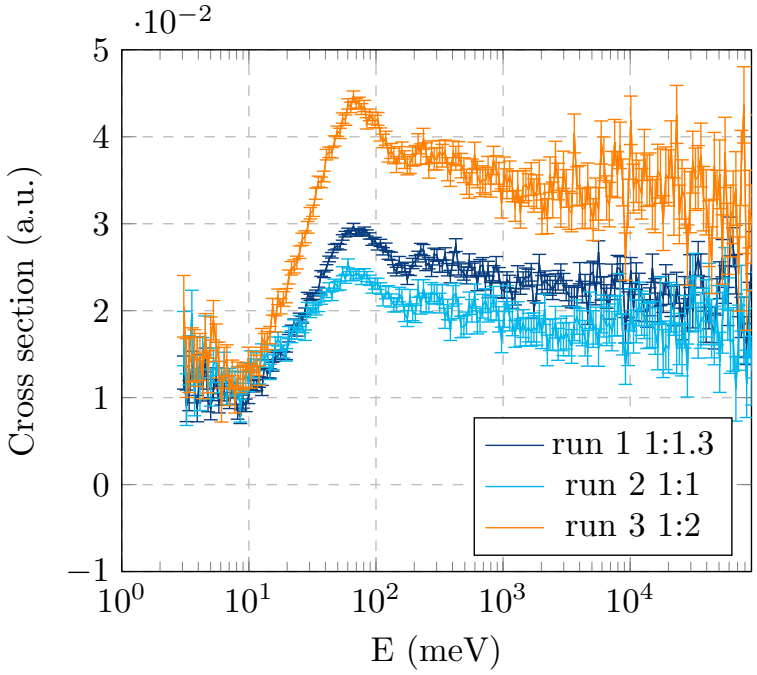

Figure 4.21: Experimental scattering cross sections of hydrogen adsorbed by HKUST-1, reported for different H_2 to Cu ratios.

To better compare the three experimental cross sections, they can be scaled so that average experimental σ_f of each run corresponds to a common value, which is the σ_f of theoretical calculations. In figure 4.23 the scaled measurements are compared with theoretical cross sections. The ortho- and para- theoretical cross sections were calculated using the Young and Koppel equations reported in chapter 3 [52], which describe the case of the 3D rotor.

The total scattering cross section can be calculated by linear combination of the ortho- and para- cross sections, weighted with their concentrations. In figure 4.22 are reported the ortho- and para- concentrations for four hindering strengths as a function of temperature, for which we had to ensure convergence. Using these partition functions the concentrations were calculated at 30 K for each hindering strength. The values of the concentrations at 30 K are reported in table 4.2.

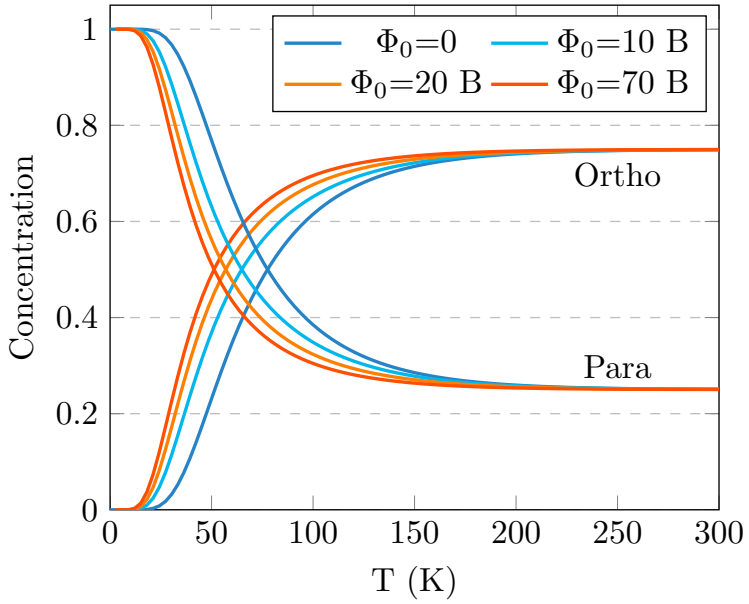

Figure 4.22: Ortho- and para- concentrations as a function of temperature for four different hindering strengths, the case of Φ_0=0 corresponds to the three dimensional case.

Table 4.2: Ortho- and para- concentrations calculated using the partition functions of ortho- and para-hydrogen, for a two dimensional rotor, for different hindering strengths, at 30 K.

Φ_0/B	pH_2 (%)	oH_2 (%)
0	97	3
10	89	11
20	83	17
70	78	22

In figure 4.23 it is possible to notice that the experimental runs do not match the 3D rotor cross section (black) in the thermal energy range. This result suggests that the adsorbed hydrogen molecules may behave as a hindered rotor. We therefore compare data to three more curves, which are labeled as $\Phi_0 = 10\ B$, $\Phi_0 = 20\ B$ and $\Phi_0 = 70\ B$. These curves are obtained using the 3D ortho- and para- cross sections, but considering concentrations that are obtained using the 2D partition function at 30 K, for each hindering strength. When comparing experimental curves to theoretical calculations, it is important to take into account that above 9 meV the energy of the incident neutrons is great enough to promote some of the para-hydrogen molecules, which at this temperature are in the lowest

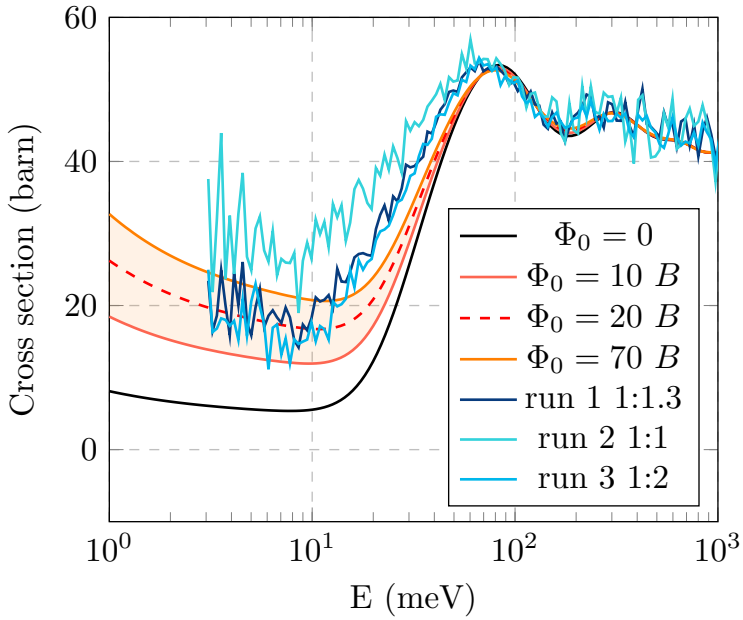

Figure 4.23: Comparison between the experimental data and theoretical calculations. The black line represents the cross section of a three dimensional rotor at 30 K. The other three theoretical cross sections are calculated by weighting the ortho- and para- 3D cross sections with concentrations obtained with a 2D partition function, as a function of the hindering strength. The dashed line represents the best fit for our data, obtained using this method.

energy state (J=0), to ortho-hydrogen (J=1). Therefore we identify as the best fit the theoretical curve that matches experimental data under 9 meV. Figure 4.23 shows that the data in runs 1 and 3 is best represented by the dashed curve, corresponding to a hindering strength of $\Phi = 20\ B$. In figure 1.5 it is possible to notice that at this strength the hindering is not particularly strong, especially at high energies. However, using the partition function, it is possible to prove that at T=30 K and $\Phi = 20\ B$ most of the molecules (83 %) are in the first energy level ($J = 0,\ m_J = 0$). The second energy level ($J = 1,\ m_J = 1$) is occupied by 17 % and the occupation percentage of the third lowest level ($J = 2,\ m_J = 2$) is of the order of 10^{-6}. The first two levels differ of 1.19 B and could therefore be associated with the behaviour of a partially hindered rotor.

The significant difference between run 2 and the other runs could be due to its lower hydrogen concentration. In fact, such a low scattering cross section could render the measurement more subject to background noise error due to the environmental γ-ray background. However this difference could also be due to

the fact that when the concentration exceeds the Cu to H_2 ratio of 1:1, hydrogen will start filling other adsorption sites, which have lower binding energies. If the binding energy is lower, the hindering strength is lower, which could explain why runs 2 and 3 are in agreement with a partially hindered rotor model.

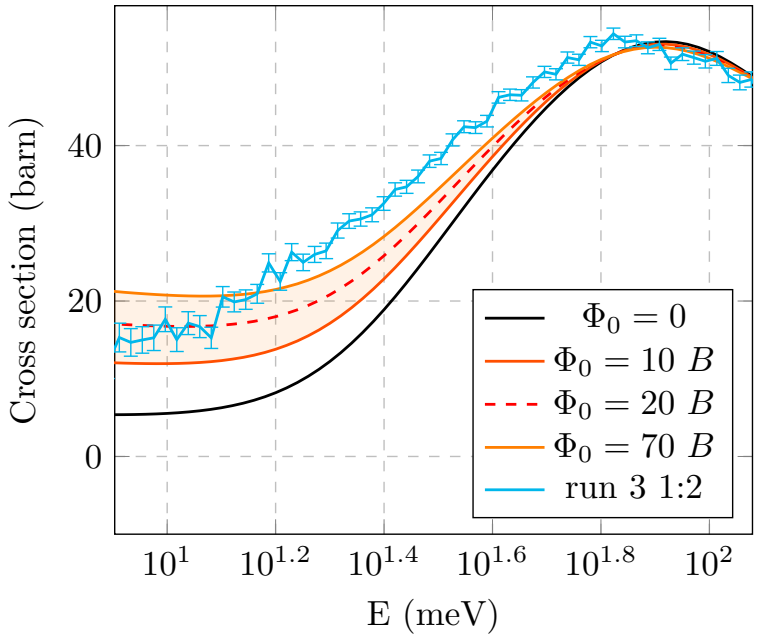

Figure 4.24: The comparison between the experimental data of run 3 and theoretical calculations of figure 4.23 is shown for the central region, in order to better visualize the difference between calculated and experimental slopes in the cross sections.

Moreover in figure 4.24 one can observe that the slope of the cross sections is not well represented by our approximation, we expect this problem to be solved by calculating the ortho- and para- cross sections of a hindered rotor. It is in fact important to stress that the ortho- and para- cross sections used to obtain these curves are calculated for a three dimensional rotor, and that the calculations for the 2D cross sections could turn out to be in agreement with a model that presents a different hindering strength.

Conclusions and outlook

Currently metal organic frameworks are attracting interest as potential hydrogen storage materials [12], rendering necessary to investigate how molecular hydrogen interacts with these complex structures.

In this work we performed neutron transmission and neutron imaging experiments on molecular hydrogen adsorbed by one particular MOF, known as HKUST-1. This MOF is particularly interesting for storage applications because of its unsaturated metal bonds.

Imaging experiments were performed ad the IMAT beamline of the ISIS neutron and muon source. Here, a time resolved imaging technique allowed us to characterize the ortho-para conversion rate as a function of time and space, for different regions of interest. We report that the ortho-hydrogen conversion rate depends linearly on the ortho-concentration, presenting an average characteristic conversion time of 58 minutes, at a temperature of 17 K. This result clearly indicates that the ortho-para conversion is catalysed by the MOF, as the free hydrogen conversion time is of ca. 79 hours [10].

Moreover we showed that the possibility to explore the spatial distribution of the sample renders imaging techniques particularly appealing for industrial and engineering applications.

Transmission experiments were performed at the VESUVIO beamline of the ISIS neutron and muon source. Here, transmission measurements were performed as a function of neutron energy using the time of flight technique.

The same MOF was observed, in order to determine the total scattering cross section of adsorbed hydrogen. Comparing it to the theoretical scattering cross section of free hydrogen we were able to show that this system is not well represented by the 3D rotor model, suggesting that a 2D rotor model might be more fit to represent adsorbed hydrogen rotational behaviour.

With a simplified approximation, we compared experimental data to a model that uses a 3D scattering cross section, weighted with 2D ortho- and para- partition

functions, showing that data are better represented assuming the presence of a hindering potential.

The next step in this line of work would be to calculate the total scattering cross section of the hindered hydrogen molecule, in order to compare it with experimental data. Moreover the experimental uncertainties due to high γ-ray background noise indicate a need to develop detectors with higher neutron efficiency and lower γ sensitivity for more reliable measurements.

Appendix A

Ortho- and para- partition functions, concentrations and heat capacities for 2D and 3D rotors

```
# -*- coding: utf-8 -*-
"""
Created on Sat May 27 13:13:34 2023

@author: margherita
"""

import numpy as np
import matplotlib.pyplot as plt

rotor = "2D"


"""H2 properties and other constants"""
M   = 2.016 # a.m.u.
re = 0.74
hbar = 2.0445 # (meV*a.m.u.)^0.5 / A-1
Kb=8.617281e-2 #meV/K
ortho=1
para=0
```

```
conversion=1.60218*6.02214/8.314462618*10 #conversion constant used to
    obtain Cv/R
T=30 # concentrations calculated at this temperature
Tmax=300
NK=5 #numero di stati rotazionali
NmJ=12 # number of eigenvalues calculated for each mJ in the input plot
B = hbar**2/(M/2.)/re**2 #meV, energy constant of rotational levels

"""Hindered rotor eigenvalues for 2D calculations"""
hindering_strength = 70 #normalized by B
filename = "hindered rotor levels m12 phi500.txt"
with open(filename, "r") as file:
           for _ in range(hindering_strength - 1):
               file.readline()
           line = file.readline().strip()
           values = line.split()
           eigenvalues= [float(el) for el in values ]

def eigenvalues2D(mJ,J):
           if mJ<=J and 2*NK<NmJ:
               e=eigenvalues[mJ*NmJ+J-mJ]
               return e
           else:
               return "mJ can not be greater than J, or your input\
           file does not have enough Js for each mJ"

def partition_function(I, temp) :
    beta = 1. / 8.617281e-2 / temp # 1/meV

    if rotor == "3D" :
        PK = np.zeros(2*NK)
        for k in range(2*NK):
            PK[k] = (2.*k+1) * np.exp(-B * k * (k+1.) * beta)
            PK[k] *= np.abs( (-1)**k + (-1)**I)/2.
        PK = PK.sum()
        return PK

    elif rotor == "2D" :
        PK = np.zeros(2*(NK**2)+NK)
```

```
        i=0
        for k in range(2*NK):
              for mk in range(0,k+1):
                  EV= eigenvalues2D(mk,k)
                  PK[i] = np.exp(-B * EV * beta)
                  if mk > 0 : PK[i] *= 2.
                  PK[i] *= np.abs( (-1)**k + (-1)**I)/2.
                  i=i+1
        PK = PK.sum()
        return PK


T_values = np.linspace(0.0001, Tmax, 100)
Ortho_concentration_3D_values =[]
Para_concentration_3D_values=[]

for t in T_values:
     Para_concentration_3D_values.append\
     (partition_function(0,t)/(partition_function(0,t)+3*partition_function(1,t)))
     Ortho_concentration_3D_values.append\
     (3*partition_function(1,t)/(partition_function(0,t)+3*partition_function(1,t)))



plt.plot(T_values, Para_concentration_3D_values)
plt.plot(T_values, Ortho_concentration_3D_values)
plt.xlabel('T')
plt.ylabel('Concentration')
plt.title('Ortho-para concentrations')
plt.show()

if rotor == "3D":
    print("The 3D Ortho concentration at temperature %g K is %g %%"\
          %(T,3*partition_function(1,T)/(partition_function(0,T)+\
          3*partition_function(1,T))*100))
    print("The 3D Para concentration at temperature %g K is %g %%"\
          %(T,partition_function(0,T)/(partition_function(0,T)+\
          3*partition_function(1,T))*100))
elif rotor =="2D":
```

```
    print("The 2D Ortho concentration at temperature %g K is %g %%"\
          %(T,3*partition_function(1,T)/(partition_function(0,T)+\
          3*partition_function(1,T))*100))
    print("The 2D Para concentration at temperature %g K is %g %%"\
          %(T,partition_function(0,T)/(partition_function(0,T)+\
          3*partition_function(1,T))*100))

def Para_Cv(temp) :
    if rotor=="3D":
        beta = 1. / Kb / temp # 1/meV
        E2avg = np.zeros(2*NK)
        Eavg = np.zeros(2*NK)
        PK=np.zeros(2*NK)
        for k in range(2*NK):
                J=2*k
                E2avg[k] = ((B*J*(J+1.))**2)*(2.*J+1.) * np.exp(-B * J *
                    (J+1.) * beta)
                Eavg[k] = B*J*(J+1.)*(2.*J+1.) * np.exp(-B * J * (J+1.) *
                    beta)
                PK[k] = (2.*J+1.) * np.exp(-B * J * (J+1.) * beta)

        E2AVG = E2avg.sum()
        EAVG = Eavg.sum()

        E2AVG /= PK.sum()
        EAVG /= PK.sum()
        EAVG2= EAVG**2
        return conversion*(E2AVG-EAVG2)/(Kb*temp**2)

    elif rotor=="2D":
        beta = 1. / Kb / temp # 1/meV
        E2avg2D = np.zeros(2*(NK**2)+NK)
        Eavg2D = np.zeros(2*(NK**2)+NK)
        PK2D = np.zeros(2*(NK**2)+NK)
        k=0
        mk=0
        i=0
        for k in range(2*NK):
              for mk in range(0,k+1):
```

```
                EV= eigenvalues2D(mk,k)

                PK2D[i] = np.exp(-B * EV * beta)
                if mk > 0 : PK2D[i] *= 2.
                PK2D[i] *= np.abs( (-1)**k + (-1)**para)/2.

                E2avg2D[i] =((EV*B)**2) * np.exp(-B * EV * beta)
                if mk > 0 : E2avg2D[i] *= 2.
                E2avg2D[i] *= np.abs( (-1)**k + (-1)**para)/2.

                Eavg2D[i] = EV*B * np.exp(-B * EV * beta)
                if mk > 0 : Eavg2D[i] *= 2.
                Eavg2D[i] *= np.abs( (-1)**k + (-1)**para)/2.

                i=i+1

        E2AVG2D = E2avg2D.sum()
        EAVG2D = Eavg2D.sum()
        E2AVG2D /= PK2D.sum()
        EAVG2D /= PK2D.sum()
        EAVG22D= EAVG2D**2
        PK2D /=PK2D.sum()
        return conversion*(E2AVG2D-EAVG22D)/(Kb*temp**2)


def Ortho_Cv(temp) :
    if rotor=="3D":
        beta = 1. / Kb / temp # 1/meV
        E2avg = np.zeros(2*NK)
        Eavg = np.zeros(2*NK)
        PK=np.zeros(2*NK)
        for k in range(2*NK):
                J=2*k+1
                E2avg[k] = ((B*J*(J+1.))**2)*(2.*J+1.) * np.exp(-B * J *
                    (J+1.) * beta)
                Eavg[k] = B*J*(J+1.)*(2.*J+1.) * np.exp(-B * J * (J+1.) *
                    beta)
                PK[k] = (2.*J+1.) * np.exp(-B * J * (J+1.) * beta)
```

```
    E2AVG = E2avg.sum()
    EAVG = Eavg.sum()

    E2AVG /= PK.sum()
    EAVG /= PK.sum()
    EAVG2= EAVG**2
    return conversion*(E2AVG-EAVG2)/(Kb*temp**2)
elif rotor=="2D":
    beta = 1. / Kb / temp # 1/meV
    E2avg2D = np.zeros(2*(NK**2)+NK)
    Eavg2D = np.zeros(2*(NK**2)+NK)
    PK2D = np.zeros(2*(NK**2)+NK)
    k=0
    mk=0
    i=0
    for k in range(2*NK):
          for mk in range(0,k+1):
              EV= eigenvalues2D(mk,k)

              PK2D[i] = np.exp(-B * EV * beta)
              if mk > 0 : PK2D[i] *= 2.
              PK2D[i] *= np.abs( (-1)**k + (-1)**ortho)/2.

              E2avg2D[i] =((EV*B)**2) * np.exp(-B * EV * beta)
              if mk > 0 : E2avg2D[i] *= 2.
              E2avg2D[i] *= np.abs( (-1)**k + (-1)**ortho)/2.

              Eavg2D[i] = EV*B * np.exp(-B * EV * beta)
              if mk > 0 : Eavg2D[i] *= 2.
              Eavg2D[i] *= np.abs( (-1)**k + (-1)**ortho)/2.

              i=i+1
    E2AVG2D = E2avg2D.sum()
    EAVG2D = Eavg2D.sum()
    E2AVG2D /= PK2D.sum()
    EAVG2D /= PK2D.sum()
    EAVG22D= EAVG2D**2
    PK2D /=PK2D.sum()
    return conversion*(E2AVG2D-EAVG22D)/(Kb*temp**2)
```

```
def Three_to_one_Cv(temp):
    EQ=(3./4.)*Ortho_Cv(temp)+(1./4.)*Para_Cv(temp)
    return EQ

def Equilibrium_Cv_3D(temp):
    beta = 1. / Kb / temp # 1/meV
    E2avg = np.zeros(2*NK)
    Eavg = np.zeros(2*NK)
    PK=np.zeros(2*NK)
    for J in range(2*NK):
        E2avg[J] = ((B*J*(J+1.))**2)*(2.*J+1.) * np.exp(-B * J * (J+1.) *
            beta)
        Eavg[J] = B*J*(J+1.)*(2.*J+1.) * np.exp(-B * J * (J+1.) * beta)
        PK[J] = (2.*J+1.) * np.exp(-B * J * (J+1.) * beta)
        if J%2!=0:
            E2avg[J] *=3
            Eavg[J] *= 3
            PK[J] *=3
    E2AVG = E2avg.sum()
    EAVG = Eavg.sum()
    E2AVG /= PK.sum()
    EAVG /= PK.sum()
    EAVG2= EAVG**2
    return conversion*(E2AVG-EAVG2)/(Kb*(temp**2))


T_values = np.linspace(0.0001, Tmax, 100)
O3_values =[]
P3_values=[]
T3_values=[]
E3_values=[]

for T in T_values:
     O3_values.append(Ortho_Cv(T))
     P3_values.append(Para_Cv(T))
     T3_values.append(Three_to_one_Cv(T))
     E3_values.append(Equilibrium_Cv_3D(T))
```

```
if rotor == "3D":

    with open("Para_Cv_3D.txt", "w") as f:
        for t, P_val in zip(T_values, P3_values):
            f.write(f"{t}\t{P_val}\n")

    with open("Ortho_Cv_3D.txt", "w") as f:
        for t, P_val in zip(T_values, O3_values):
            f.write(f"{t}\t{P_val}\n")

    with open("Three_to_one_Cv_3D.txt", "w") as f:
        for t, P_val in zip(T_values, T3_values):
            f.write(f"{t}\t{P_val}\n")

    with open("Equilibrium_Cv_3D.txt", "w") as f:
        for t, P_val in zip(T_values, E3_values):
            f.write(f"{t}\t{P_val}\n")
elif rotor == "2D":
    with open("Para_Cv_2D.txt", "w") as f:
        for t, P_val in zip(T_values, P3_values):
            f.write(f"{t}\t{P_val}\n")

    with open("Ortho_Cv_2D.txt", "w") as f:
        for t, P_val in zip(T_values, O3_values):
            f.write(f"{t}\t{P_val}\n")
    with open("Three_to_one_Cv_2D.txt", "w") as f:
        for t, P_val in zip(T_values, T3_values):
            f.write(f"{t}\t{P_val}\n")

if rotor =="3D":
    plt.plot(T_values, O3_values)
    plt.plot(T_values, P3_values)
    plt.plot(T_values, T3_values)
    plt.plot(T_values, E3_values)
    plt.xlabel('T')
    plt.ylabel('Rotational Cv/R')
    plt.show()
elif rotor== "2D":
```

```
plt.plot(T_values, O3_values)
plt.plot(T_values, P3_values)
plt.plot(T_values, T3_values)
plt.xlabel('T')
plt.ylabel('Rotational Cv/R')
plt.show()
```

Appendix B

Background noise corrections

B.1 Normalization correction

```
    open("/home/s1123564/Desktop/Empty_CCR_10K/CCR_5s_PH40")

imageCalculator("Subtract create stack", "CCR_5s_PH40","AVG_Darks_5s");
selectWindow("Result of CCR_5s_PH40");

Table.open("/home/s1123564/Desktop/Empty_CCR_10K/Timestamp_vs_Beamcount_
    IMAT00018309_Empty_CCR_10KCCR_5s_PH40_log.txt");

m=0;
for (i = 1; i <= nSlices; i++) {
    setSlice(i);
    counts=parseFloat(Table.get("counts", i-1));
    m=m+counts;
}
media=m/nSlices;
for (i = 1; i <= nSlices; i++) { //loop per normalizzare
    setSlice(i);
    counts=parseFloat(Table.get("counts", i-1));
    val=counts/media; //?????????
    run("Divide...", "value="+val+" slice");
}
```

```
run("Grouped Z Project...", "projection=[Average Intensity]
    group="+nSlices);
selectWindow("CCR_5s_PH40");
close();
```

B.2 Standard deviation correction

```
    open("/home/s1123564/Desktop/Empty_CCR_10K/CCR_5s_PH40")

imageCalculator("Subtract create stack", "CCR_5s_PH40","AVG_Darks_5s");
selectWindow("Result of CCR_5s_PH40");

Table.open("/home/s1123564/Desktop/Empty_CCR_10K
/Timestamp_vs_Beamcount_IMAT00018309_Empty_CCR_10KCCR_5s_PH40_log.txt");

m=0;
for (i = 1; i <= nSlices; i++) {
    setSlice(i);
    counts=parseFloat(Table.get("counts", i-1));
    m=m+counts;
}
media=m/nSlices;
SD=0

for (i = 1; i <= nSlices; i++) {
    setSlice(i);
    counts=parseFloat(Table.get("counts", i-1));
    SD=SD+Math.sqr(counts-media);
}
StanDev=sqrt(SD/nSlices);

for (i = 1; i <= nSlices; i++) { //loop per normalizzare
    //setSlice(i);
    counts=parseFloat(Table.get("counts", i-1));
    if (counts>media+StanDev) {
      run("Slice Remover", "first="+i+" last="+i+" increment=1");
    }
```

```
    if (counts<media-StanDev) {
      run("Slice Remover", "first="+i+" last="+i+" increment=1");
    }
}

run("Grouped Z Project...", "projection=[Average Intensity]
    group="+nSlices);
selectWindow("CCR_5s_PH40");
close();
```

B.3 Total background corrections

```
////////////////////////////////////////////////////////////////////
////////////////////////////// DARKS ///////////////////////////////
////////////////////////////////////////////////////////////////////
                    //////// open stack ////////
open("/home/s1123564/Desktop/MOF_Darks/Darks_5s") //??no conteggi da norm
                ///////////////////////////////////
run("Median 3D...", "x=2 y=2 z=2");
//run("Gaussian Blur...", "sigma=4 stack");
//run("Remove Outliers", "block_radius_x=40 block_radius_y=40
    standard_deviations=3 stack");

run("Grouped Z Project...", "projection=[Average Intensity]
    group="+nSlices);

selectWindow("Darks_5s");
close();
////////////////////////////////////////////////////////////////////
////////////////////////////// EMPTY CCR ///////////////////////////
////////////////////////////////////////////////////////////////////
                  //////// open stack ////////
open("/home/s1123564/Desktop/Empty_CCR_10K/CCR_5s_PH40")
                  ////////////////////////////
imageCalculator("Subtract create stack", "CCR_5s_PH40","AVG_Darks_5s");
selectWindow("Result of CCR_5s_PH40");
                ///////// open .txt table ////////
```

```
Table.open("/home/s1123564/Desktop/Empty_CCR_10K/Timestamp_vs_Beamcount_
IMAT00018309_Empty_CCR_10KCCR_5s_PH40_log.txt");
              ////////////////////////////////////
m=0;
for (i = 1; i <= nSlices; i++) {
    setSlice(i);
    counts=parseFloat(Table.get("counts", i-1));
    m=m+counts;
}
media=m/nSlices;
SD=0

for (i = 1; i <= nSlices; i++) {
    setSlice(i);
    counts=parseFloat(Table.get("counts", i-1));
    SD=SD+Math.sqr(counts-media);
}
StanDev=sqrt(SD/nSlices);

for (i = 1; i <= nSlices; i++) { //loop per normalizzare
    //setSlice(i);
    counts=parseFloat(Table.get("counts", i-1));
    if (counts>media+StanDev) {
      run("Slice Remover", "first="+i+" last="+i+" increment=1");
    }
    if (counts<media-StanDev) {
      run("Slice Remover", "first="+i+" last="+i+" increment=1");
    }
}

selectWindow("Result of CCR_5s_PH40");
run("32-bit");

for (i = 1; i <= nSlices; i++) {
    setSlice(i);
    makeRectangle(1548, 384, 188, 1300);
    run("Measure");
    MediaPixel=parseFloat(Table.get("Mean", i-1));
    makeRectangle(0, 0, 2048, 2048);
```

```
    run("Divide...", "value="+MediaPixel+" slice");
}

run("Grouped Z Project...", "projection=[Average Intensity]
    group="+nSlices);
selectWindow("CCR_5s_PH40");
close();
////////////////////////////////////////////////////////////////////
//////////////////// MOF_17K Corrected ////////////////////
////////////////////////////////////////////////////////////////////

open("/home/s1123564/Desktop/MOF_17K/H2liq_5s_PH40")
    imageCalculator("Subtract create stack",
    "H2liq_5s_PH40","AVG_Darks_5s");
selectWindow("Result of H2liq_5s_PH40");
run("32-bit");
selectWindow("AVG_Result of CCR_5s_PH40");
run("32-bit");
imageCalculator("Divide create stack", "Result of
    H2liq_5s_PH40","AVG_Result of CCR_5s_PH40");


selectWindow("Result of Result of H2liq_5s_PH40");
run("32-bit");

for (i = 1; i <= nSlices; i++) {
    setSlice(i);
    makeRectangle(1548, 384, 188, 1300);
    run("Measure");
    MediaPixel=parseFloat(Table.get("Mean", i-1));
    makeRectangle(0, 0, 2048, 2048);
    run("Divide...", "value="+MediaPixel+" slice");
}
////////////////////////////////////////////////////////////////////
////////////////////////////// plot ////////////////////////////////
////////////////////////////////////////////////////////////////////
selectWindow("Result of Result of H2liq_5s_PH40");
makeRectangle(824, 924, 408, 260);
run("Plot Z-axis Profile");
```

Appendix C

Sampling characteristic conversion time in a grid

```
///makeRectangle(800, 800,400, 400); ///////// griglia 8x8
///makeRectangle(775, 800,500, 500); ///////// griglia 10x10
//5s
open("/home/s1123564/Desktop/MOF_17K/Result of Result of
    H2liq_5s_PH40_17K.tif");
//15s
open("/home/s1123564/Desktop/MOF_17K/Result of Result of
    H2liq_15s_PH40_17K.tif");
//30s
open("/home/s1123564/Desktop/MOF_17K/Result of Result of
    H2liq_30s_PH40_17K.tif");
Table.open("/home/s1123564/Desktop/MOF_17K/Timestamp_tot_17K.txt");
timestamp=Table.getColumn("timestamp");
//normalizzare per il plateaux (?)
elements5s=150; //numero elementi nella prima stack
elements15s=100; //numero elementi seconda stack
err=0.05; //errore del 5%
xgriglia=8; //nxm elementi = griglia number
ygriglia=8;
celldim=50; //larghezza elemento della griglia 50x50
xpixel=800; //fino a 1200

for (X = 1; X < xgriglia+1; X++) { //contatore che corre sulla griglia
    lungo X
```

```
   ypixel=800; //fino a 1200
   for (Y = 1; Y < ygriglia+1; Y++) {//contatore che corre sulla griglia
       lungo Y
      str = "";
      selectWindow("Result of Result of H2liq_5s_PH40_17K.tif");
      makeRectangle(xpixel, ypixel, 50, 50);
      run("Plot Z-axis Profile");
      Plot.getValues(x5, y5);
         for ( i5 = 0; i5 < x5.length; i5++ ) {
            lnT=-log(parseFloat(y5[i5]));
            str += "" + timestamp[i5] + "\t" + lnT + "\t" + err + "\n"; }

      selectWindow("Result of Result of H2liq_15s_PH40_17K.tif");
       makeRectangle(xpixel, ypixel, 50, 50);
       run("Plot Z-axis Profile");
       Plot.getValues(x15, y15);
         for ( i15 = 0; i15 < x15.length; i15++ ) {
            lnT=-log(parseFloat(y15[i15]));
            str += "" + timestamp[i15+elements5s] + "\t" + lnT + "\t" +
                err + "\n"; }

      selectWindow("Result of Result of H2liq_30s_PH40_17K.tif");
      makeRectangle(xpixel, ypixel, 50, 50);
      run("Plot Z-axis Profile");
      Plot.getValues(x30, y30);
         for ( i30 = 0; i30 < x30.length; i30++ ) {
            lnT=-log(parseFloat(y30[i30]));
            str += "" + timestamp[i30+elements5s+elements15s] + "\t" +
                lnT + "\t" + err + "\n"; }

      File.saveString( str, "/home/s1123564/Desktop/MOF_17K
          /griglia_lnT_17K/lnT_tot_17K_X"+X+"_Y"+Y+".txt" );
      ypixel=ypixel+celldim;
   }
   xpixel=xpixel+celldim;
}
close("*");
```

Appendix D

Mantid analysis of the grid

```
# import mantid algorithms, numpy and matplotlib
from mantid.simpleapi import *
import matplotlib.pyplot as plt
import numpy as np

Tau=[]
A=[]
B=[]
x0=2000 # legato al valore iniziale!!!!
gxg=10 #elementi della griglia, es griglia di dimensioni 8x8
#file griglia
g= open("/Users/margherita/Desktop/Tesi magistrale//Dati
    H2/MOF_17K/griglia_10x10_lnT_17K/griglia_10x10_tau_17K.txt","w+")

GridErr= open("/Users/margherita/Desktop/Tesi magistrale/Dati \
H2/MOF_17K/griglia_10x10_lnT_17K/errori_griglia_10x10_tau_17K.txt","w+")

GridErrpgf= open("/Users/margherita/Desktop/Tesi magistrale/Dati\
H2/MOF_17K/griglia_10x10_lnT_17K/pgfplot_errori_griglia_10x10_tau_17K.txt","w+")

pgf=open("/Users/margherita/Desktop/Tesi magistrale/Dati \
H2/MOF_17K/griglia_10x10_lnT_17K/pgfplot_griglia_10x10_tau_17K.txt","w+")

mpi=open("/Users/margherita/Desktop/Tesi magistrale/Dati \
H2/MOF_17K/griglia_10x10_lnT_17K/media_plateaux_tau_17K.txt","w+")
```

```
#media punti iniziali
n=20 #numero di punti del plateaux su cui faccio la media
y=1
for y in range(1,gxg+1):
    x=1
    for x in range(1,gxg+1):
        Load(Filename='C:/Users/margherita/Desktop/Tesi magistrale/Dati
            H2/MOF_17K/griglia_10x10_lnT_17K\
        /lnT_tot_17K_X'+str(x)+'_Y'+str(y)+'.txt', \
        OutputWorkspace='lnT_tot_17K_X'+str(x)+'_Y'+str(y))

        Fit(Function='name=UserFunction,Formula=A*exp(-(x-x0)/tau)+B,A=0.108322,
            x0='+str(x0)+',tau=2929.79,B=0.00920422,ties=(x0='+str(x0)+')',
        InputWorkspace='lnT_tot_17K_X'+str(x)+'_Y'+str(y),
            Output='lnT_tot_17K_X'+str(x)+'_Y'+str(y),
            OutputCompositeMembers=True, StartX=x0,
            EndX=21301.955000000002, Normalise=True)
        with open('C:/Users/margherita/Desktop/Tesi \
        magistrale/Dati H2/MOF_17K/griglia_10x10_lnT_17K\
        /lnT_tot_17K_X'+str(x)+'_Y'+str(y)+'.txt', 'r') as f:
            values=[]
            for i, line in enumerate(f):
                if i >= n:
                    break
                values.append(float(line.split()[1]))
        m=0
        for M in range(0,n):
            m=m+values[M]
        Mpi=m/n
        mpi.write("%g \n" %(Mpi))
        ws=mtd['lnT_tot_17K_X'+str(x)+'_Y'+str(y)+'_Parameters']
        a=ws.cell(0,1)
        tau=ws.cell(2,1)
        errtau=ws.cell(2,2)
        b=ws.cell(3,1)
        g.write("%g \t" %(tau))
        GridErr.write("%g \t" %(errtau))
        pgf.write("%g \t %g \t %g \n" %(x, y, tau))
        GridErrpgf.write("%g \t %g \t %g \n" %(x, y, errtau))
```

```
        Tau.append(tau)
        A.append(a)
        B.append(b)
        x=x+1
    g.write("\n")
    GridErr.write("\n")
    pgf.write("\n")
    mpi.write("\n")
    GridErrpgf.write("\n")
    y=y+1

GridErrpgf.close()
GridErr.close()
pgf.close()
g.close()
mpi.close()
```

Appendix E

Average Functional Group Approximation for the neutron thermal cross section of organic polymers

In the framework of neutron thermal scattering cross sections of hydrogen-rich materials, I personally had the chance to employ the Average functional group approximation (AFGA) to calculate the scattering cross section of thermoplastic polymers, contributing to the publication of [60].

The AFGA approach is based on the fact that hydrogen greatly contributes to the thermal scattering cross section of organic materials. In fact, as mentioned in chapter 3, hydrogen contribution to the incoherent cross section of a polymer is particularly significant because its mass is close to that of neutrons, therefore exchanging a higher amount of energy compared to any other atom. Moreover an incoherent approximation is particularly suitable to describe hydrogen rich materials (such as polymers), because of the great difference between coherent and incoherent hydrogen cross sections (see table 3.1). For these reasons it is possible to rationalize a polymer as composed of hydrogen atoms, that belong to specific functional groups. The average functional group approximation (AFGA) [61] consists of approximating the total incoherent scattering cross section of a polymer using the contribution of each functional group that composes the polymer. The purpose of this approximation is to provide a simplified and phenomenological method to estimate the thermal neutron cross section of polymers and organic molecules, that could render unnecessary more complex atomistic simulations. It is also important

Table E.1: Rationalisation of organic polymers based on their hydrogen-containing functional groups. The density and molecular mass per formula unit for each material are also reported.

Material	Formula	CH_3	CH_2	CH_{ali}	Other	Mass (a.m.u.)	Density (g/cm^3)
Polylactic acid	$(C_3H_4O_2)_n$	1	–	1	–	72.06	1.43
Polycarbonate	$(C_{16}H_{14}O_4)_n$	2	–	–	$8CH_{aro}$	272.29	1.20
Polypropylene	$(C_3H_6)_n$	1	1	1	–	42.08	0.90
Acrylonitrile	$(C_3H_3N)_n$	–	1	1	–	53.06	0.81
Butadiene	$(C_4H_6)_n$	–	2	2	–	54.09	0.61
Styrene	$(C_8H_8)_n$	–	1	1	$5CH_{aro}$	104.15	0.91
PAPP	$(C_4H_{10}N_2H_4O_7P_2)_n$	–	4	–	$2OH$, $2NH_2$	264.11	1.50

to notice that experimental data of thermal neutron cross sections are not available for many materials, thus rendering this approximation particularly useful in the analysis of complex compounds. AFGA can therefore be implemented when designing nuclear reactor components, neutron moderators or shielding materials, in order to compare different recipes and predict how the neutrons interact with them. Moreover it could be employed for the transport codes used in neutron capture therapy to simulate neutron interaction with different organs and tissues.

AFGA can also be employed to simulate the thermal neutron cross section of materials used for 3D printing, in order to easily investigate 3D-printed instrument components. It is possible to identify a great number of different materials for 3D printing, since monomers and polymer chains can be combined with different stoichiometries. This field is therefore a good example of how AFGA can provide a game-changing approach. AFGA calculations of the scattering cross sections run within the NCrystal environment [62], and are based on the formalism reported in [61].

Table E.1 reports the rationalization of multiple polymers based on their functional groups. NCrystal already features some of these polymers, therefore we mainly focus on three polymers that are the main constituents for ABS: acrylonitrile, butadiene, and styrene. ABS is a common thermoplastic polymer for which is possible to identify multiple possible recipes by varying the proportions between its three main constituents. Specifically we considered one of its most common forms, reported in [63]: 7.1 wt% acrylonitrile, 12.9 wt% butadiene, and 80 wt% styrene.

As an example we show the code used to obtain the cross section of a specific polymer (acrylonitrile) from NCrystal using the average functional group approximation.

```
# create material in NCrystal
```

```
# using the AFGA model
!ncrystal_hfg2ncmat --formula C3H3N
                    --spec 1xCHali+1xCH2
                    --density 0.81
                    --title acrylonitrile
                    -o acrylonitrile.ncmat
T = '300K' # Temperature in K
fn = 'acrylonitrile.ncmat;temp='+T
pc = NC.createScatter(fn)
# calculate absorption cross section
absorption = NC.createAbsorption(fn)
xs_abs = absorption.crossSectionNonOriented(E)
# calculate scattering cross section
xs = pc.crossSectionNonOriented(E)
```

With the AFGA method we are able to calculate the total scattering cross section per formula unit, as well as the linear scattering attenuation factor per mass unit, an therefore transmission implementing the Beer-Lambert law. It should be noted that within the AFGA approach it is possible to calculate the attenuation coefficient as a linear combination of the coefficients of the constituents polymers.

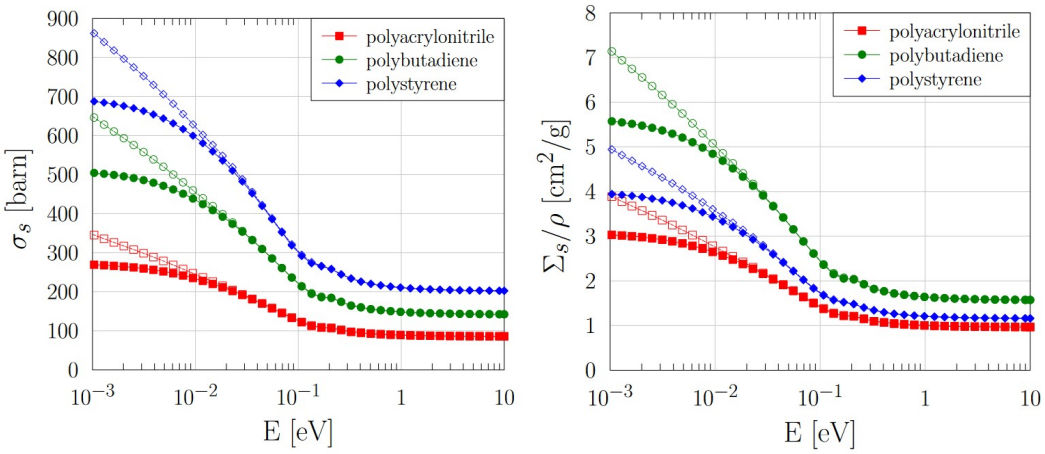

Figure E.1: The total scattering cross section per monomer unit (top) and mass attenuation coefficient (bottom) for the acrylonitrile (red squares), butadine (green circles) and styrene (blue diamonds) polymers. The reported spectra take into account scattering contributions only (absorption cross sections not included). Filled and empty markers refer to 10 K and 300 K, respectively.

Moreover we extended the calculations to the specific case presented in [63], where ABS was mixed with the flame-retardant compound known as piperazine pyrophosphate (PAPP).

Figure E.2 shows a comparison between the mass attenuation coefficients of ABS, PAPP and a co-polymer made of 25 wt% PAPP and 75 wt% ABS, as well as the main constituent polymer of ABS.

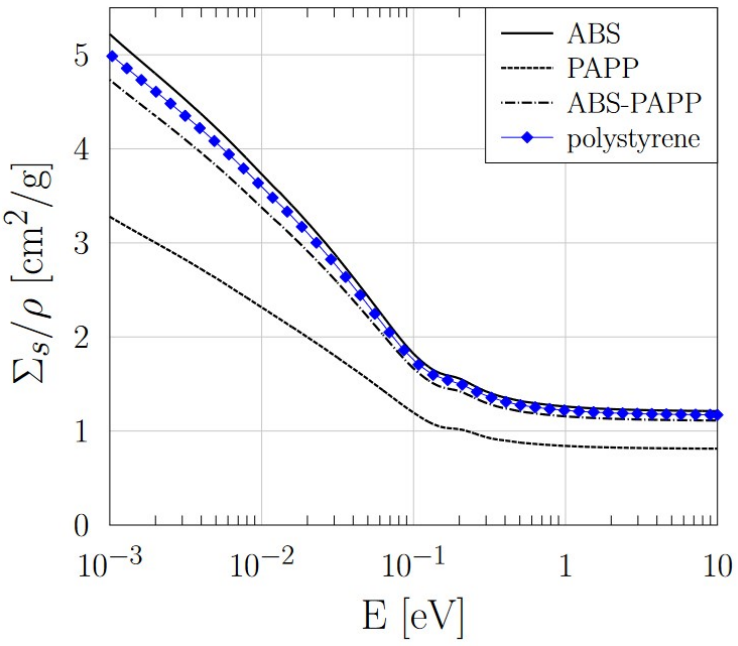

Figure E.2: The mass attenuation coefficient for the polymer ABS based on the recipe from Ref.[**?**], compared with the one for polystyrene (blue triangles). The mass attenuation coefficient for PAPP and a mixture of ABS and PAPP are also reported as dashed and dotted-dashed lines, respectively.

The publication of these results in [60] provided a worked example that shows how to implement the average functional group approximation, while also proving its potential in the field of polymer compounds characterization.

Bibliography

[1] Sebastian Eisenhut, Marcel Klaus, Johannes Baggemann, Ulrich Rücker, Y. Beßler, Alexander Schwab, Christoph Haberstroh, Tobias Cronert, Thomas Gutberlet, Thomas Brückel, and Carsten Lange. Cryostat for the provision of liquid hydrogen with a variable ortho-para ratio for a low-dimensional cold neutron moderator. *EPJ Web of Conferences*, 231:04001, 01 2020.

[2] Isaac F. Silvera and Mourits Nielsen. Inelastic neutron scattering and separation coefficient of absorbed hydrogen: Molecular alignment and energy levels. *Phys. Rev. Lett.*, 37:1275–1278, Nov 1976.

[3] Isaac F. Silvera. The solid molecular hydrogens in the condensed phase: Fundamentals and static properties. *Rev. Mod. Phys.*, 52:393–452, Apr 1980.

[4] Isaac F Silvera. The solid molecular hydrogens in the condensed phase: Fundamentals and static properties. *Reviews of Modern Physics*, 52(2):393, 1980.

[5] L. Abouaf-Marguin and A.-M. Vasserot. Nuclear spin conversion of O2 doped solid normal H2 at 4.2k: An empirical law to determine the ortho-H2 concentration by infrared absorption spectroscopy. *Chemical Physics Letters*, 460(1):82–85, 2008.

[6] Liese-Marie Sutherland, J. Knudson, Michal Mocko, and Richard Renneke. Practical in-situ determination of ortho-para hydrogen ratios via fiber-optic based raman spectroscopy. *Nuclear Instruments and Methods in Physics Research Section A Accelerators Spectrometers Detectors and Associated Equipment*, 810:182–185, 02 2016.

[7] A Stewart and G Squires. Analysis of ortho- and para-hydrogen mixtures by the thermal conductivity method. *Journal of Scientific Instruments*, 32:26, 12 2002.

[8] Mitsuru Matsumoto and James H. Espenson. Kinetics of the interconversion of parahydrogen and orthohydrogen catalyzed by paramagnetic complex ions. *Journal of the American Chemical Society*, 127 32:11447–53, 2005.

[9] W U Notardonato, A M Swanger, J E Fesmire, K M Jumper, W L Johnson, and T M Tomsik. Zero boil-off methods for large-scale liquid hydrogen tanks using integrated refrigeration and storage. *IOP Conference Series: Materials Science and Engineering*, 278(1):012012, dec 2017.

[10] C. A. Swenson. The Catalysis of the Ortho-Para Conversion in Liquid Hydrogen. *jcp*, 18(4):520–522, April 1950.

[11] Richard Folkson. 6 - hydrogen as an energy vector for transportation vehicles. In Richard Folkson and Steve Sapsford, editors, *Alternative Fuels and Advanced Vehicle Technologies for Improved Environmental Performance (Second Edition)*, Woodhead Publishing Series in Energy, pages 151–171. Woodhead Publishing, 2022.

[12] Myunghyun Suh, Hye Jeong Park, Prasad Thazhe Kootteri, and Dae Woon Lim. Hydrogen storage in metal-organic frameworks. *Chemical reviews*, 112:782–835, 12 2011.

[13] Nibedita Behera, Jingui Duan, Wanqin Jin, and Susumu Kitagawa. The chemistry and applications of flexible porous coordination polymers. *EnergyChem*, 3(6):100067, 2021.

[14] Nathaniel Rosi, Juergen Eckert, Mohamed Eddaoudi, David Vodak, Jaheon Kim, Michael O'Keeffe, and Omar Yaghi. Hydrogen storage in microporous metal-organic frameworks. *Science (New York, N.Y.)*, 300:1127–9, 06 2003.

[15] Gérard Férey, Michel Latroche, Christian Serre, Franck Millange, Thierry Loiseau, and title ="Hydrogen adsorption in the nanoporous metal-benzenedicarboxylate M(OH)(O2C–C6H4–CO2) (M = Al3+, Cr3+), MIL-53 Percheron-Guégan, Annick". *Chem. Commun.*, pages 2976–2977, 2003.

[16] Jesse Rowsell, Juergen Eckert, and Omar Yaghi. Characterization of H2 binding sites in prototypical metal-organic frameworks by inelastic neutron scattering. *Journal of the American Chemical Society*, 127:14904–10, 11 2005.

[17] F.M. Mulder, T.J. Dingemans, H.G. Schimmel, A.J. Ramirez-Cuesta, and G.J. Kearley. Hydrogen adsorption strength and sites in the metal organic framework MOF-5: Comparing experiment and model calculations. *Chemical Physics*, 351(1):72–76, 2008.

[18] Nour Nijem, Jean-Francois Veyan, Lingzhu Kong, Haohan Wu, Yonggang Zhao, Jing Li, David Langreth, and Yves Chabal. Molecular hydrogen "pairing" interaction in a metal organic framework system with unsaturated metal centers (MOF-74). *Journal of the American Chemical Society*, 132:14834–48, 10 2010.

[19] Craig M Brown, Yun Liu, Taner Yildirim, Vanessa K Peterson, and Cameron J Kepert. Hydrogen adsorption in HKUST-1: a combined inelastic neutron scattering and first-principles study. *Nanotechnology*, 20(20):204025, apr 2009.

[20] Tony Pham, Katherine A. Forrest, Peter A. Georgiev, Wiebke Lohstroh, Dong-Xu Xue, Adam Hogan, Mohamed Eddaoudi, Brian Space, and Juergen Eckert. A high rotational barrier for physisorbed hydrogen in a fcu-metal–organic framework. *Chem. Commun.*, 50:14109–14112, 2014.

[21] Kenji Sumida, Jae-Hyuk Her, Mircea Dinca, Leslie Murray, Jennifer Schloss, Christopher Pierce, Benjamin Thompson, Stephen Fitzgerald, Craig Brown, and Jeffrey Long. Neutron scattering and spectroscopic studies of hydrogen adsorption in Cr3(BTC)2—A metal-organic framework with exposed Cr2+ sites. *The Journal of Physical Chemistry C*, 115, 03 2011.

[22] Michael Hirscher and Barbara Panella. Hydrogen storage in metal–organic frameworks. *Scripta Materialia*, 56(10):809–812, 2007. Viewpoint set no. 42 “Nanoscale materials for hydrogen storage”.

[23] Jesse L. C. Rowsell and Omar M. Yaghi. Effects of functionalization, catenation, and variation of the metal oxide and organic linking units on the low-pressure hydrogen adsorption properties of metal-organic frameworks. *Journal of the American Chemical Society*, 128 4:1304–15, 2006.

[24] Houston Frost, Tina Düren, and Randall Snurr. Effects of surface area, free volume, and heat of adsorption on hydrogen uptake in metal-organic frameworks. *The journal of physical chemistry. B*, 110:9565–70, 06 2006.

[25] Farid Nouar, Juergen Eckert, Jarrod Eubank, Paul Forster, and Mohamed Eddaoudi. Zeolite-like metal-organic frameworks (ZMOFs) as hydrogen storage platform: Lithium and magnesium ion-exchange and h-2-(rho-ZMOF) interaction studies. *Journal of the American Chemical Society*, 131:2864–70, 03 2009.

[26] Jesse Rowsell and Omar Yaghi. Strategies for hydrogen storage in metal—organic frameworks. *Angewandte Chemie (International ed. in English)*, 44:4670–9, 11 2005.

[27] Wei Zhou, Hui Wu, and Taner Yildirim. Enhanced H2 adsorption in metal-organic frameworks with open metal sites: Binding mechanism and strong dependence on metal ions. 03 2009.

[28] Seyed Mohamad Moosavi, Aditya Nandy, Kevin Jablonka, Daniele Ongari, Jon Paul Janet, Peter Boyd, Yongjin Lee, Berend Smit, and Heather Kulik. Understanding the diversity of the metal-organic framework ecosystem. *Nature Communications*, 11, 08 2020.

[29] Kaido Sillar, Alexander Hofmann, and Joachim Sauer. Ab initio study of hydrogen adsorption in MOF-5. *Journal of the American Chemical Society*, 131:4143–50, 04 2009.

[30] Matthew Kapelewski, Stephen Geier, Matthew Hudson, David Stück, Jarad Mason, Jocienne Nelson, Dianne Xiao, Zeric Hulvey, Elizabeth Gilmour, Stephen Fitzgerald, Martin Head-Gordon, Craig Brown, and Jeffrey Long. M-2(m-dobdc) (m = mg, mn, fe, co, ni) metal-organic frameworks exhibiting increased charge density and enhanced H2 binding at the open metal sites. *Journal of the American Chemical Society*, 136, 08 2014.

[31] Craig M. Brown, Anibal Javier Ramirez-Cuesta, Jae-Hyuk Her, Paul S. Wheatley, and Russell E. Morris. Structure and spectroscopy of hydrogen adsorbed in a nickel metal–organic framework. *Chemical Physics*, 427:3–8, 2013. Advances and frontiers in chemical spectroscopy with neutrons.

[32] Kenji Sumida, Satoshi Horike, Steven Kaye, Zoey Herm, Wendy Queen, Craig Brown, Fernande Grandjean, Gary Long, Anne Dailly, and Jeffrey Long. Hydrogen storage and carbon dioxide capture in an iron-based sodalite-type metal-organic framework (fe-btt) discovered via high-throughput methods. (1), 2010-08-01 00:08:00 2010.

[33] Shanelle Suepaul, Katherine Forrest, Peter Georgiev, Paul Forster, Wiebke Lohstroh, Veronika Grzimek, Samuel Dunning, Joseph Reynolds, Simon Humphrey, Juergen Eckert, Brian Space, and Tony Pham. Investigating H2 adsorption in isostructural metal–organic frameworks m-cuk-1 (m = co and mg) through experimental and theoretical studies. *ACS Applied Materials and Interfaces*, 14, 02 2022.

[34] Tony Pham, Katherine Forrest, Adam Hogan, Brant Tudor, Keith McLaughlin, Jon Belof, Juergen Eckert, and Brian Space. Understanding hydrogen sorption in in-soc-MOF: A charged metal-organic framework with open-metal sites, narrow channels, and counterions. *Crystal Growth and Design*, 15:1460–1471, 01 2015.

[35] Vanessa Peterson, Yun Liu, Craig Brown, and Cameron Kepert. Neutron powder diffraction study of D2 sorption in Cu3 (1,3,5-benzenetricarboxylate) 2. *Journal of the American Chemical Society*, 128:15578–9, 01 2007.

[36] Craig M. Brown, Yun Liu, Taner Yildirim, Vanessa K. Peterson, and Cameron J. Kepert. Hydrogen adsorption in HKUST-1: a combined inelastic neutron scattering and first-principles study. *Nanotechnology*, 20:204025, 2009.

[37] Daniil Polyukhov, Nikita Kudriavykh, Sergey Gromilov, Alexey Kiryutin, Artem Poryvaev, and Matvey Fedin. Efficient MOF-catalyzed ortho–para hydrogen conversion for practical liquefaction and energy storage. *ACS Energy Letters*, 7:4336–4341, 11 2022.

[38] Giovanni Romanelli, Felix Fernandez-Alonso, Triestino Minniti, and Matthew Krzystyniak. Visualisation of the catalysed nuclear-spin conversion of molecular hydrogen using energy-selective neutron imaging. 04 2019.

[39] K. Svensson, L. Bengtsson, J. Bellman, M. Hassel, M. Persson, and S. Andersson. Two-dimensional quantum rotation of adsorbed H_2. *Phys. Rev. Lett.*, 83:124–127, Jul 1999.

[40] L. Bengtsson, K. Svensson, M. Hassel, J. Bellman, M. Persson, and S. Andersson. H2 adsorbed in a two-dimensional quantum rotor state on a stepped copper surface. *Phys. Rev. B*, 61:16921–16932, Jun 2000.

[41] D. Teillet-Billy and J.P. Gauyacq. Rotational excitation of physisorbed molecules by resonant electron scattering. *Surface Science*, 502-503:358–363, 2002.

[42] Jesse Rowsell, Juergen Eckert, and Omar Yaghi. Characterization of H2 binding sites in prototypical metal-organic frameworks by inelastic neutron scattering. *Journal of the American Chemical Society*, 127:14904–10, 11 2005.

[43] Fokko Mulder, Theo Dingemans, H. Schimmel, A. Ramirez-Cuesta, and Gordon Kearley. Hydrogen adsorption strength and sites in the metal organic framework MOF-5: Comparing experiment and model calculations. *Chemical Physics*, 351, 07 2008.

[44] G. L. Squires. Introduction to the theory of thermal neutron scattering. *Cambridge University Press*, 53, 2012.

[45] https://www.nist.gov/ncnr/chrns. Center for high resolution neutron scattering.

[46] https://www.ornl.gov. Oak Ridge National Laboratory.

[47] https://www.ill.eu. ILL neutron for society.

[48] https://lansce.lanl.gov. Los Alamos Neutron Science Center LANSCE.

[49] https://www.isis.stfc.ac.uk. ISIS facility website.

[50] https://europeanspallationsource.se. European spallation source.

[51] J Mayers, J Tomkinson, T Abdul-Redah, W.G Stirling, C Andreani, R Senesi, M Nardone, D Colognesi, and E Degiorgi. Vesuvio—the double difference inverse geometry spectrometer at ISIS. *Physica B: Condensed Matter*, 350(1, Supplement):E659–E662, 2004. Proceedings of the Third European Conference on Neutron Scattering.

[52] James A. Young and Juan U. Koppel. Slow neutron scattering by molecular hydrogen and deuterium. *Phys. Rev.*, 135:A603–A611, Aug 1964.

[53] Giovanni Romanelli, Svemir Rudić, Matteo Zanetti, Carla Andreani, Felix Fernandez-Alonso, Giuseppe Gorini, Maciej Krzystyniak, and Goran Škoro. Measurement of the para-hydrogen concentration in the ISIS moderators using neutron transmission and thermal conductivity. *Nuclear Instruments and Methods in Physics Research Section A: Accelerators, Spectrometers, Detectors and Associated Equipment*, 888:88–95, 2018.

[54] Caroline A. Schneider, Wayne S. Rasband, and Kevin W. Eliceiri. NIH image to ImageJ: 25 years of image analysis. *Nature methods*, 9(7):671–675, 2012.

[55] Johannes Schindelin, Ignacio Arganda-Carreras, Erwin Frise, Verena Kaynig, Mark Longair, Tobias Pietzsch, Stephan Preibisch, Curtis Rueden, Stephan Saalfeld, Benjamin Schmid, Jean-Yves Tinevez, Daniel James White, Volker Hartenstein, Kevin Eliceiri, Pavel Tomancak, and Albert Cardona. Fiji: an open-source platform for biological-image analysis. *Nature Methods*, 9, 2012.

[56] O. Arnold, J.C. Bilheux, J.M. Borreguero, A. Buts, S.I. Campbell, L. Chapon, M. Doucet, N. Draper, R. Ferraz Leal, M.A. Gigg, V.E. Lynch, A. Markvardsen, D.J. Mikkelson, R.L. Mikkelson, R. Miller, K. Palmen, P. Parker, G. Passos, T.G. Perring, P.F. Peterson, S. Ren, M.A. Reuter, A.T. Savici, J.W. Taylor, R.J. Taylor, R. Tolchenov, W. Zhou, and J. Zikovsky. Mantid—data analysis and visualization package for neutron scattering and muon SR experiments. *Nuclear Instruments and Methods in Physics Research Section A: Accelerators, Spectrometers, Detectors and Associated Equipment*, 764:156–166, 2014.

[57] S. Koerner. Digital image processing in neutron radiography. *Technische Univ. Wien Bibliothek*, 2000.

[58] René Hassanein, Eberhard Lehmann, and Peter Vontobel. Methods of scattering corrections for quantitative neutron radiography. *Nuclear Instruments and Methods in Physics Research Section A: Accelerators, Spectrometers, Detectors and Associated Equipment*, 542(1):353–360, 2005. Proceedings of the Fifth International Topical Meeting on Neutron Radiography.

[59] Davide Micieli, Triestino Minniti, and Giuseppe Gorini. Neutompy toolbox, a Python package for tomographic data processing and reconstruction. *SoftwareX*, 9:260–264, 2019.

[60] Giovanni Romanelli, Margherita Simoni, Enrico Preziosi, Jose Damian, Carla Andreani, and Roberto Senesi. Neutron thermal cross sections of 3D-printing organic polymers using the average functional group approximation. *EPJ Web of Conferences*, 284, 05 2023.

[61] Giovanni Romanelli, Dalila Onorati, Pierfrancesco Ulpiani, Stephanie Cancelli, Enrico Perelli-Cippo, José Ignacio Márquez Damián, Silvia Capelli, Gabriele Croci, Andrea Muraro, Marco Tardocchi, Giuseppe Gorini, Carla Andreani, and Roberto Senesi. Thermal neutron cross sections of amino acids from average contributions of functional groups. *Journal of Physics: Condensed Matter*, 33(28):285901, may 2021.

[62] X.-X. Cai and T. Kittelmann. Ncrystal: A library for thermal neutron transport. *Computer Physics Communications*, 246:106851, 2020.

[63] Zha Yuan, Hui Wen, Yuan Liu, and Qi Wang. Synergy between piperazine pyrophosphate and aluminum diethylphosphinate in flame retarded acrylonitrile-butadiene-styrene copolymer. *Polymer Degradation and Stability*, 190:109639, 2021.

Acknowledgments

Un sentito ringraziamento va al Dott. Giovanni Romanelli e al Prof. Roberto Senesi, per la loro pazienza, per i consigli preziosi, ma soprattutto per avermi più volte offerto la possibilità di mettermi alla prova, facendomi muovere i primi passi nel mondo della ricerca.

Un ringraziamento speciale va agli amici di sempre, è anche il loro affetto incondizionato che mi ha portato fin qui.

Ringrazio miei colleghi, in particolare Matteo e Virginia, che più di tutti hanno alleggerito questi anni di studio.

Un pensiero speciale va alla mia famiglia, che in questi anni mi ha sempre dimostrato il suo sostegno incondizionato: non posso che dedicare a tutti voi questo traguardo.